Title	Newly Developed Method of Measurement for Conversion Electron Mossbauer Spectroscopy and its Applications in Material Sciences
Author(s)	谷本, 久典
Citation	大阪大学, 1990, 博士論文
Version Type	VoR
URL	https://hdl.handle.net/11094/286
rights	
Note	

NEWLY DEVELOPED METHOD OF THE MEASUREMENT FOR CONVERSION ELECTRON MÖSSBAUER SPECTROSCOPY AND ITS APPLICATIONS IN MATERIAL SCIENCES

A Thesis Submitted to
Osaka University

For the Requirements of the Degree
of Doctor of Engineering

Hisanori TANIMOTO

Department of Material Physics
Faculty of Engineering Science
Osaka University

February 1990

SYNOPSIS

Newly designed gas proportional electron counters have been developed in order to achieve the higher counting rate and the stable operation at low temperatures. By using these counters, conversion electron Mössbauer spectroscopy (CEMS) has been applied in order to demonstrate the advantage of CEMS to study the physical and chemical properties at the surface of various kinds of materials. First, the behavior of ^{119}Sn atoms implanted into Ni and Fe metals has been investigated by ^{119}Sn and ^{57}Fe CEMS. CEMS spectra consist of the components rising from solid solutions, intermetallic compounds, clusters and oxides of Sn. Their formation is well explained by the local Sn concentration. Secondly, CEMS has been applied to the study of the remarkable work hardening of high-manganese steel. CEMS measurement reveals the decarburization around the surface of high-manganese steel and the origin of the remarkable hardening is due to the formation of ε martensite. Thirdly, the interface between Al_2O_3 surface layer and α-Fe substrate deposited by chemical vapor deposition has been investigated by CEMS. The interface between α-Fe substrate and Al_2O_3 layer has no mixing of Al_2O_3 and Fe atoms. But the Fe^{2+} and Fe^{3+} ionic states are generated by the annealing of the specimens. Fourthly, the surface of Nd-Fe-B permanent magnet has been measured by CEMS. It is found that the surface of $Nd_2Fe_{14}B$ compound is covered with small α-Fe clusters after heat-treatment. Finally, CEMS measurements have been performed for pellets of Y-Ba-Cu oxide superconductor. CEMS spectra suggest the existence of the preferred orientation of the c-axis in the disk shaped specimen and the principal axis of electric field gradient is parallel or perpendicular to the c-axis. These applications of CEMS measurements clearly show that CEMS is one of the powerful techniques to study the microscopic state around the surface of various materials.

CONTENTS

CHAPTER I. INTRODUCTION

1.1 General introduction

In this investigation, the development of newly designed gas proportional electron counters and their applications for the conversion electron Mössbauer spectroscopy are described. Advantage of conversion electron Mössbauer spectroscopy for the investigation of the physical and chemical properties at the surface of various materials is demonstrated utilizing ^{57}Fe and ^{119}Sn CEMS measurements.

Conversion electron Mössbauer spectroscopy (CEMS)[1-3] is well known as one of the powerful techniques to study the microscopic properties of surface layers of materials. CEMS spectra are obtained by the detection of electrons which are emitted from the Mössbauer probe atoms as the internal conversion process of Mössbauer resonance nuclei. These electrons are called as the conversion electrons. Straggling range of the conversion electron is so short in solids that only electrons which are emitted near the surface can emerge from the surface and are detected by the well designed electron counters. In the case of ^{57}Fe CEMS, the energy of the K-shell conversion electron is 7.3 keV and this electron has only about 100 nm of the straggling range in metallic iron. Therefore, the CEMS spectrum contains the microscopic information only near the surface. For its higher sensitivity to the surface layers, CEMS is known as one of the powerful techniques to study the microscopic properties near surface.

In chapter I, the principles and the explanations of the Mössbauer effect and the CEMS are given.

Two kinds of the gas proportional electron counters which were newly developed in order to achieve the higher counting rate are described in chapter II.

In chapter III, the applications of CEMS measurements to five kinds of materials are presented.

At the first part of chapter III, the CEMS measurements applied to study the microscopic behavior of the ^{119}Sn ion-implanted into pure Ni and Fe metals have been discussed. Ion-implantation technique has become popular to improve the physical properties at the material surface. But not only implanted impurity atoms but also a lot of lattice defects are introduced during the ion-implantation process. These impurities and defects give rise to the problems such as the interactions of each other, clustering and the formation of the non-equilibrium phases. CEMS measurements revealed that Ni-Sn solid solutions and Ni_3Sn intermetallic compounds are formed by the ^{119}Sn implantation into Ni at room temperature. The formation of the Ni_3Sn compounds are associated with the radiation enhanced diffusion of the implanted Sn atoms. In the case of the ^{119}Sn implantation into Fe at room temperature, Fe-Sn solid solutions and oxides and clusters of Sn atoms are formed. But the components of intermetallic compounds are not observed in any CEMS spectra. The different behavior of the implanted Sn atoms in the targets between Ni and Fe would be due to the difference of the vacancy mobility in Ni and Fe metals at room temperature.

At the second part of chapter III, the mechanism of the remarkable work hardening around the surface of a high-manganese steel, which is called as Hadfield steel$^{4)}$, has been studied by

CEMS. Hadfield steel is widely used for the abrasion-resistant steel because of its remarkable work hardening property. A lot of investigations for the mechanism of the work hardening of Hadfield steel were reported, but its mechanism has not been clear yet in spite of these efforts. From the CEMS measurements, the decarburization at the surface of the high-manganese steels is found and it is concluded that the remarkable work hardening of Hadfield steel is resulted from the formation of ε martensite by working.

At the third part of chapter III, the property at the interface between α-Fe substrate and Al_2O_3 layers deposited by using a chemical vapor deposition (CVD) technique. The CVD technique is utilized to coat the substrate surface with some molecules generated by thermal decomposition, especially in the field of the semiconductor device production. Annealing effect on the interface between the -Fe substrate and Al_2O_3 layers also has been investigated by CEMS. After the deposition of Al_2O_3 layers on the α-Fe foil, the interface between the α-Fe substrate and deposited Al_2O_3 layers was clear and no mixing of Fe atoms and Al_2O_3 layers was observed. However, the magnetic closure domain of α-Fe substrate is divided into smaller domains by the deposition of Al_2O_3 layers. After annealing of the deposited foils at various temperatures, small amounts of Fe^{2+} and Fe^{3+} ionic states were observed at the interface.

At the fourth part of chapter III, the surface layers of $Nd_2Fe_{14}B$ intermetallic compound have been studied by applying CEMS measurements. The Nd-Fe-B ($Nd_2Fe_{14}B$) alloy is well known as the excellent permanent magnet material5), which has the largest maximum energy products over 290 kJ/m^3 than the other magnets like SmCo compounds. However, it is reported that the coercive force around the surface of Nd-Fe-B permanent magnet is considerably smaller than that of the inner grains as the bulk. In order to clarify the magnetic properties at the surface, the CEMS measurements have been performed using various treated Nd-Fe-B permanent magnets. CEMS measurements clarified that the surface of the heat-treated Nd-Fe-B magnet is covered with small α-Fe clusters. The low coercive force at the surface of the Nd-Fe-B magnet is due to the decomposition of Nd and B atoms from the $Nd_2Fe_{14}B$ intermetallic compound at the surface by the heat-treatment.

In the final section of chapter III, the differences of the ^{57}Fe states between the surface layers and the bulk of Y-Ba-Cu oxide superconductors are discussed by comparing the CEMS and transmission Mössbauer spectra. The acquired CEMS and transmission Mössbauer spectra have not shown any appreciable difference so that the chemical state at the surface of Y-Ba-Cu oxide superconductor is almost same to the bulk state. From the intensity ratio of the doublet peak in CEMS spectra, it is suggested that the principal axis of the electric field gradient is parallel or perpendicular to the c-axis.

The results from the present investigation made sure that CEMS is a quite powerful technique to understand the physical and chemical properties near the surface of the various kinds of materials.

In chapter IV, the results of this investigation are summarized.

1.2 Mössbauer effect[6-10)]

The nucleus at the excited state is deexcited to the ground state by the emitting γ-ray after its appropriate life time. If there are two nuclei of the same species and one is at the ground state and the other is at the excited state, it is expected that γ-ray resonance absorption by nuclei can be observed like the resonance fluorescence in atoms by visible light. In the case of the nucleus, however, the recoil of the nuclei by γ-ray cannot be negligible compared to the energy broadening of γ-ray because of the higher energy of the γ-ray than the visible light. From the conservation of energy and momentum, the recoil energy of a free nucleus, E_R, is given by eq (1).

$$E_R = 1/(2M)\,(E_\gamma/c)^2, \qquad (1)$$

where E_γ is the energy of γ-ray. M and c are a mass of a free nucleus and the velocity of light. When the nucleus emits γ-ray, the nucleus is recoiled to the opposite direction to the direction of γ-ray emission and the transition energy is shared with those of γ-ray and the recoil. When the nucleus absorbs γ-ray, the nucleus is recoiled to the same direction to γ-ray and the energy for the resonance required to be the sum of the nuclear transition and the recoil energy. So that the energy of γ-ray emitted from the nucleus is smaller than the transition energy by E_R and the energy of γ-ray absorbed by the nucleus is larger than the transition energy by E_R. The typical value of E_R is about 10^{-2} eV and that of the energy width of γ-ray is about 10^{-8} eV. There is little overlapping of the energy spectrum between emitted γ-ray and absorbed γ-ray and γ-ray resonance absorption hardly occurs in this condition (Fig. 1-1(a)).

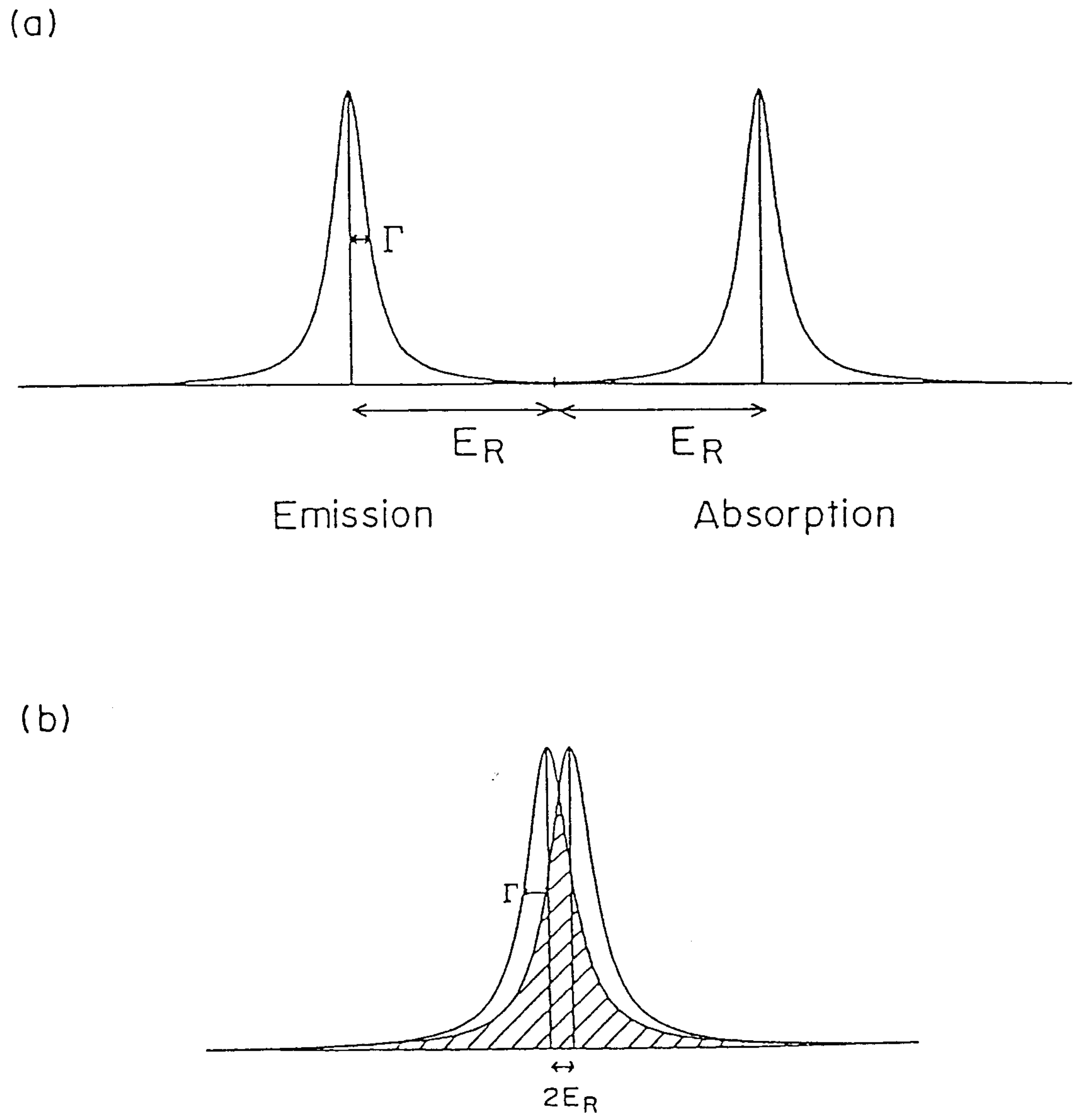

Fig. 1-1. Energy distributions of the emitted and absorbed γ-ray by a nucleus. E_R and Γ are the recoil energy and the half width at half maximum, respectively. In the case of (a), the emission and absorption lines do not overlap because of the large recoil energy compared to Γ.

Before the discovery of Mössbauer effect, some efforts were made to observe the nuclear γ-ray resonance absorption. For example, the nucleus was driven very fast applying the ultracentrifuge to compensate the recoil energy by Doppler energy shift. The other way is to utilize the thermal Doppler broadening of γ-ray at high temperature gas phase. At high temperature gas phase, the energy width of γ-ray becomes broad because of Doppler effect caused by the intense thermal motion. The enough broadening leads to the overlapping of energy distributions between emitted and absorbed γ-ray. The cascade of decay process was also used to compensate the recoil energy. The recoil of the nucleus by prior decay was applied to the loss of the energy at resonance absorption of leading γ-ray emission.

In 1957, Mössbauer found that the probability for the nuclear γ-ray resonance of ^{191}Ir rapidly increased with the decrease of temperature under 160 K$^{11)}$. It was thought that the probability for the γ-ray resonance absorption became small with the decrease of temperature in order to the decrease of the overlapping on the energy spectra of emitted and absorbed γ-ray. Mössbauer's discovery is contrary to this thought and was not believed for a few years. The most important point of his discovery is that a part of γ-ray which is emitted or absorbed by the nucleus in solids is not concerned in the recoil energy loss. In solids, the nucleus is restricted in its position by the surrounding lattice atoms and the recoil comes to be shared by the group of these atoms. In this case, the mass in eq. (1) becomes so large that the recoil energy E_R can be almost to be zero. If E_R is zero, the energy distributions of emitted and absorbed γ-ray are wholly overlapped and resonance absorption of γ-ray can be easily observed. This process is called recoil-free nuclear γ-ray resonance absorption, which is named to be Mössbauer effect by discovery.

The probability to emit or absorb γ-ray without the recoil is the important factor to observe the Mössbauer effect. The probability to emit or absorb γ-ray without the recoil is defined as the recoil-free fraction f. The value of f can be calculated by using Debye model of lattice vibration at temperature T well below the Debye temperature θ_D.

$$f = \exp[-3E_RT/(2k\theta_D)], \qquad (2)$$

where k is the Boltzmann's constant.

This equation shows that f has the large value when E_R described by eq. (1) is small and the Debye temperature of the absorber and source is high. The value of f also depends on the temperature of the measurement. It becomes large with the decrease of the temperature.

The ratio of energy width to the energy of γ-ray on Mössbauer effect is smaller than 10^{-12} and such a value cannot be achieved by other spectroscopic methods. It means that Mössbauer spectroscopy has the higher energy resolution than any other spectroscopy. For this reason, Mössbauer spectroscopy is applied to the various field of science$^{12)}$.

Mössbauer spectrum is constructed by recording the relative transmission or emission at various energy shift from a certain energy. The energy shift is usually achieved by giving the relative velocity between γ-ray source and absorber. Some energy shift of the standard material is chosen as a zero point of the velocity. This Mössbauer spectrum reflects the interactions between the nucleus and the surrounding electrons (hyperfine interactions) and these interactions cause the energy shifts and the splitting of peaks in the spectrum.

a) Isomer shift

The energy levels of the nucleus would be shifted by the different density of electrons at the nucleus. If the electronic state around the nucleus in γ-ray source is different from that in absorber, some energy shifts can be observed in the transition energy between the source and the absorber (Fig. 1-2(a)). This is called as isomer shift and one can discuss the valence state of the probe atom which contains the resonant nucleus.

b) Electric quadrupole interaction

The electric charge distribution of the nucleus is non-spherical if the quantum number of the nuclear spin is larger than I=1. The electric quadrupole moment Q, which describes the non-spherical distribution of electric charge, is defined by the following equation.

$$eQ = \int \rho r^2 (3\cos^2\theta - 1) d\tau, \qquad (3)$$

where ρ is the electric charge density in the volume fraction of $d\tau$, which locates at the distance r from the center of the nucleus with the angle θ from the quantization axis of the nuclear spin.

The electric field gradient rising from the non-cubic symmetry and the electric quadrupole moment of the nucleus interacts with each other and the energy level of the nucleus with the spin quantum number I would be split as follows.

$$E_Q = e^2qQ/[4I(2I-1)]\cdot[3I_z{}^2-I(I+1)](1+\eta^2)^{1/2}, \qquad (4)$$

where the diagonalized electric field gradient tensor and asymmetry parameter η are described by the followings,

$$eq = V_{zz} = \partial^2V/\partial z^2$$

$$\eta = (V_{xx}-V_{yy})/V_{zz} \qquad |V_{zz}| \geqq |V_{yy}| \geqq |V_{xx}|.$$

By this interaction, the peaks corresponding to this splitting will be observed in the spectrum. Figure 1-3(b) shows the splitting of the Mössbauer peak in the case of the transition from I = 3/2 to 1/2 by the electric quadrupole interaction.

c) Magnetic dipole interaction

Under a certain magnetic field, the energy level of the nucleus having the spin quantum number I will split into 2I + 1 sublevels.

$$E_m = -g_N\beta_NHm_I, \qquad (5)$$

where g_N and β_N are the nuclear g-factor and nuclear Bohr magneton. H is the magnetic field and m_I is the magnetic quantum number representing the z component of I.

However, all transitions between the sublevels of the excited and ground states are not allowed by the selection rule of the transition. The spin quantum numbers of exited and ground state of ^{57}Fe are I = 3/2 and 1/2 and its transition type is M1 which allows the angular momentum change of ±1 and 0. In this case, six kinds of the transitions are allowed and the magnetically split Mössbauer spectrum of ^{57}Fe becomes like Fig. 1-3(c).

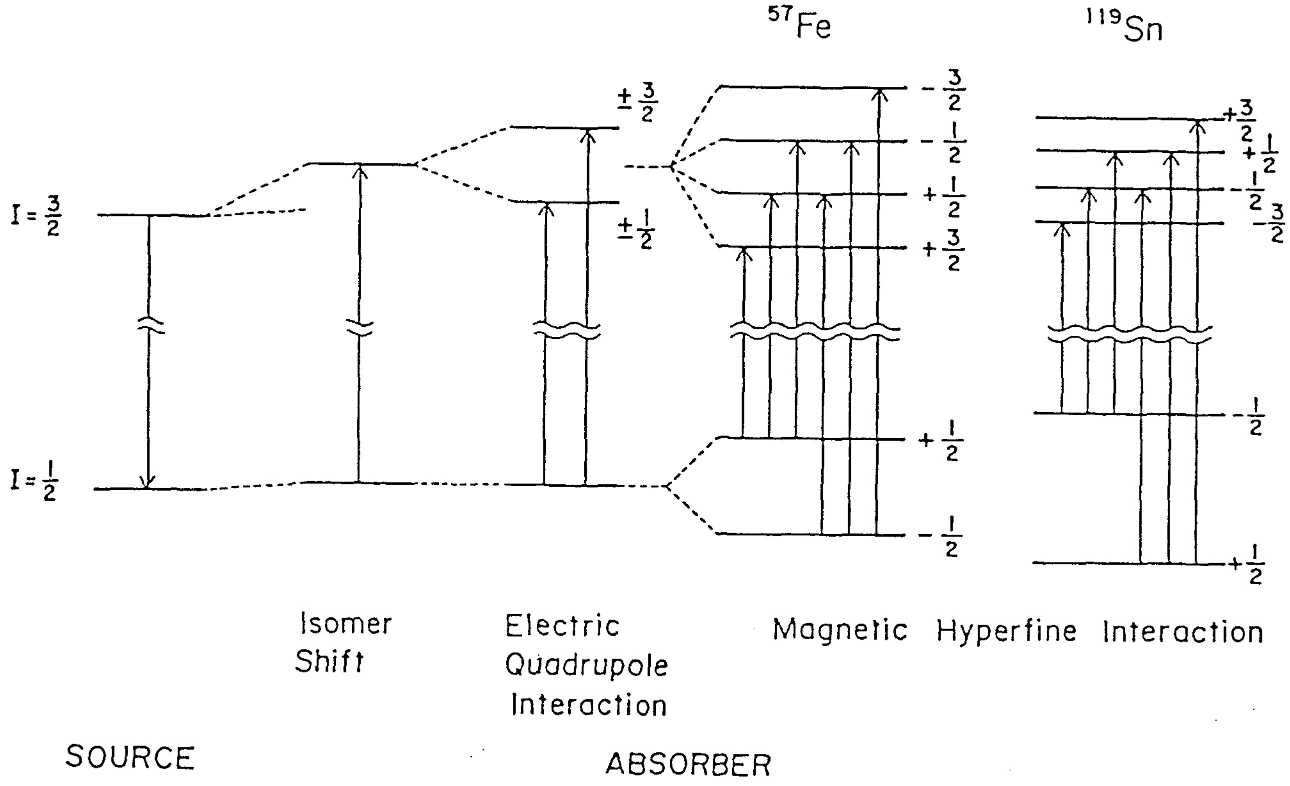

Fig. 1-2. The shifts and splittings of nuclear energy levels by hyperfine interactions and the transition between I=1/2 and 3/2 nuclear states.

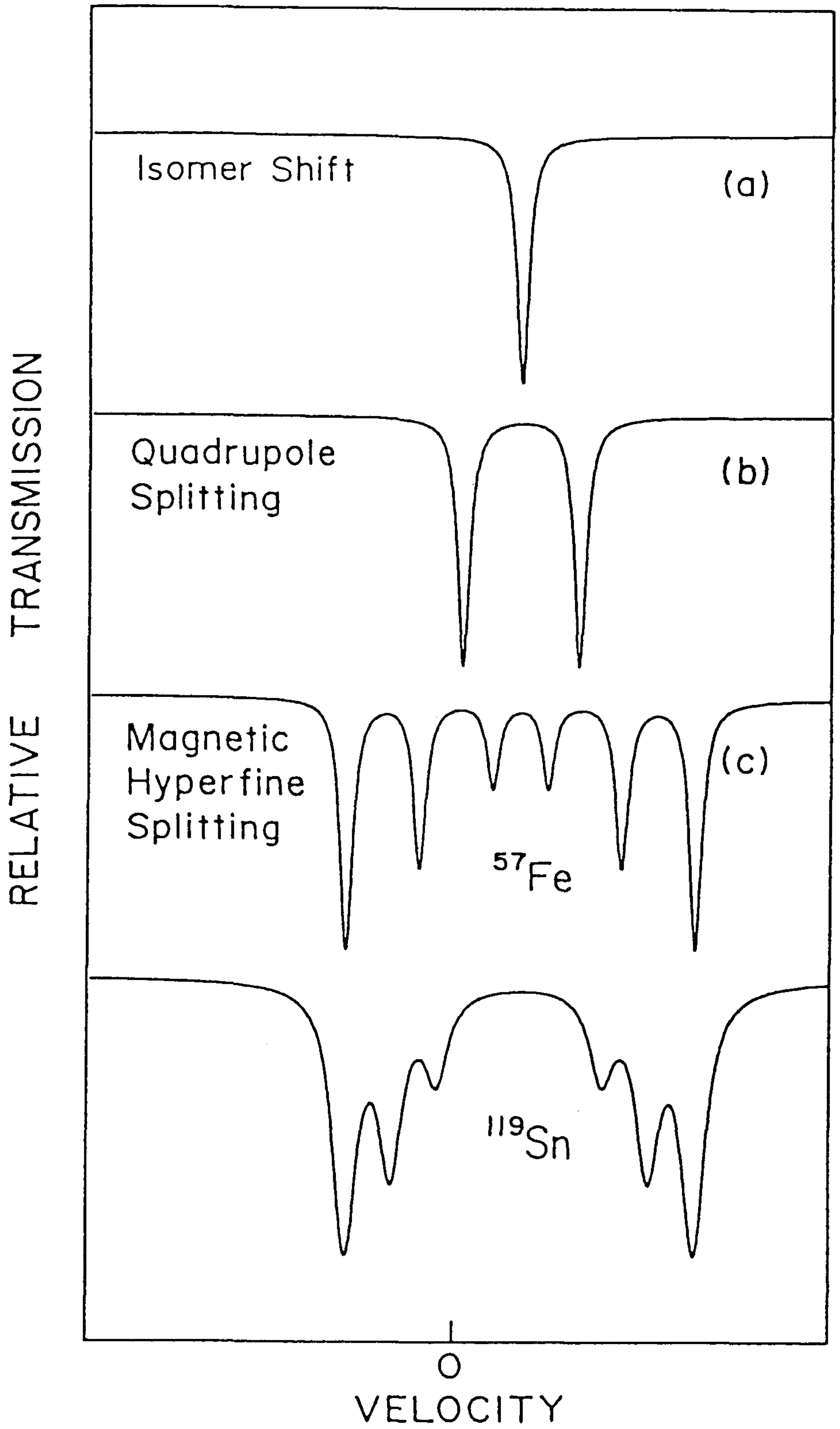

Fig. 1-3. Hyperfine interactions reflected on the Mössbauer spectra. These spectra correspond to the energy level schemes in Fig. 1-2.

d) Mixed hyperfine interaction

In general, these hyperfine interactions mentioned as above appear not independently but are usually mixed and the Hamiltonian cannot be solved analytically. In the case of ^{57}Fe, the interaction energy of magnetic dipole interaction under magnetic field is much larger than that of electric quadrupole interaction and the electric quadrupole interaction can be treated by the perturbation to the magnetic interaction. The energy levels in such a case are described by following equation and the spectrum shown in Fig. 1-4, assuming $\eta = 0$.

$$E = -g_N\beta_N H m_I + (-1)^{m_I+1/2} e^2 qQ(3\cos^2\theta - 1)/8, \qquad (6)$$

where θ is the angle between the principal axis of the electric field gradient and the direction of the magnetic field.

If the magnitude of the electric quadrupole interaction is comparable to that of the magnetic hyperfine interactions, a corresponding Hamiltonian of the nuclear energy state cannot be resolved analytically. In this case, the numerical calculation13) of the eigenvalues and eigenfunctions for the given Hamiltonian is useful to analyze the complicated spectrum rising from the mixed hyperfine interaction.

Figure 1-5 (a) shows the Mössbauer spectrum of the austenitic high-manganese steel measured at room temperature and 20 K. At room temperature, the spectrum obtained is well analyzed by the combination of a singlet peak and quadrupole splitting doublet peak. The doublet peak corresponds to the Fe atoms having C atoms at the neighbor interstitial sites.

At 20 K, the weak magnetic field is caused by the antiferromagnetic order of Fe atoms14,15). The singlet peak observed at

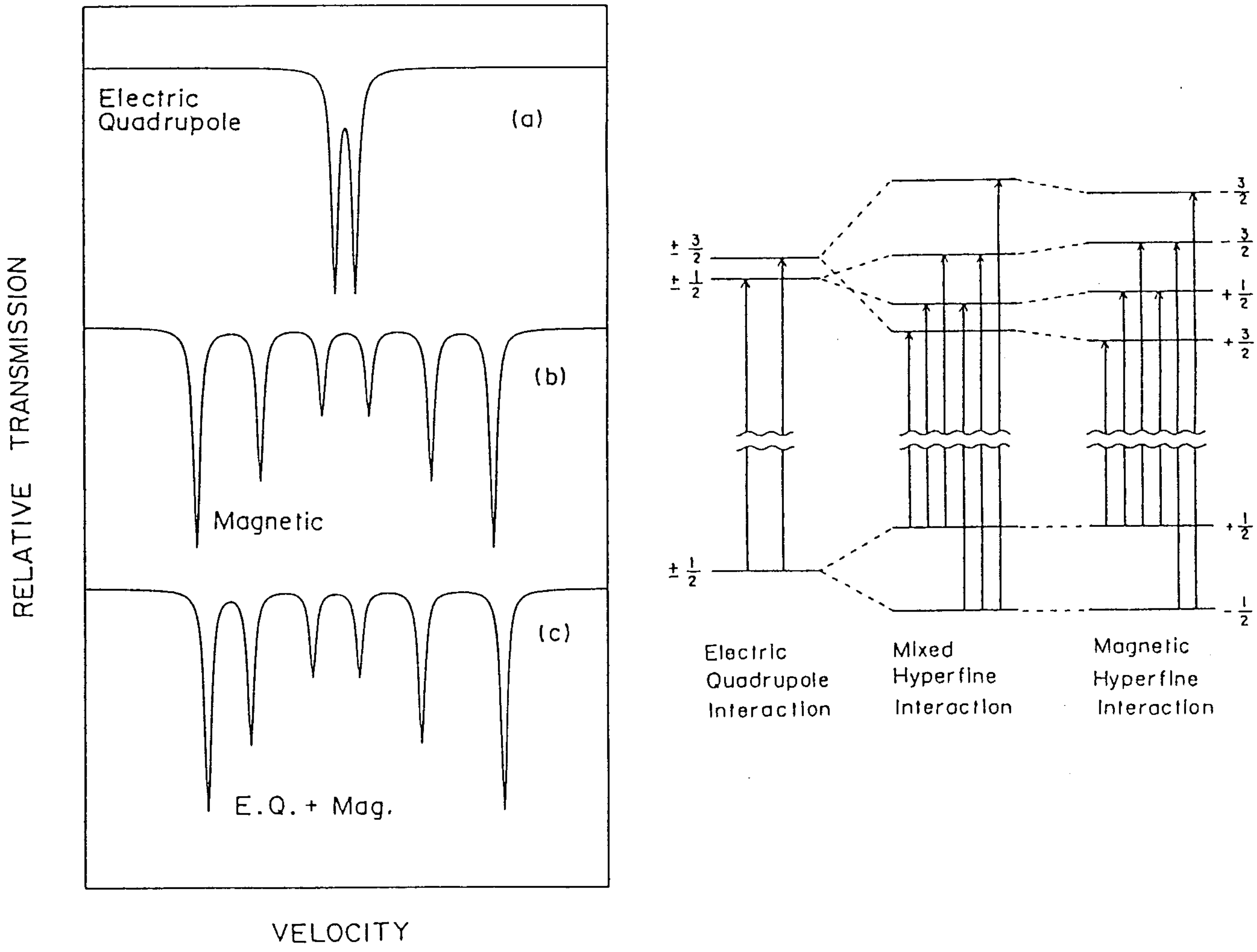

Fig. 1-4. Typical Mössbauer spectra for the transition between I = 1/2 and 3/2 nuclear states obtained from the following hyperfine interactions.

(a) Pure electric quadrupole interaction.

(b) Pure magnetic hyperfine interaction.

(c) The effect of a small electric quadrupole perturbation on the magnetic hyperfine splitting. The outer two peaks of 6-line shifts by the energy of $e^2qQ(3\cos^2\theta -1)/8$ and the other peaks shift by the energy of $-e^2qQ(3\cos^2\theta -1)/8$. η is assumed to be 0.

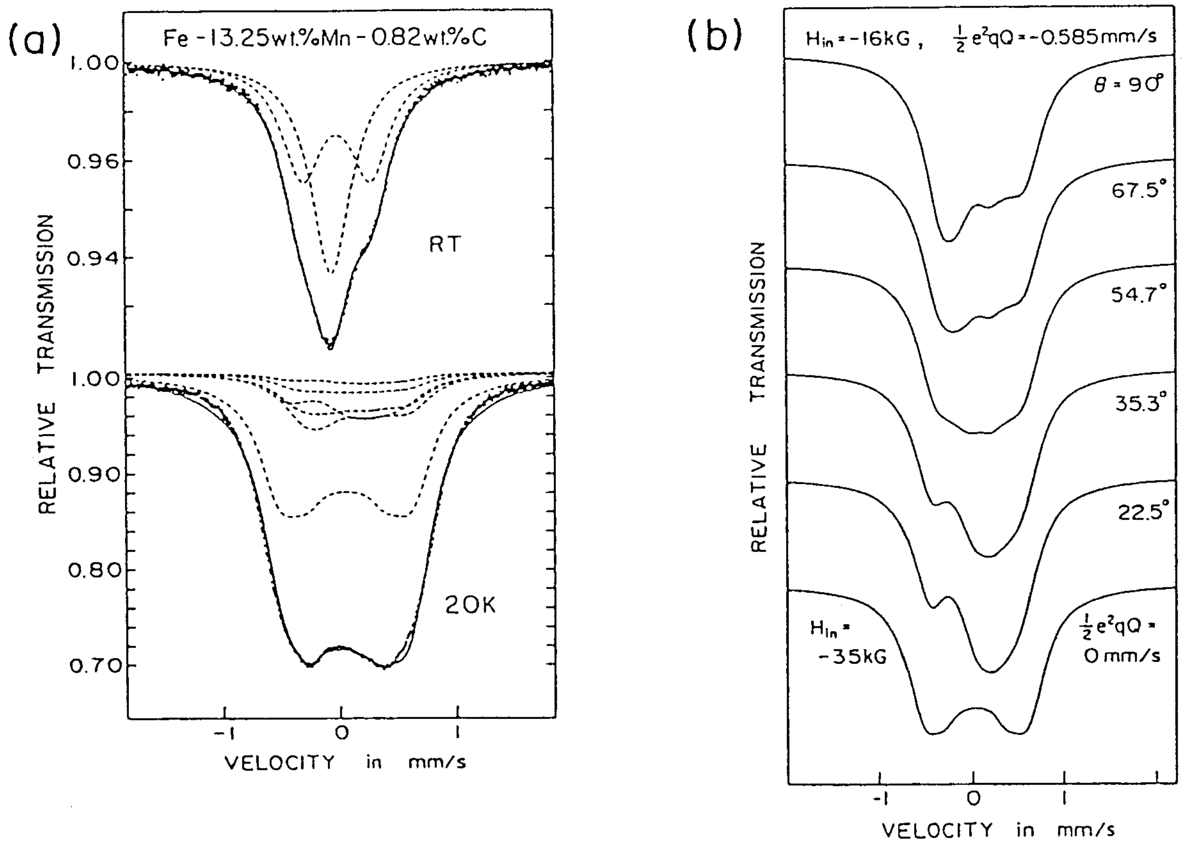

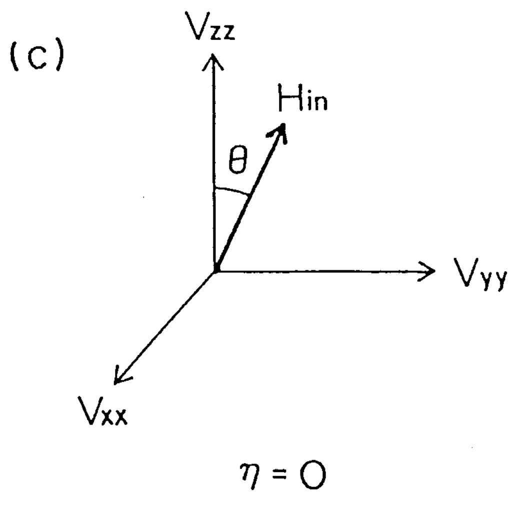

Fig. 1-5. (a) Transmission Mössbauer spectra of Fe-13.25wt.%Mn-0.82wt.%C austenitic steel measured at room temperature and 20 K. At room temperature, the spectrum is well reproduced by the combination of a singlet peak and a quadrupole splitting doublet peak. At 20 K, the weak magnetic hyperfine field is caused from the antiferromagnetic order of the magnetic moments of Fe atoms. The spectrum measured at 20 K was analyzed by the combinations of six components, which are presented in figure (b). The principal axis of the electric field gradient tensor and the magnetic field H_{in} is shown in figure (c). The asymmetry parameter η is assumed to be zero.

room temperature becomes a weakly split 6-line pattern only by the weak magnetic hyperfine interaction. On the other hand, the doublet peak observed at room temperature becomes complicated peaks because of the superposition of the weak magnetic hyperfine interaction to the electric quadrupole interaction. The magnitudes of these interactions are comparable so that the corresponding Hamiltonian cannot be resolved by the analytical way.

The transition energy and probability for each transition were evaluated by the numerical calculation by using the Mössbauer parameters at room temperature and spin structure proposed to fcc Fe precipitates in Cu16). The solid line in the spectrum measured at 20 K is the calculated spectrum by using the electric field gradient value of $-2\mathrm{x}10^{17}$ V/cm^2 and hyperfine field magnitude of -16 kG. The calculated spectrum is constructed by one 6-line pattern split only by the magnetic hyperfine interaction and five complicated peaks split by the mixed hyperfine interactions having different angles between the principal axis of the electric field gradient and the direction of the magnetic field at the Fe nucleus. These components are shown in Fig. 1-5 (b).

From this analysis, it is determined that the sign of the electric field gradient caused by the C atom in fcc Fe is negative and the value of the magnetic field of the Fe atoms having C atoms at the neighbor interstitial sites is -16 kG.

1.3 Internal conversion process17-19)

After an appropriate life time, the nucleus at the excited level by the recoil-free γ-ray absorption deexcites to the ground state emitting the excess energy. There are two ways in the deexcitation process. One is the reemission of γ-ray. The other is the internal conversion process. The pair creation is also concerned to the deexcitation process for the nucleus. But the transition energy involved with Mössbauer effect is too small to create the electron and positron pair.

Figure 1-6 shows the decay scheme of ^{57}Fe, the levels at the right hand side are corresponding to the nuclear states and the left hand side to the electronic states. The nucleus at the excited state with I = 3/2 deexcites to the ground state with I = 1/2. In this process, the probability to be deexcited by the reemission of γ-ray is only 10 %. By the probability of 90 %, the exited nucleus deexcites by emitting a K-shell electron without any γ-ray emission[20)]. This emitted electron is called as the conversion electron. The internal conversion coefficient α is defined by the ratio of the probability of the internal conversion process to that of γ-ray reemission. The value α of ^{57}Fe has been determined to be 9. The values of the internal conversion coefficient are calculated for the each electron shell of the various nuclei, applying the theory for the dipole radiation. The general characteristics for the internal conversion coefficient are as follows.

a) The values increase with the increase of the atomic number.

b) For one nucleus, the largest value is achieved by the electron orbital that has the largest probability at the nucleus. This is due to the fact that the internal conversion process is the direct interaction between the nucleus and the electrons.

c) The value for the magnetic transition is larger than that of

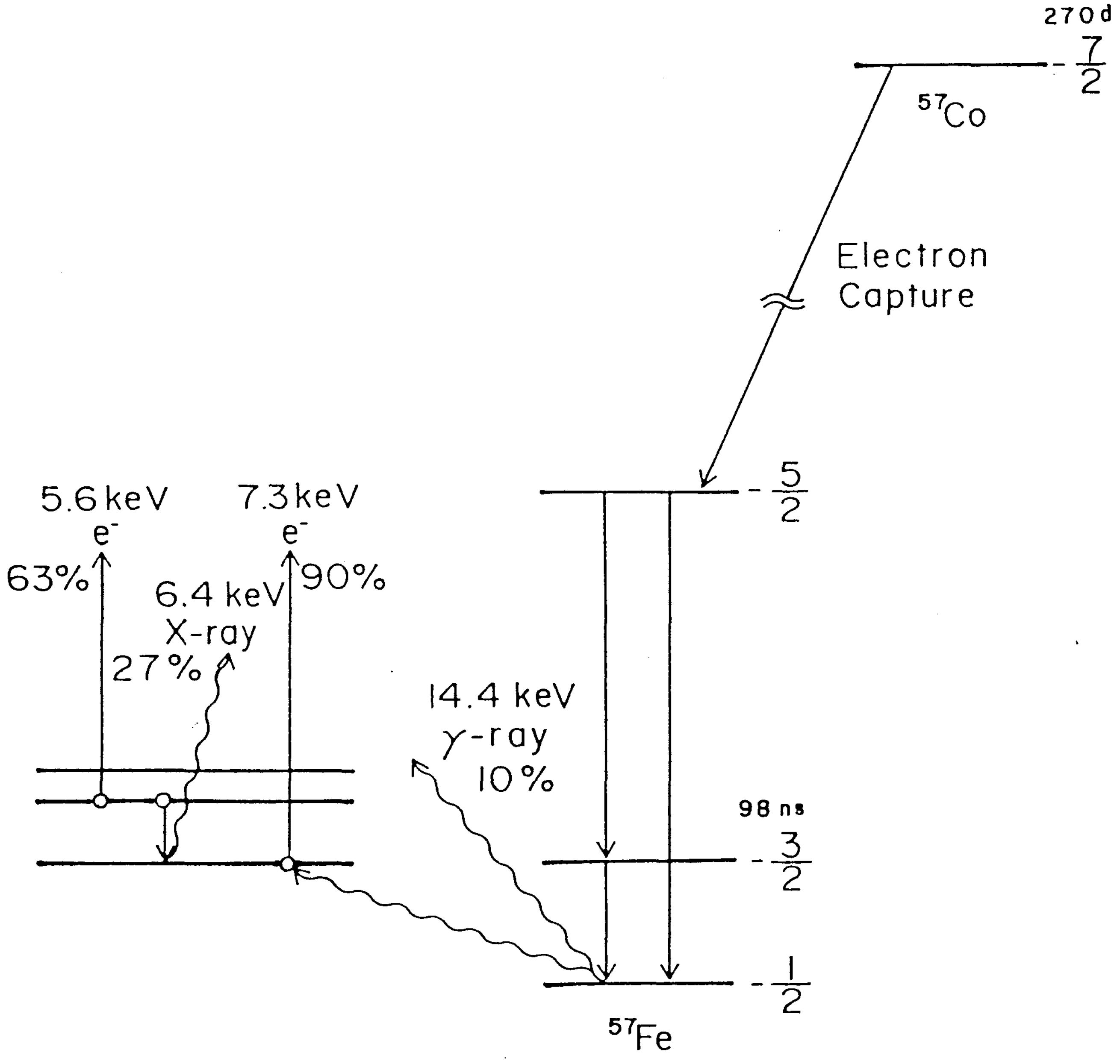

Fig. 1-6. A decay scheme of ^{57}Fe$^{21,22)}$. The energy levels of the nucleus are described at the right hand side and the atomic energy levels of electrons are at the left hand side.

electric transition.

After the internal conversion process, the electron hole is created in the inner electron shell. To fill up this electron hole, two competitive processes will be taken place. One is the Auger effect. Two electrons at the outer electron shell (L-shell in Fig. 1-6) are involved to the Auger effect. One electron falls into the hole at the inner shell and the other electron is emitted with the excess energy, which is called as Auger electron. The other is the characteristic X-ray emission by the transition of the electron at the outer shell to the hole. The ^{57}Fe atom having the electron hole at K-shell escapes from the excited state by the Auger effect with the probability of 63 % and by the emission of characteristic X-ray emission with 27 %.

The decay scheme of the ^{119}Sn nucleus is shown in Fig. 1-7. In the case of ^{119}Sn, the energy of the Mössbauer transition (I = 3/2 to 1/2) is smaller than that of the biding energy of the K-shell electron so that the K-shell electron is never emitted by the internal conversion process.

1.4 Backscattering Mössbauer spectroscopy[21)]

Mössbauer spectra are usually taken by collecting transmitting γ-ray through the specimen absorber (Fig. 1-8). γ-ray which absorbed in the absorber by Mössbauer effect is reemitted isotropically after its life time. So the transmission of γ-ray at resonant energy is lower than that at non-resonant energy and the absorption line appears in Mössbauer spectrum measured by transmission geometry.

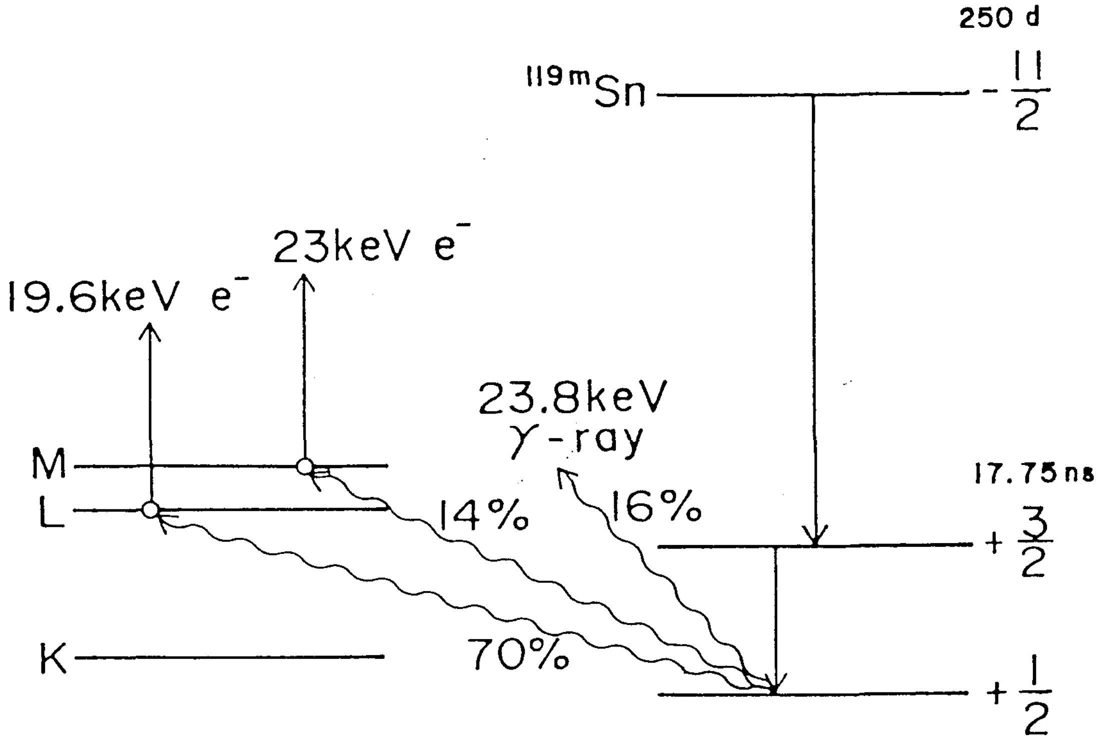

Fig. 1-7. A decay scheme of ^{119}Sn$^{21,22)}$. The energy levels of the nucleus are described at the right hand side and the atomic energy levels of electrons are at the left hand side.

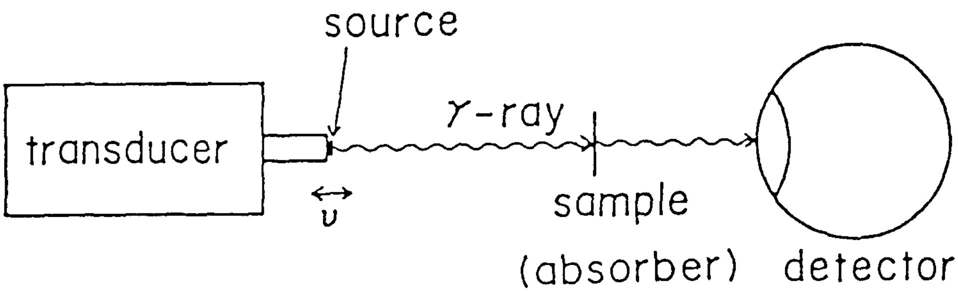

TRANSMISSION GEOMETORY

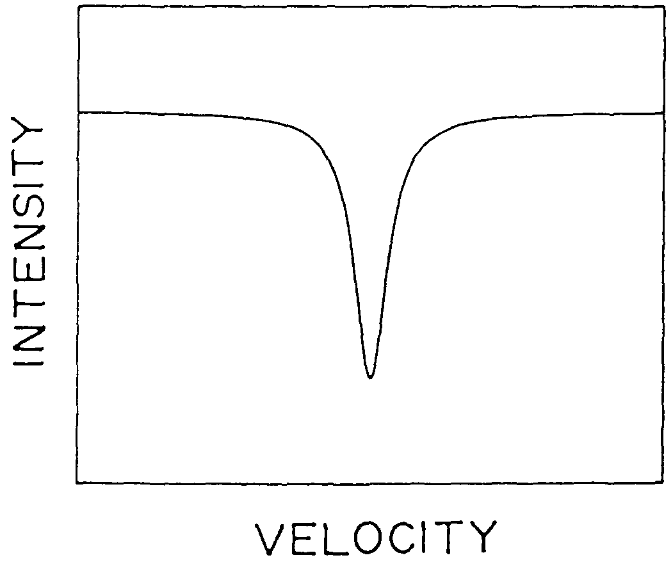

Fig. 1-8. A schematic diagram of the transmission Mössbauer measurement and the resonant absorption line.

The collection of γ-ray scattered by the absorber also makes it possible to construct Mössbauer spectrum. Figure 1-9 shows the backscattering geometry of Mössbauer measurement. The intensity of detected γ-ray on resonance is larger than that of off resonance, where no γ-ray is detected in the ideal case such as γ-ray backscattered by only Mössbauer resonance. This means the backscattering geometry can achieve the higher signal to noise ratio than in the case of transmission geometry. Another good point of the backscattering Mössbauer spectroscopy is that its measurement can be performed for the specimen without the deformations such as the rolling or grinding. When the specimen is measured by the transmission Mössbauer spectroscopy, the thickness of the specimen must be enough thin that Mössbauer γ-ray can be transmitted.

Conversion electrons and the characteristic X-ray are emitted from the absorber, in which the resonant nuclei are excited by Mössbauer effect, with the higher probability than the reemission of γ-ray. In the case of transmission geometry, the solid angle for the γ-ray detection is almost 4π because the scattered γ-ray is emitted isotropically. In the case of backscattering geometry, it is generally smaller than 2π by the structural limitation of the counter. Specially designed detector in order to cover the lower solid angle of the detector is favorable to detect the electrons and the X-ray in Mössbauer measurement by the backscattering geometry.

1.5 Conversion electron Mössbauer spectroscopy (CEMS)[1-3]

Conversion electron Mössbauer spectroscopy (CEMS) is the one

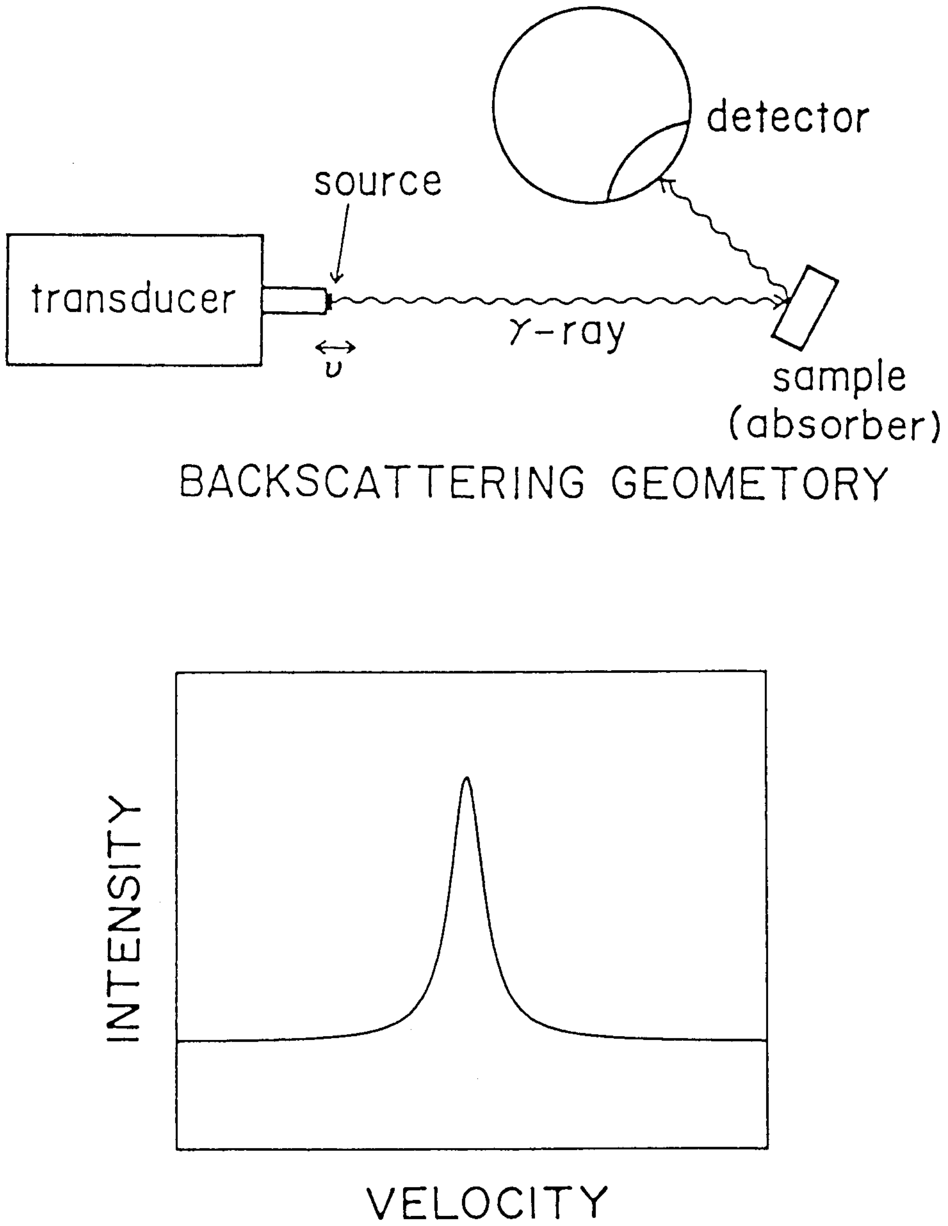

Fig. 1-9. A schematic diagram of the backscattering Mössbauer measurement and the resonant emission line.

of the backscattering Mössbauer measurements. Mössbauer spectrum is constructed by collecting the internal conversion electrons. An additional detection of Auger electrons emitted by following the internal conversion process makes the counting rate of CEMS higher.

The detectable area of CEMS is limited just around the surface of materials because of the small straggling range of the conversion electron. Only electrons which are generated by the internal conversion process at the very shallow part of materials can emerge from the surface and will be detected by the counter. 7.3 keV conversion electron of ^{57}Fe Mössbauer effect has the effective range of about 100 nm in metallic iron and ^{57}Fe CEMS spectrum contains the microscopic information at shallow parts below 100 nm from the surface of materials. CEMS can measure the surface layers of materials with high selectivity and it is known as one of the most powerful tools to study the microscopic properties around the surface of materials.

The depth selective CEMS measurement can be possible if the information on the relationship between the traveling distance of electrons and the amount of its energy losses is already known[22,23]. This method is known as depth selective CEMS (DCEMS). One of the benefits of DCEMS is the non-destructiveness to measure the microscopic property at various depth near the surface. But the special electron counter is needed for the measurement of DCEMS in order to select the energy of electrons with the energy resolution of higher than 100 eV.

For CEMS measurements, the use of the specially designed electron counter containing the specimen scatter is necessary to detect electrons. If one does not hope the high energy selectivity, the gas proportional electron counter is advantageous to the detection of electron for the high counting efficiency and its easy handling.

In this theses, CEMS were applied to study the physical and chemical properties around surfaces of several materials and the utility of CEMS for the measurement of surface properties are demonstrated, utilizing the specially designed gas proportional electron counters.

1.6 References

1. J.J.Spijkerman, "Mössbauer Effect Methodology Vol.7", Ed. by I.J.Gruverman, Plenum, New York, (1971), p.85.
2. S.Nasu, Bul. Jpn. Inst. Metals, 26(1987)95.
3. S.Nasu, J. Magn. Soc. Jpn., 13(1989)38.
4. K.Hashiura, J. Jpn. Inst. Metals, 16(1977)681.
5. M.Sagawa, S.Fujimura, H.Yamamoto and Y.Matsuura, J. Appl. Phys., 55(1984)2083.
6. H.Franufelder, "The Mössbauer Effect", W.A.Benjamin, New York, (1963).
7. G.K.Wertheim, "Mössbauer Effect : Principle and Applications", Academic Press, New York, (1964).
8. N.N.Greenwood and T.C.Gibb, "Mössbauer Spectroscopy", Chapman and Hall, London, (1971).
9. T.Sano, "Mössbauer Spectroscopy : The Chemical Applications", Kodansha, Tokyo, (1972).
10. U.Gonser and C.Schneider, "Mössbauer Spectroscopy Applied to Inorganic Chemistry Vol.3", Ed. by G.J.Long and F.Grandjean, Plenum, New York, (1989), p.1.

11. R.L.Mössbauer, Z.Physik, 151(1958)124 ; R.L.Mössbauer, Naturwissenschaften, 45(1958)538.

12. "Mössbauer Spectroscopy", in Topics in Applied Physics Vol.5, Ed. by U.Gonser, Springer-Verlag, New York-Heidelberg-Berlin, (1975)
; "Mössbauer Spectroscopy II", in Topics in Current Physics Vol.25, Ed. by U.Gonser, Springer-Verlag, Belrin-Heidelberg-New York, (1981).

13. W.Kündig, Nucl. Instrum. Methods, 48(1967)219.

14. C.Kimball, W.D.Gerber and A.Arrott, J. Appl. Phys., 34(1963)1046.

15. Y.Endou and Y.Ishikawa, J. Phys. Soc. Jpn., 30(1971)1614.

16. Y.Tsunoda, J. Phys. Condenced Matter, 1(1989)10429.

17. H.Yukawa and S.Sakata, Proc. Phys.-Math. Soc. Jpn., 17(1938)467.

18. E.Fermi, "Nuclear Physics", the University of Chicago Press, Chicago, (1949).

19. E.Segrè, "Nuclei and Particles", W.A.Benjamin, New York, (1965).

20. E.Browne et al., "Table of Isotopes 7th edition", Ed. by C.M.Lederer and V.S.Shirley, John Wiley & Sons, New York, (1978).

21. F.E.Wagner, J. de Phys., C6(1976)673.

22. U.Bäverstam, C.Bohm, T.Ekdahl, D.Liljequist and B.Ringström, "Mössbauer Effect Methodology Vol.9", Ed. by I.J.Gruverman, C.W.Seidel and D.K.Dieterly, Plenum, New York, (1974), p.259.

23. T.Shigematsu, H.-D.Pfannes and W.Keune, Phys. Rev. Lett., 45(1980)1206.

CHAPTER II. ELECTRON COUNTER

2.1 Gas proportional counter[1,2)]

The gas proportional counter is widely used for the detection of the low energy radiations. The structure of a typical gas proportional counter is shown in Fig. 2-1. The counter has an anode wire at its center and the inside of the counter is filled up with the gas to detect the energetic particles and rays. The detection gas is the mixture of the inert gas and the small amount of the multiatomic molecule gas. The gases are chosen by the kind of the particles or rays to be detected. For instance, the helium and C_4H_{10} mixture gas is used for the detection of electrons and the argon and CH_4 mixture gas for γ-ray.

The principal operation of the gas proportional counter is described by the following process. The radioactive rays ionize the inert gas atoms (the primary ionization) and the number of these atoms are proportional to the energy of incident rays. The positive high voltage about 1 - 2 kV is applied to the anode wire and the electrons generated by the primary ionization are accelerated to the anode by the electric field. On the way to the anode, the accelerated electrons cause the secondary ionization of the inert gas atoms. The cascade of this secondary ionization multiplies the number of electrons over 10^3 times of those by the incident rays and an electric pulse is detected as the gathering of these electrons at the anode. This process is known as the gas multiplication. The gas multiplication does not contain the source generating the noise in its process, so the gas proportional counter can multiply the signal of the

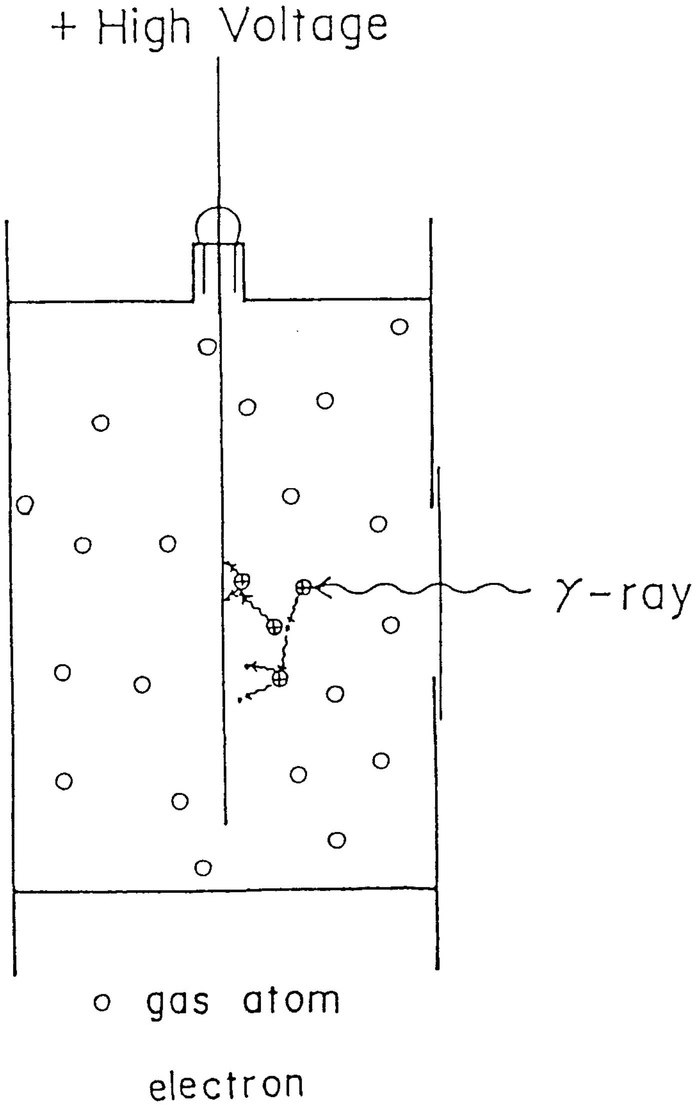

Fig. 2-1. A schematic structure of the gas-filled counter

incident rays with the lower noise than other detectors. The addition of the multiatomic molecule gas stabilizes its operation of gas proportional counter. The small ionizing energy of the multiatomic gas will absorb a part of the energy of the secondary ionization and suppress the continuous electric discharge originated from the excess gas multiplication. These multiatomic gas is called as the quenching gas.

The operation of the gas-filled counter depends on the voltage applying to the anode. The dependence of the factor of gas multiplication to the anode voltage is shown in Fig. 2-2. In the region II in Fig. 2-2, the amount of the electric charge collected at the anode corresponds to the number of electrons created by the primary ionization. In the region III in Fig. 2-2, the number of electrons created by the primary ionization is multiplied by the gas multiplication and this region is used for the gas proportional counter. In these regions, the height of the detected pulse is proportional to the number of electrons created by the primary ionization, which corresponds to the energy of the incident radioactive rays. It is possible to measure not only the amount of the radioactive ray but also its energy. At the high voltage region of V, the amount of the electric charge collected at the anode is not proportional to the number of primary electrons any longer. The Geiger-Muller counter is used at this region to get the high sensitivity to the radioactive rays at the cost of the energy resolution.

2.2 Electron counter for CEMS

CEMS has a lot of advantage to study the microscopic proper-

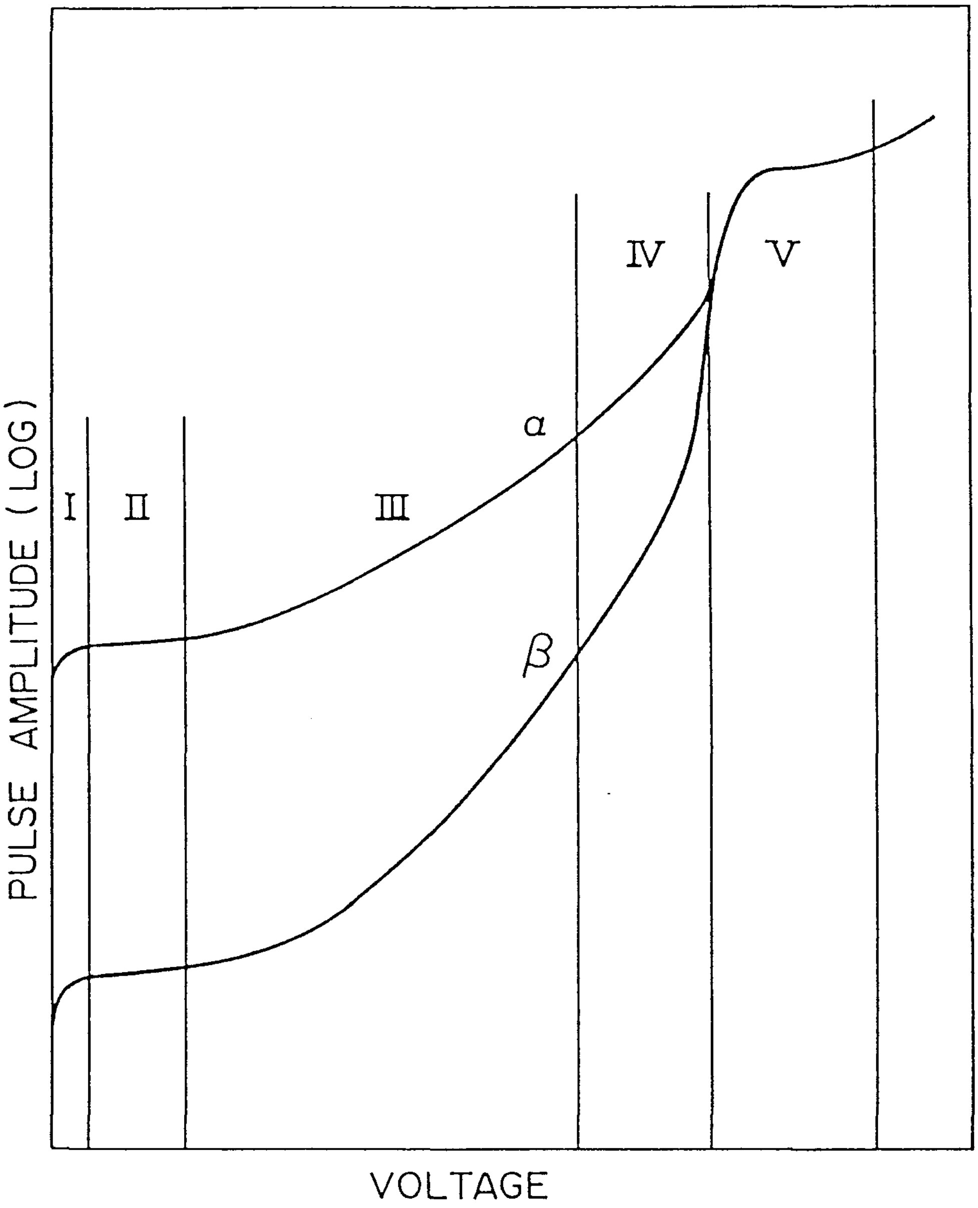

Fig. 2-2. Pulse amplitude detected at the anode vs applied anode voltage of the gas-filled counter for α and β particles. The region III is called as proportional range and used for the gas proportional counter[1].

ty around surface of materials. But it is not applied widely because it requires some specially designed counter for the detection of electrons. The electrons are so strongly absorbed in solids that the sample has to be enclosed in the counter to detect electrons directly. If the energy resolution higher than a few keV is not required, the gas proportional counter is valuable to detect the conversion and Auger electrons. The gas proportional counter has almost 100 % efficiency to detect low energy electrons under a small background noise. The structure of the counter which was used in present investigations is quite simple and it does not need ultra high vacuum at the measurement, compared to the electron spectrometer used for nuclear and atomic physics.

The gas proportional counter to detect electrons has been manufactured already in our laboratory3). But it has several disadvantages. The small volume of this counter makes it impossible to carry out CEMS measurement for bulky samples. The loose airtight structure prevents the stable operation of the counter by the admixture of impurity gases. A counter is newly manufactured in this study in order to improve these points. The electron counter which can operate at low temperature is also developed in order to CEMS measurement at low temperature. The details of these counters are described in the following sections.

2.2.1 Room temperature measurements

Figure 2-3 shows the cross-sectional view of the newly developed electron counter for CEMS measurement at room tempera-

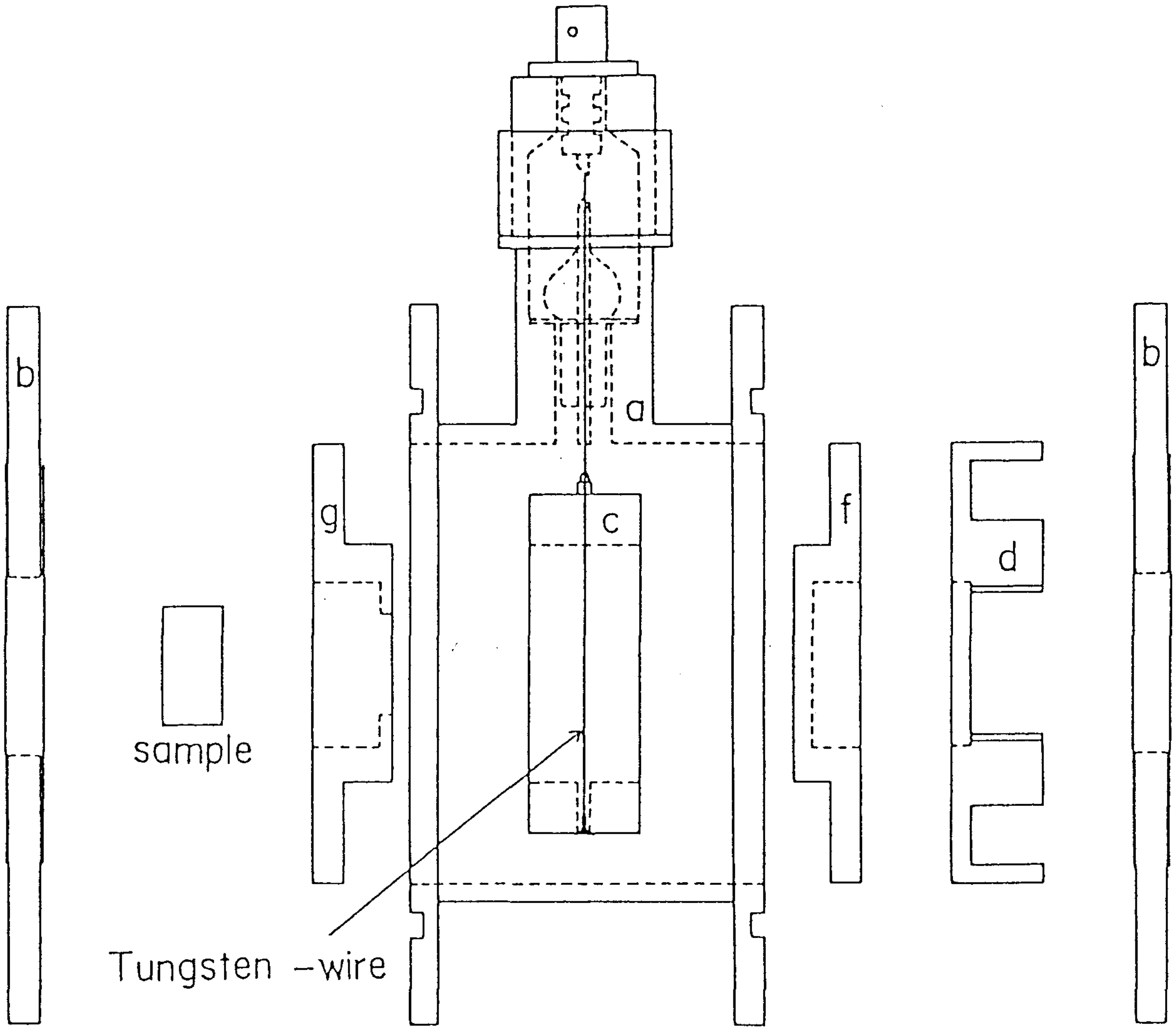

Fig. 2-3. Cross sectional view of the newly developed electron counter for the CEMS measurement at room temperature.

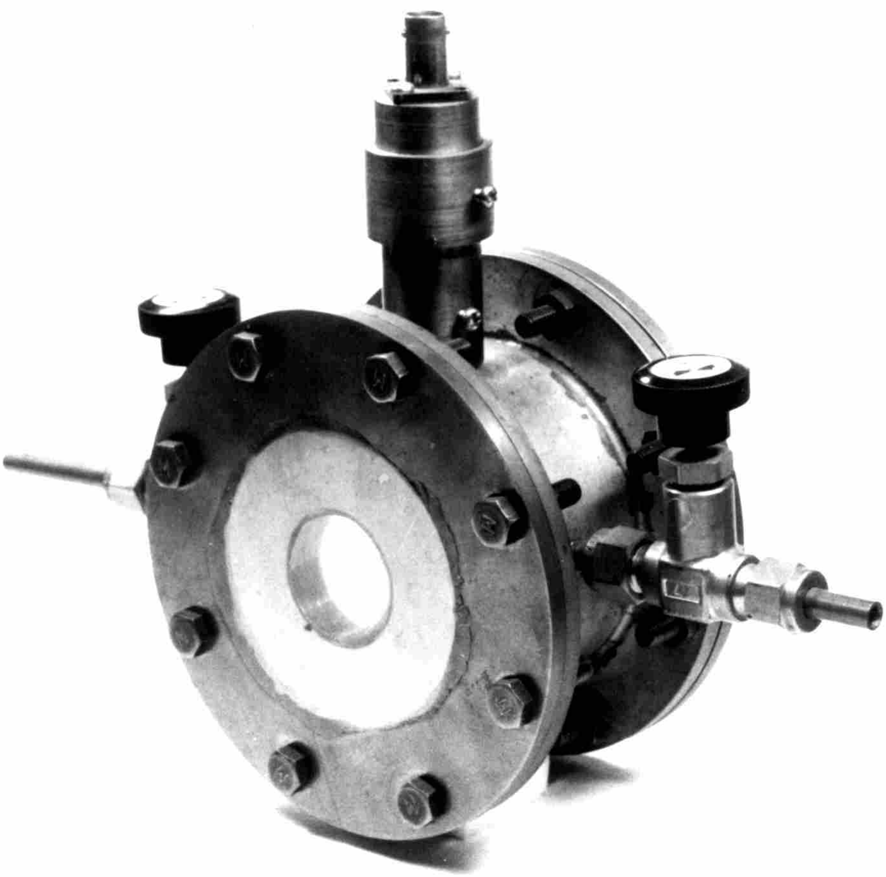

Photo. 2-1. Newly developed electron counter for the CEMS measurement at room temperature.

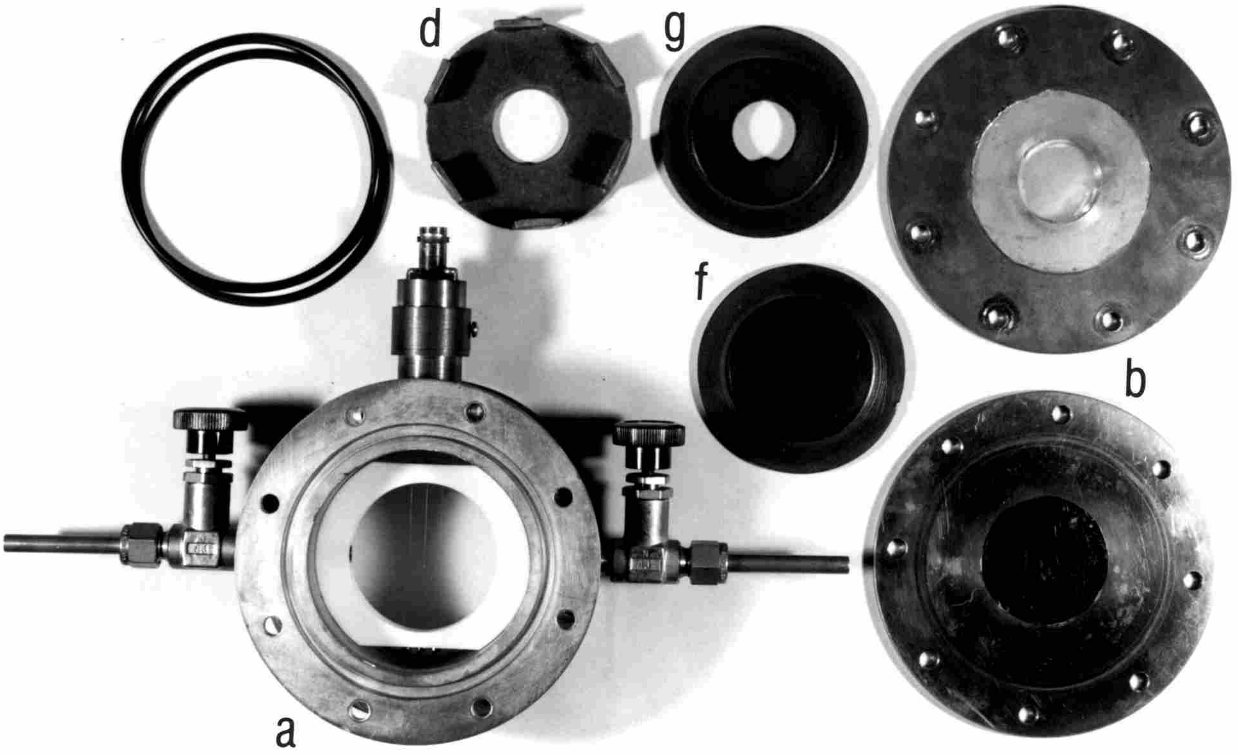

Photo. 2-2. Components of the newly developed electron counter for the CEMS measurement at room temperature.

ture. This is the gas-flow type proportional counter of which the detectable solid angle is 2π. The main body (a) of the counter has flange structures at each end, where the disks (b) are fitted by nuts and bolts with O-ring seals (h). The each disk has the window of 20 mm ϕ at the center. The window is covered with two films. One is the transparent mylar film adhered on the outside of the disk to keep the airtight. The other is the metallized mylar film on the inside to prevent the incidence of lights which creates photoelectrons. These body and disks are made of brass. At the center of the counter body, the tungsten wire of 40 μm in diameter for the anode is extended through the acrylic holder (c) having doughnut shape. The sample is placed at the distance of 3 mm from the tungsten wire by the acrylic sample holder (g). At the incident side of γ-ray, the acrylic dummy holder (f) is set into the holder (c) to maintain the symmetry of the electric field. This dummy holder also performs the role to filter off the characteristic X-ray from the γ-ray source and its thickness is chosen to the suitable value. The unnecessary X-ray incident into the operating area of counter will generate photoelectrons which make the lower signal to noise ratio of the counter. The lead shield (d) is also set in the counter to cut unnecessary γ-ray and X-ray. The surface of acrylic holders of (g) is covered with the graphite coating in order to keep the charge neutrality of the sample. The surface of the dummy holder of (f) is also covered with the graphite coating to maintain the symmetrical condition around the anode wire. Two valves are fixed on the cylindrical side of the main body in order to fill up the inside with the detection gas or flow the gas during the measurement. The counter is operated with about 3 cm^3/min flow of Q gas (99 % He + 1 % C_4H_{10} mixture).

Figure 2-4 shows the energy spectrum of this counter at room temperature. The area of the spectrum at the low energy is constructed by the photoelectrons, which make the signal to noise ratio of the CEMS spectrum worse. The low energy area of the spectrum, which is hatched in Fig. 2-4, was cut off by the discriminator in the CEMS measurements.

2.2.2 Low temperature measurements

Mössbauer measurement at low temperature provides a lot of valuable information about magnetic and local vibrational states around the probe atoms. Transmission Mössbauer measurement at low temperature can be performed by using the cryostat including the source and/or the sample. In the case of CEMS, it is rather difficult to perform the measurement at low temperature than transmission measurement because the detector containing the specimen should be refrigerated additionally.

The CEMS measurements at low temperature were successfully performed using the tubular electron multiplier and channeltron for the detector of electrons[4,5]. The gas proportional counter has the problem of the condensation of quenching gas at low temperature and it seemed that the operation of the gas counter would not be stable at low temperature. Some groups have succeeded CEMS measurement at low temperature applying the gas proportional counter. Isozumi et al.[6] have developed the gas-filled electron counter operating at liquid helium tempera-

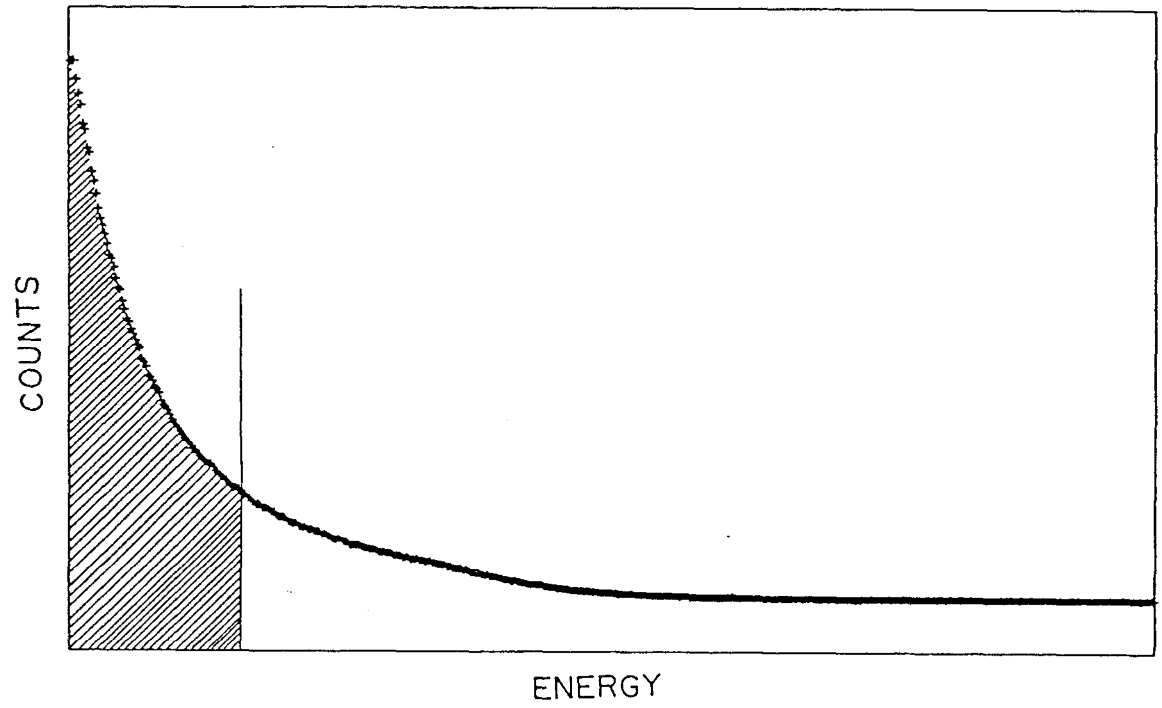

Fig. 2-4. Energy spectrum of the newly developed electron counter for the CEMS measurement at room temperature. The hatched area is cut off by the discriminator at the CEMS measurement.

ture. Kastner et al.[7)] have reported the stable operation of the gas-flow proportional counter from 50 K to 370 K. These reports show the utility of the gas counter for CEMS measurement at low temperature.

Figure 2-5 shows the cross-sectional and top views of the electron counter designed for CEMS measurement at 77 K. Its fundamental structure is similar to that of the electron counter for the room temperature measurement. It is small enough to set into the cryostat. In seals are used to keep the airtightness at low temperature instead of O-ring seals. The temperature of the sample is determined by the resistance of Pt resister placed on the upper plane of the counter. The mixture of helium and methane (95.8 : 4.2) or helium and carbon monoxide (9 : 1) was used for the detection gas to avoid the condensation of quenching gas[8)]. At these mixing ratios, the partial pressure of the quenching gas is smaller than the vapor pressure at 77 K (Fig. 2-6). The gas was filled up before the cooling of the detector and was not flowed during the measurement to acquire the stable operation for long period.

The diagram of the electron counter and the cryostat is shown in Fig. 2-7. The inside space of the cryostat is filled up with the helium gas about 5 Torr at room temperature and the counter is cooled down by the thermal conduction of the helium gas. This cooling method makes the counter cooled down to about 180 K. The cryostat also has the capillary and the direct cooling by liquid nitrogen is possible. The energy spectrum of this electron counter is shown in Fig. 2-8 measured at 190 and 100 K.

α-Fe_2O_3 was measured by CEMS at low temperature to demon-

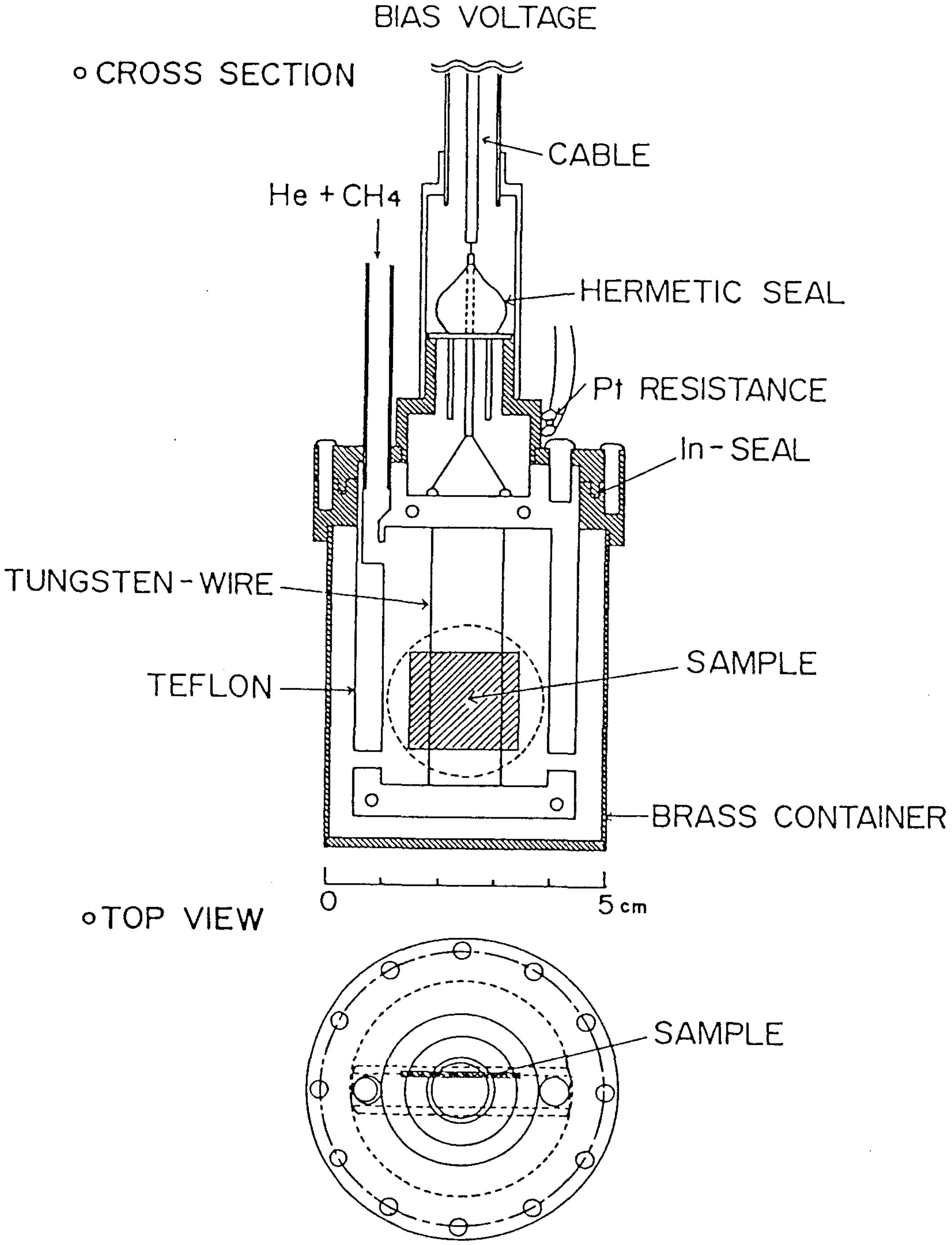

Fig. 2-5. Cross sectional and top views of the newly developed electron counter designed for the CEMS measurement at low temperature.

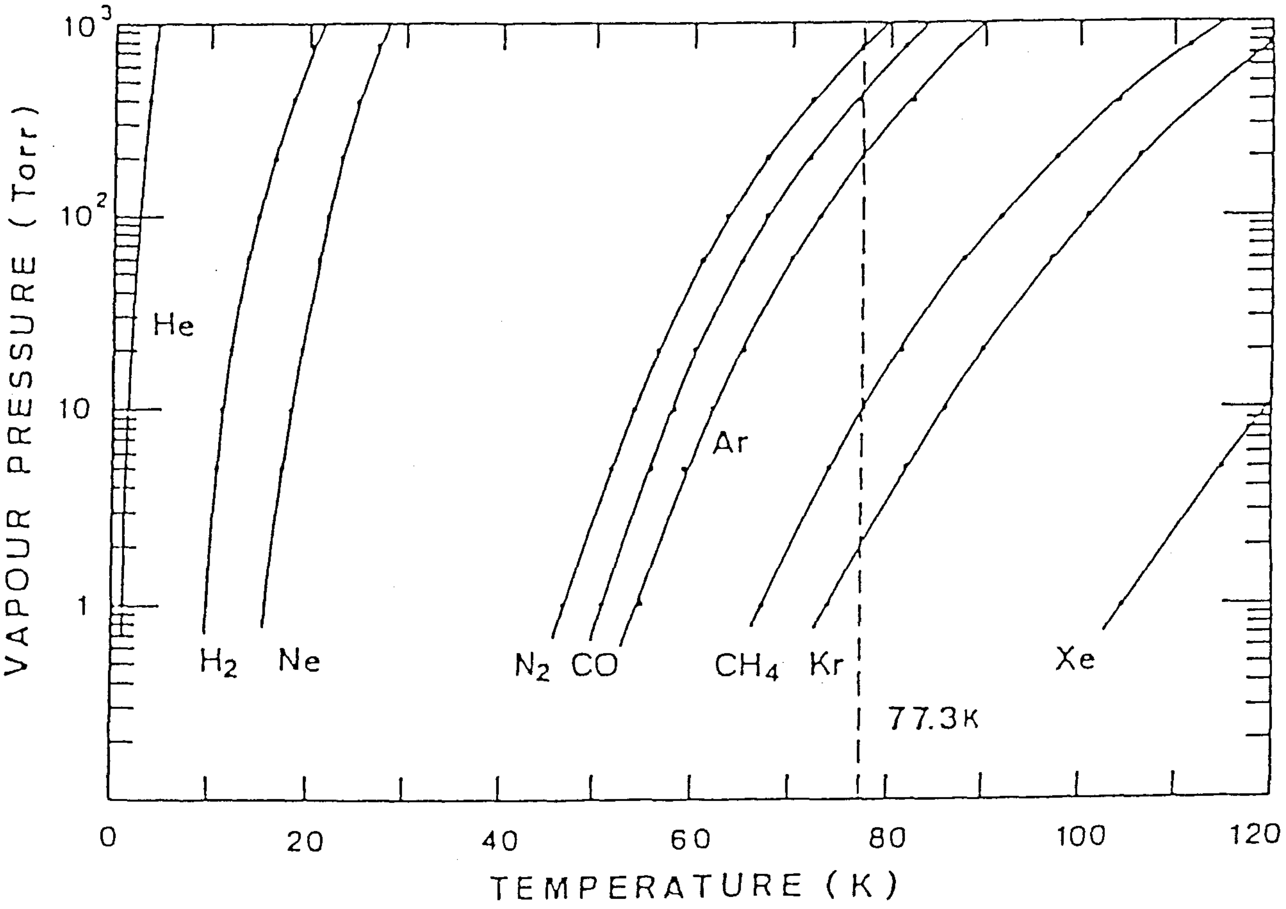

Fig. 2-6. Saturated vapor pressure of various molecules.

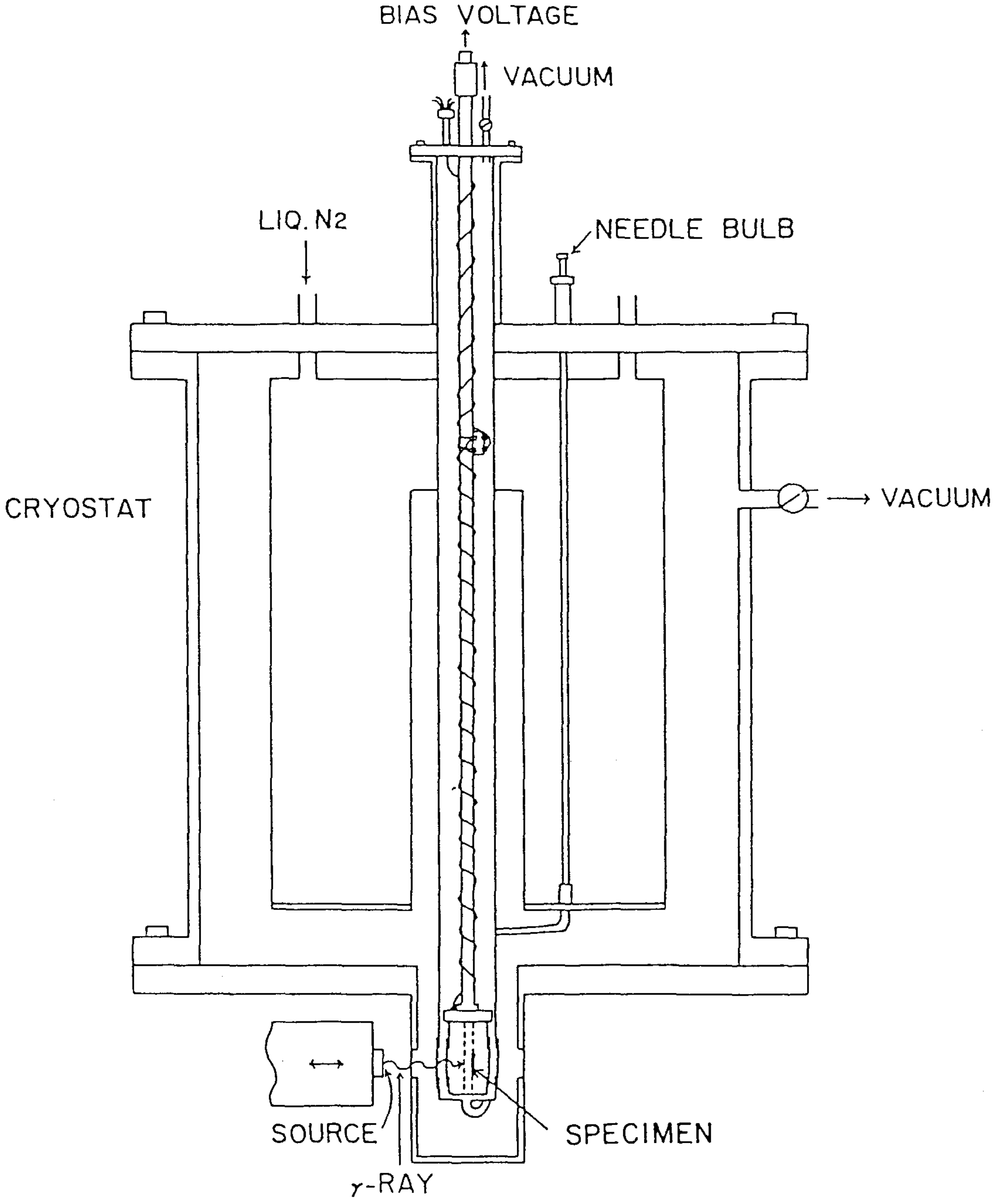

Fig. 2-7. A diagram of the newly developed electron counter and the cryostat for the low temperature measurements.

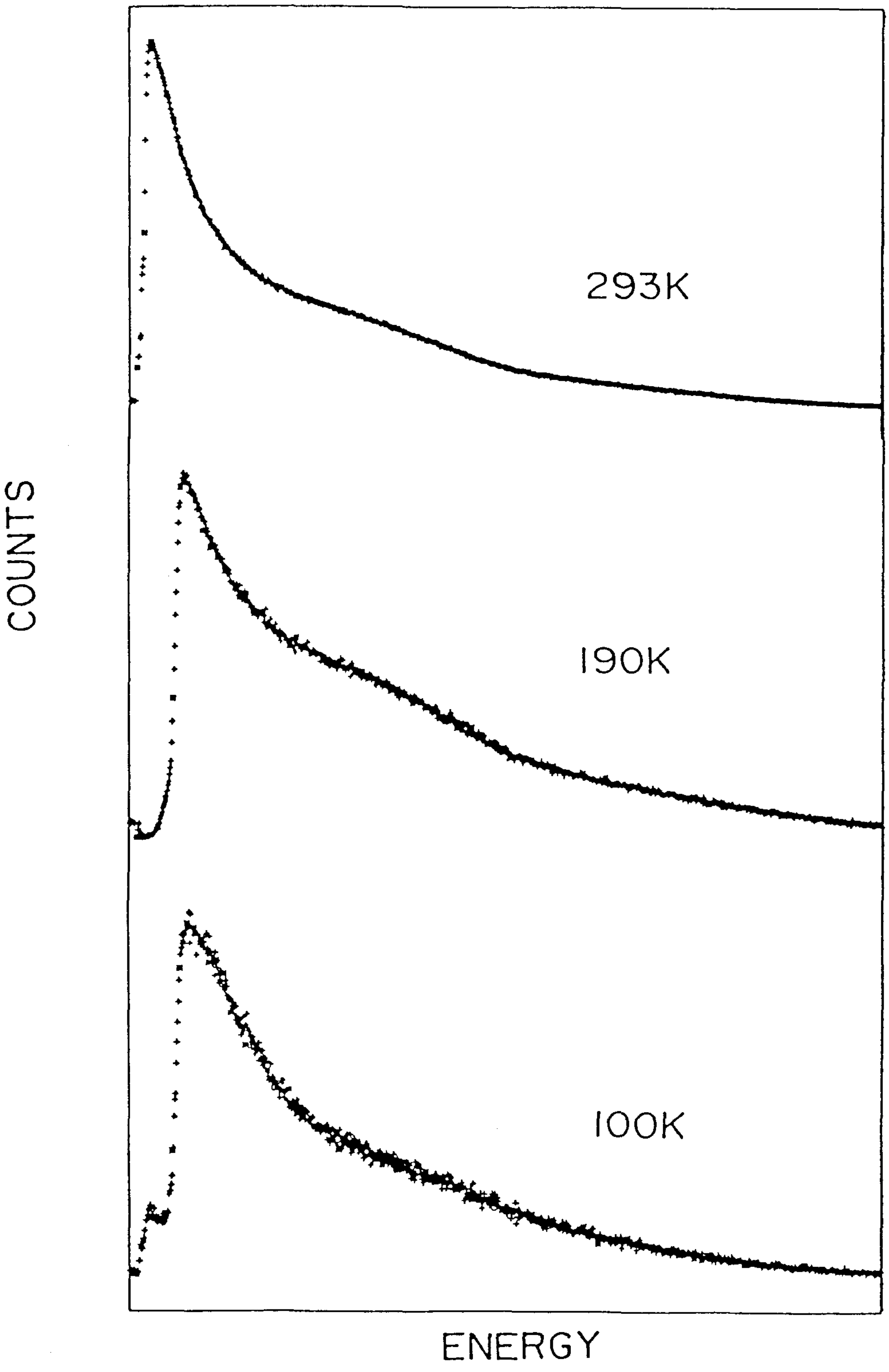

Fig. 2-8. Energy spectra of the newly developed electron counter designed for the CEMS measurement at low temperature.

strate the performance of this counter. α-Fe_2O_3 is well known for its spin-flip transition by temperature and pressure, namely Morin transition[9,10]. Figure 2-9 shows the spin structures below and above the transition temperature. The transition temperature is about 260 K at 1 atm. The principal axis of the electric field gradient is always parallel to c-axis of the crystal. On the other hand, the direction of spin is parallel to c-axis above transition temperature, but is perpendicular to c-axis below its temperature. When θ is the angle between the principal axis of electric field gradient and the direction of spin, the value of electric quadrupole splitting will be denoted by the next equation assuming $\eta = 0$,

$$Q.S. = e^2qQ(1-3\cos^2\theta)/8.$$

The sign of electric quadrupole interaction is directly reflected at the asymmetry of the 6-line pattern in Mössbauer spectrum. If the sign of the electric field gradient is negative, the distance between the first and the second peaks of the 6-line pattern is larger than that between the fifth and the sixth. If it is positive, vice versa.

Figure 2-10 shows CEMS spectra of α-Fe_2O_3 measured at 273 K and 190 K. The distance between the left two peaks is larger than that between right two peaks at 273 K and the relationship of two distances is reversed at 190 K. The values of isomer shift and electric quadrupole splitting are +0.36 and -0.23 mm/s at 293 K and +0.44 and +0.36 mm/s at 190 K. These are well agreed with the reported values obtained from the transmission Mössbauer measurements[11].

These results show the positive proof of the operation of

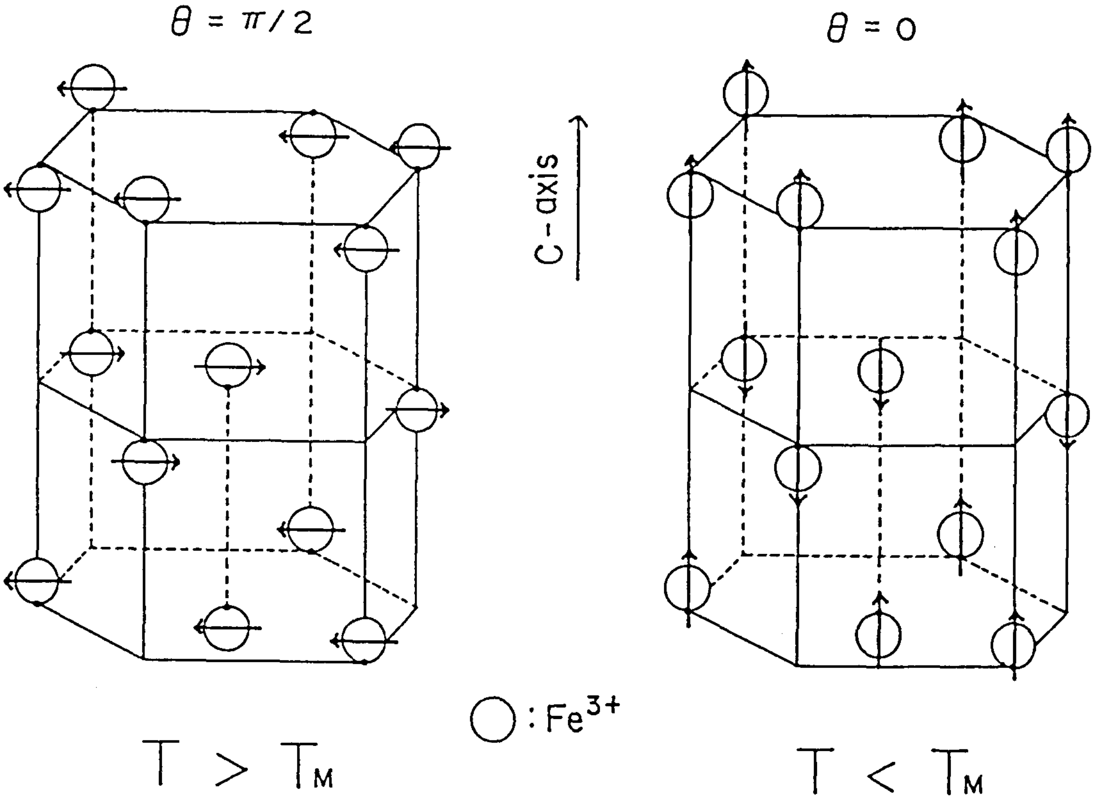

Fig. 2-9. Spin structure of $\alpha\text{-Fe}_2\text{O}_3$ above and below Morin temperature T_M. θ is the angle between the direction of the spin and the principal axis of the electric field gradient, which is parallel to the c-axis of the crystal.

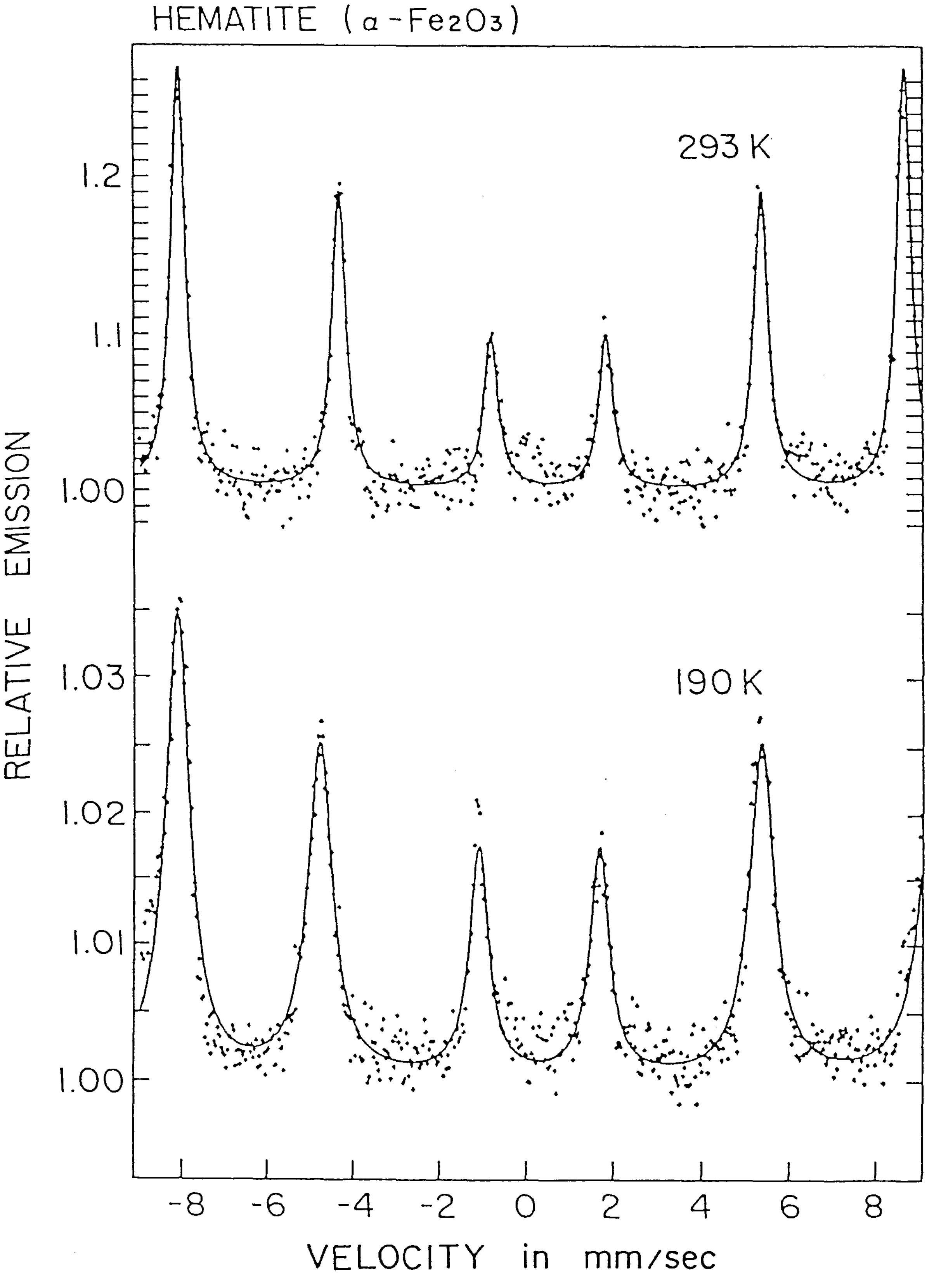

Fig. 2-10. ^{57}Fe CEMS spectra of α-Fe_2O_3 measured at 190 and 293 K. At 293 K, the distance between the first and second peaks is larger than that between the fifth and sixth. At 190 K, the relation of these distances is reversed. Velocity scale is relative to α-Fe at room temperature.

the electron counter at low temperature. This electron counter, however, has some defects. One is the bad cooling rate which is originated from the large heat capacity of the counter and the limitation of the thermal conductivity by the small amount helium gas. The second is that the handling of the counter is not so easy because of In sealing. The third point is the indirect measurement of the temperature of the sample. But the temperature at the counter wall should be very close to the temperature of the specimen because helium gas having a high thermal conductivity is filled up in the counter. The accomplishment of this counter will promise the new application of CEMS to various fields.

2.3 References

1. K.Ohno et al., "Houshasen Sokutei", Ed. by S.Iida et al., Asakure Shoten, Tokyo, (1967).
2. S.Kishimoto, Master Thesis, Kyoto University, (1984).
3. S.Nasu and F.E.Fujita, Hyp. Int., 29(1986)1279.
4. O.Massenet, Nucl. Instrum. Methods, 153(1978)419. ; O.Massenet and H.Daver, Solid. State Commun., 25(1978)917.
5. J.A.Sawicki, T.Tyliszczak and O.Gzowski, Nucl. Instrum. Methods, 190(1981)433.
6. Y.Isozumi, S.Kishimoto, R.Katano and H.Takekoshi, Rev. Sci. Instrum., 58(1987)293.
7. A.Kastner, G.Lugert and G.Bayreuther, Hyp. Int., 42(1988)1145.
8. S.Kishimoto, Y.Isozumi, R.Katano and S.Shimizu, Nucl.

Instrum. methods, A225(1987)213.

9. R.W.Vaugham and H.G.Drickamer, J. Chem. Phys., 47(1967)1530.

10. C.L.Bruzzone and R.Ingalls, Phys. Rev. B, 28(1983)2430.

11. N.N.Greenwood and T.C.Gibb, "Mössbauer Spectroscopy", Chapman and Hall, London, (1971), p.240.

CHAPTER III. APPLICATIONS

3.1 Ion-implantation

3.1.1 Ion-implantation technique[1,2)

When charged particles are accelerated by the electric field and make collision against the target, the effects of these particles on the target depend on the energy of the particles. Figure 3.1-1 illustrates how the accelerated particles affect on the surface layers of the target. At the energy about 10 eV, accelerated particles will be piled up on the target surface and construct the new layers. At about a few keV, these particles will be backscattered by the target atoms accompanying a sputtering of the surface layers of the target. This process is applied to make the ion source vapor of the target atom, to clean the surface of the target and to make a thinner thickness of the target. At the energy over 10 keV, the energetic particles come to get into the inside of the target. The particles which get into the target lose its energy by random collisions with the target atoms and stop at various depth from the surface. The introduction of impurity atoms into target by this process is known as the ion-implantation. Since the collisions with the target atoms are random process, the depth of the implanted atom depends on the initial energy of the particle. This means that the depth of atoms implanted into the target can be controlled by the acceleration energy of ions. The depth of the implanted atoms in the target shows the continuous distribution like Gaussian function even if all atoms are implanted at the same

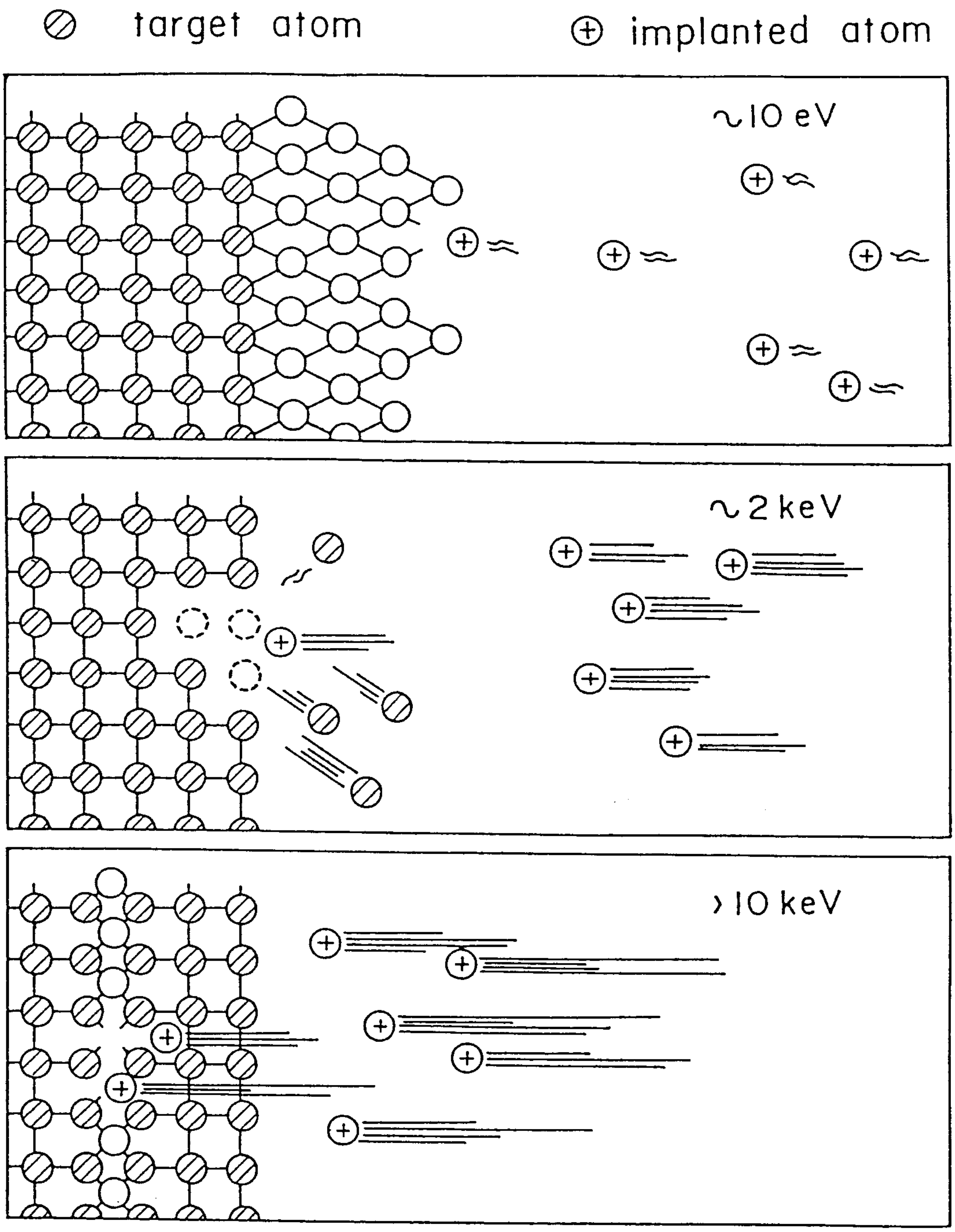

Fig. 3.1-1. Effects of the energetic particles upon the target$^{3)}$.

acceleration energy. In addition, the concentration of the implanted atoms in the target is easily controlled by the dose of the implanted atoms. Also any atom species can be implanted into any kinds of targets by ion-implantation. The ion-implantation technique is advantageous to improve the physical properties around surface for these features.

The ion accelerator and the ion source are needed in order to carry out the ion-implantation. Cockcroft-Walton accelerator is popularly used for the ion implantation of the acceleration energy under 1 MeV. Tandem Van de Graaff accelerator is also available for the implantation at the higher energy about 10 MeV. The ions are generated by applying several techniques such as the microwave oven, sputtering or arc discharge.

Ion-implantation technique has been developed especially in the field of semiconductor in order to dope the impurity atoms into the substrate because this technique can easily control the concentration and distribution of dopant atoms. Recently it was further applied to metals in order to improve the surface corrosion or the wear resistance 4,5) with the development of the accelerators.

As above mentioned, the ion-implantation technique comes to be used for various materials to improve their physical properties around the surface. However, the ion-implantation introduces not only impurities which are ion-implanted foreign atoms but also a large amount of lattice defects. The introduction of the impurities and defects would induce the problems such as their migration, interaction, clustering and formation of non-equilibrium phase. For the study of ^{119}Sn implantation into metals, ^{119}Sn CEMS will provide a microscopic information on the behavior of the implanted Mössbauer atoms and their environment in target metals. Especially, in the case of the implantation into Fe metal, the microscopic information of target ^{57}Fe atoms can also be acquired by ^{57}Fe CEMS.

3.1.2 Experimental procedure

1) ^{119}Sn implantation into Ni and Fe

The targets for ^{119}Sn ion-implantation were chosen to two metals of Ni and Fe. The target foils of 45 µm were prepared by cold-rolling of high purity rods of 5 mm in diameter supplied by Johnson Matthey Chemicals Ltd. The purity of each metal is 99.998 % up for Ni and 99.99 % up for Fe. The rolled foils were electrolytically etched to about 40 µm in thickness by using the electrolytic solution of $H_2SO_4 : H_2O = 3 : 2$ for Ni and $HClO : CH_3COOH : CH_3OH = 10 : 1 : 1$ for Fe in volume fraction. These foils were annealed by suitable ways for each element. The Ni foils were annealed for 8 hrs at 1173 K in the silica tubes under vacuum. The Fe foils were annealed for 2 hrs at 1173 K in the flow of wet H_2 gas. As a final step of the target preparation, these annealed foils were electrolytically etched for about 10 s to remove the surface contaminations.

The ion-implantation was performed by using a Cockcroft-Walton accelerator at Electrotechnical Laboratory, Agency of Industrial Science and Technology, Tsukuba, which is shown in Fig. 3.1-2. The ion-implantations were performed with accelerating energies of 100, 200, 300 and 400 keV and the total doses

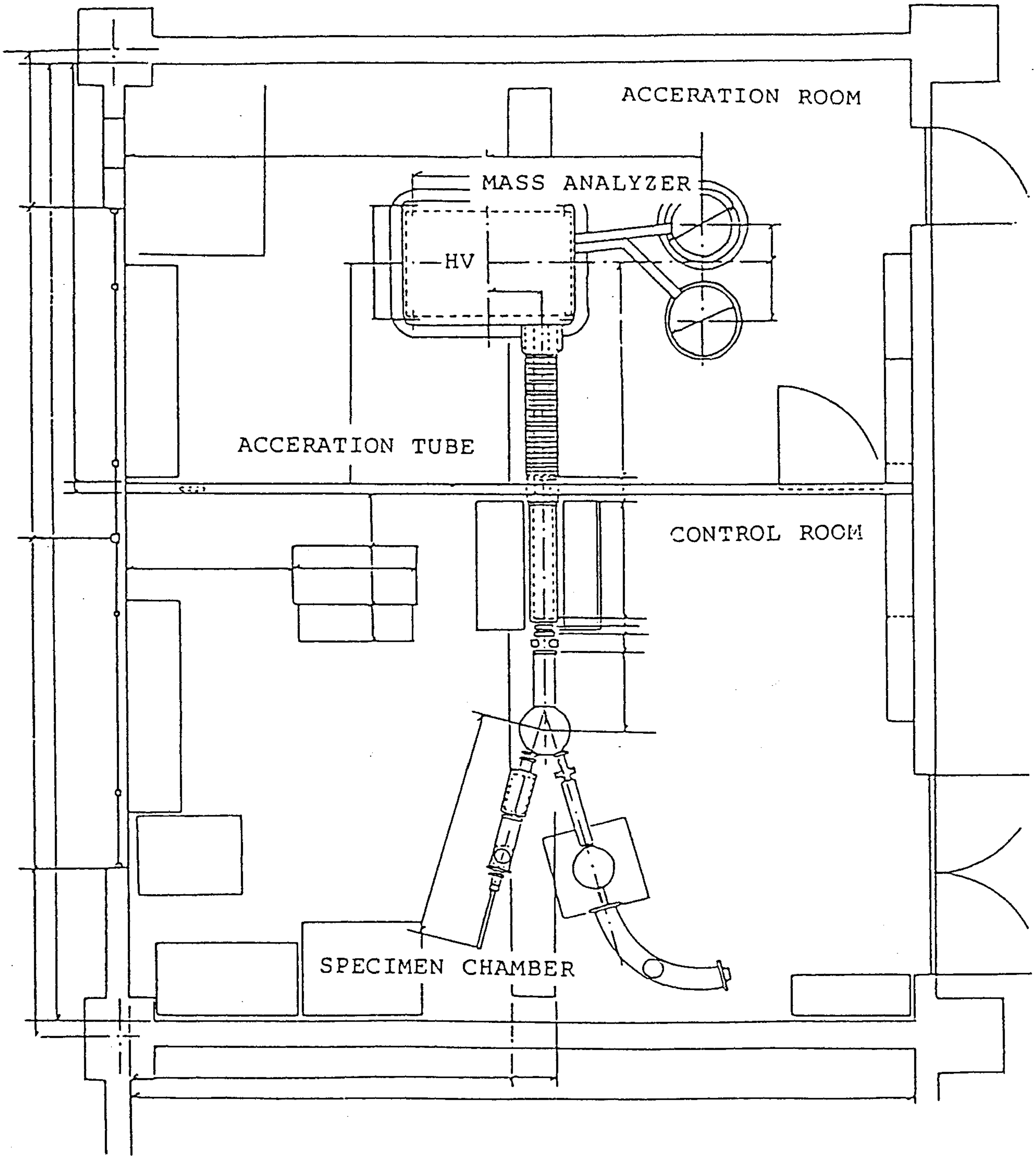

Fig. 3.1-2. Cockcroft-Walton type ion accelerator in Electrotechnical Laboratory, Tsukuba.

of the implantation were 5×10^{15}, 1×10^{16} and 5×10^{16} ions/cm^2.

The foils were mounted on the copper base sample holder inside of the target chamber using an electrically conductive paste. After the implantations, the foils were removed from the copper base dissolving the paste by acetone.

The implantations were done at room temperature. The temperature of the foils was not measured during implantations, because the electric noise arising from the ion collision made impossible to measure the temperature by the thermocouple. However, the temperature of the copper base where the foils were mounted just after implantation was below 323 K in all cases. The maximum rise of the temperature of the foils during implantation would be lower than 50 K.

2) CEMS measurements

^{119}Sn CEMS measurements were performed at room temperature by using the gas flow type electron counter which was newly developed to gain the higher efficiency of count-rate. About 3 cm^3/s flow of Q gas (99 % He + 1 % CH_4) was used for the detection gas during CEMS measurements. All CEMS spectra were recorded by the combination of a velocity transducer and a multichannel analyzer operated in time mode. The transducer was driven under the constant acceleration mode. The back and forth motion of the transducer changes the distance between the source and the detector and this leads to the change of the counting rate of the effective γ-ray detection at each Doppler velocity. By this effect, the base line of the spectrum will be curved like a quadratic line. In order to reject the convex of the base

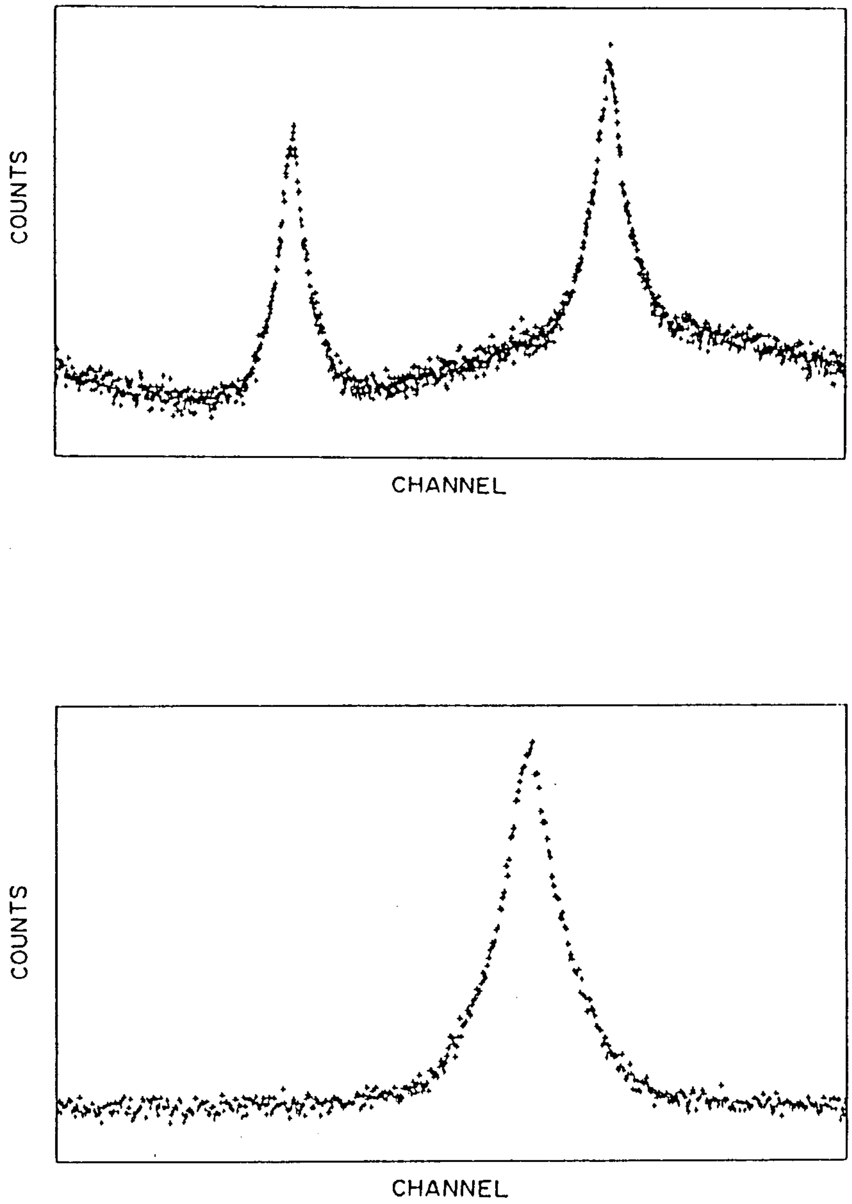

Fig. 3.1-3. A rare and the folded ^{119}Sn CEMS spectrum obtained from the ^{119}Sn implanted into Ni measured at room temperature.

line, the transducer was driven by the triangular wave function. Under this condition, the spectrum is constructed by two continuous spectra whose base lines are symmetrically quadratic lines of up and down convex. The spectrum whose base line is flat can be obtained by folding the spectrum at a certain channel. The optimum folding point of the spectrum is searched by the computer with accuracy of 1/100 channel. The spectra before and after the folding procedure are shown in Fig. 3.1-3.

^{119m}Sn in $CaSnO_3$ was used as a Mössbauer γ-ray source and the zero Doppler velocity was defined to be the center shift value of $BaSnO_3$ at room temperature. All CEMS spectra were analyzed by least-square-fitting assuming the thin foil approximation.

In the case of the ^{119}Sn implantation into Fe, ^{57}Fe CEMS measurements were also performed in order to investigate the microscopic state of the target Fe atoms implanted by ^{119}Sn. These ^{57}Fe CEMS spectra were compared with corresponding ^{119}Sn spectra and the influence of ^{119}Sn implantation on the target Fe atoms was discussed. The method of ^{57}Fe CEMS measurements is same as that of ^{119}Sn CEMS, but 25 mCi ^{57}Co in Rh was used for Mössbauer γ-ray source and the Doppler velocity scale was calibrated by using a spectrum of α-Fe at room temperature.

3) X-ray diffraction measurements

The surface structures of specimens were measured by X-ray diffraction and compared with the results from CEMS measurements. The diffractometer of Rigaku RAD-1A was used for these X-ray diffraction measurements.

4) Computer simulation of ^{119}Sn depth distribution using TRIM3D code

In order to discuss the depth distribution of implanted Sn atoms, ^{119}Sn CEMS spectra were compared with the results from TRIM3D computer simulation$^{6)}$. TRIM3D code has been developed for the calculation of the radiation damage by the energetic particles. The method of the calculation is constituted by the repetition of the history that one incident particle loses its energy by collisions with the target atoms. The particle is implanted into amorphous structured target to concern the random collision of the particle in the target. In TRIM3D code, it is assumed that the incident particle loses its energy by elastic collision to target atoms and by electronic excitation independently. When the energy of the particle becomes smaller than the cut-off value that is chosen about 5 eV or the particle goes out from the target, one cycle of the calculation is finished. After a set number of the repetition of this cycle, the radiation damage energy and the number of the stopped particles are calculated by the summation over the all cycles at various depth. TRIM3D computer simulation is widely used for the information of the radiation damage by energetic particles.

10000 cycles of particle histories were actually calculated for each simulation of the ^{119}Sn implantation. The values of 25 and 22 eV were used for the displacement threshold energy of metallic Ni and Fe$^{7)}$. The cut-off energy was chosen to 5 eV in all simulations. The depth distributions of implanted ^{119}Sn atoms were presented by the number of Sn atoms stopped at each depth from surface having a 5 nm layered intervals. The local

Sn concentrations were also calculated on the assumption that all implanted Sn atoms occupied the substitutional lattice sites of the targets.

5) Mössbauer measurements of Ni-Sn and Fe-Sn alloys

In order to compare with the CEMS spectra of ^{119}Sn implanted Ni and Fe, the transmission Mössbauer measurements were performed for the Ni-Sn and Fe-Sn alloys.

Figure 3.1-4 shows the phase diagram of Ni-Sn system$^{8)}$. The maximum solid solubility of Sn into Fe is about 10.4 at.% at 1403 K and the intermetallic compounds are formed at 25, 40 and 57.1 at.% Sn. Ni-0.9, 3.2, 5.1, 6.9, 8.6 and 10.4 at.% Sn solid solutions, Ni_3Sn and Ni_3Sn_2 intermetallic compounds were prepared from melts. The ingots from these compositions were melted by the arc furnace and annealed for 100 hrs at several temperatures in the silica tube under vacuum. After annealing, the powder specimens were made of these ingots and annealed for 12 hrs in the evacuated silica tube. For the solid solution treatment, the powder specimens were quenched into iced water and the other specimens for intermetallic compounds were cooled in air. The structures of these powders were checked by X-ray diffraction measurements.

The phase diagrams of Fe-Sn system$^{8)}$ is shown in Fig. 3.1-5. By using a similar process to the preparation of Ni-Sn alloy specimens, Fe-1.2, 3.5, 4.8, 5.9 and 8.2 at.% Sn solid solutions and FeSn intermetallic compounds were prepared from melts.

Transmission Mössbauer measurements were performed by the combination of a velocity transducer and a multichannel analyzer

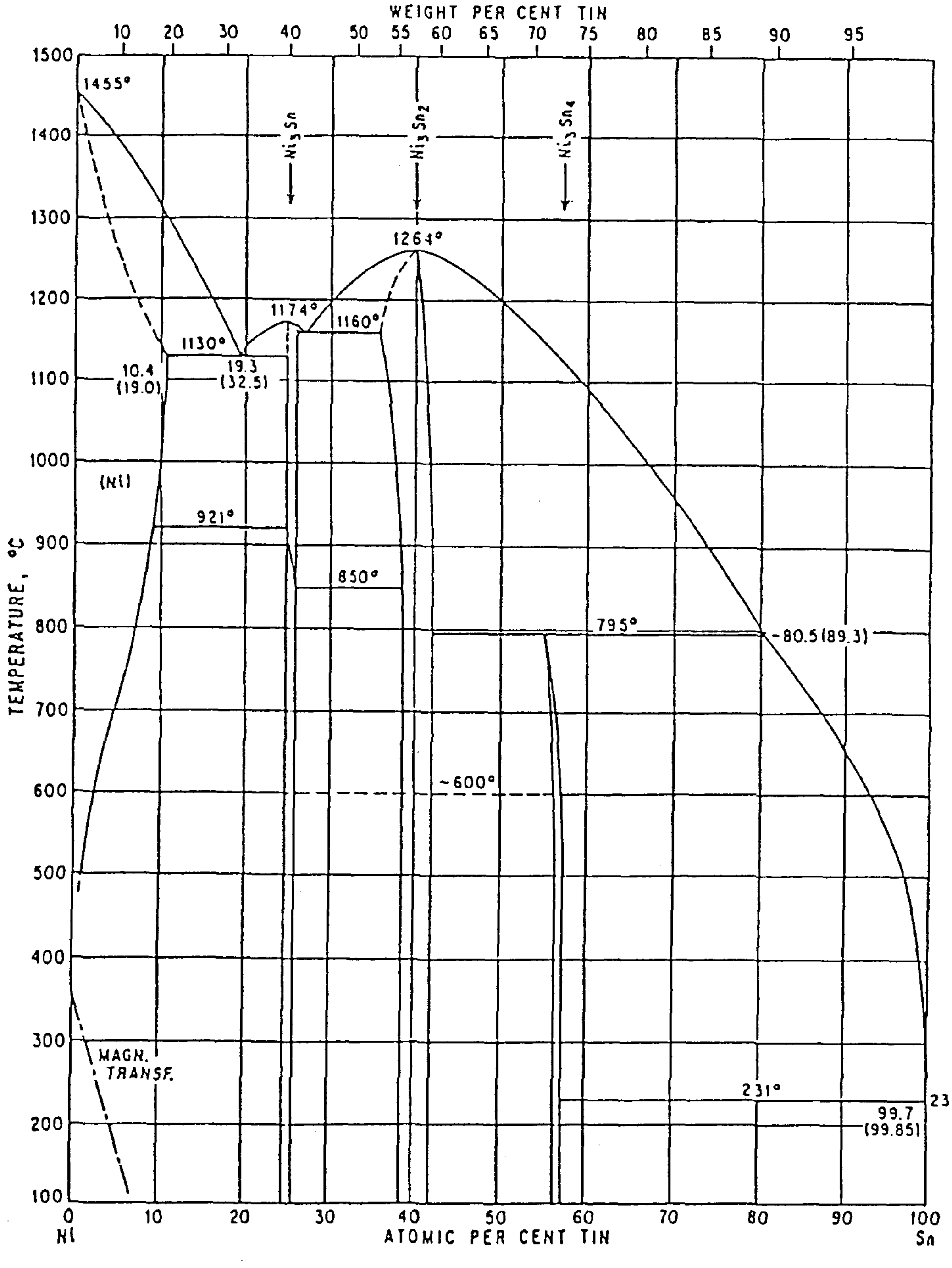

Fig. 3.1-4. Phase diagram of Ni-Sn alloy system8).

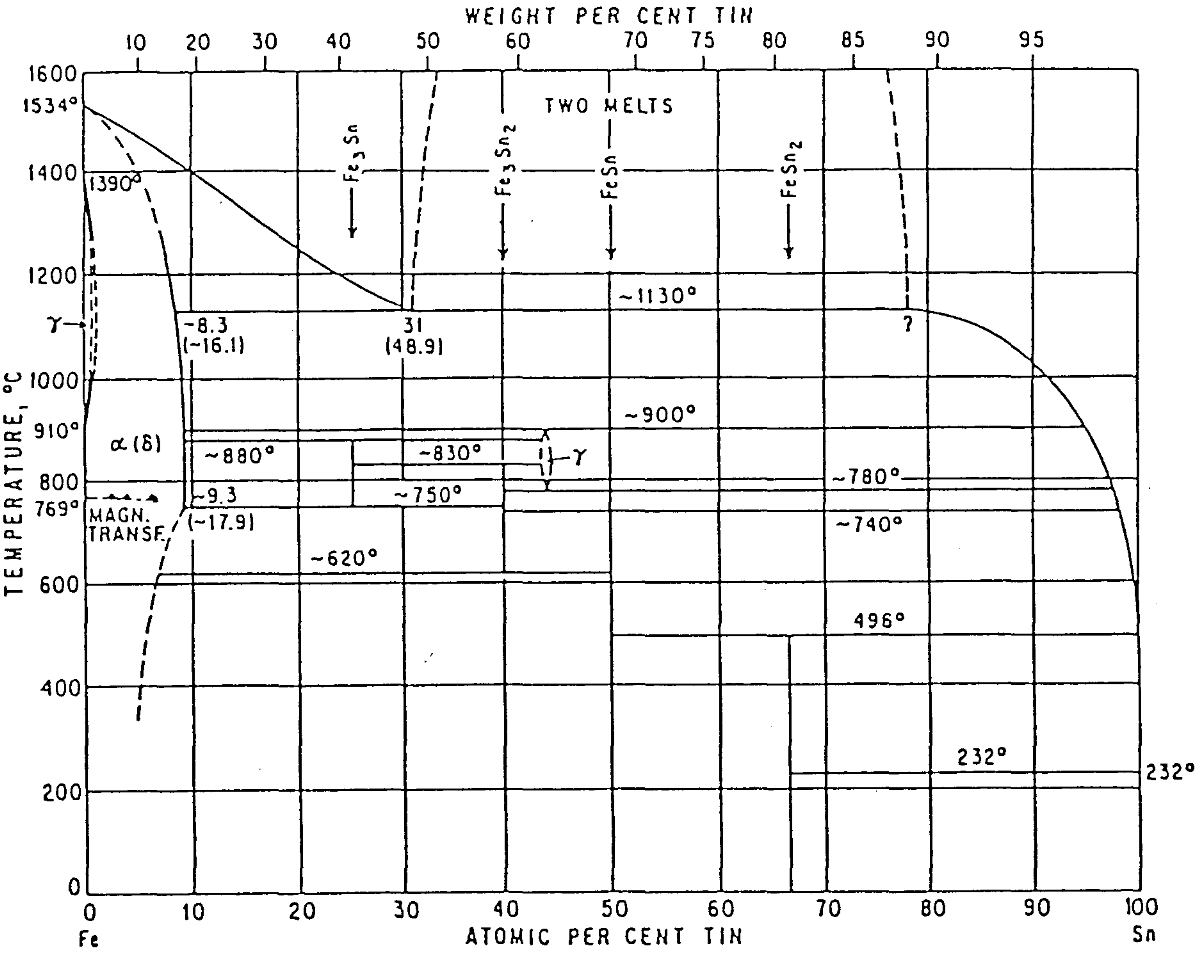

Fig. 3.1-5. Phase diagram of Fe-Sn alloy system[8)].

operated in time mode. ^{119m}Sn in $CaSnO_3$ was used for the γ-ray source and 0 mm/s in the velocity scale was relative to the center shift value of $BaSnO_3$ at room temperature. The spectra were fitted by the least-square-fit procedure assuming the thin foil approximation.

In the case of Fe-Sn alloys, ^{57}Fe Mössbauer measurement was also carried out. ^{57}Co in Rh was used for the γ-ray source and the velocity scale was calibrated by the metallic iron at room temperature.

6) Analysis of hyperfine field distribution

For the information to the magnetic property of the implanted ^{119}Sn and target atoms, the hyperfine field distribution was determined using the continuous distribution function which is given by the Fourier series expansion. The Mössbauer spectrum showing a broad distribution of the hyperfine field was decomposed into the power spectrum by the Fourier series and the probability at each hyperfine field was calculated from the coefficients of Fourier expansion.

3.1.3 Results and Discussion

1) ^{119}Sn implanted into Ni

a. Ni-Sn alloys

Figure 3.1-6 shows the ^{119}Sn TMS spectra of Ni-Sn solid solutions measured at room temperature. The spectra of the Sn concentrations below 6.9 at.% seem to be constructed by one doublet peak. These doublet-like-peaks are magnetically-split

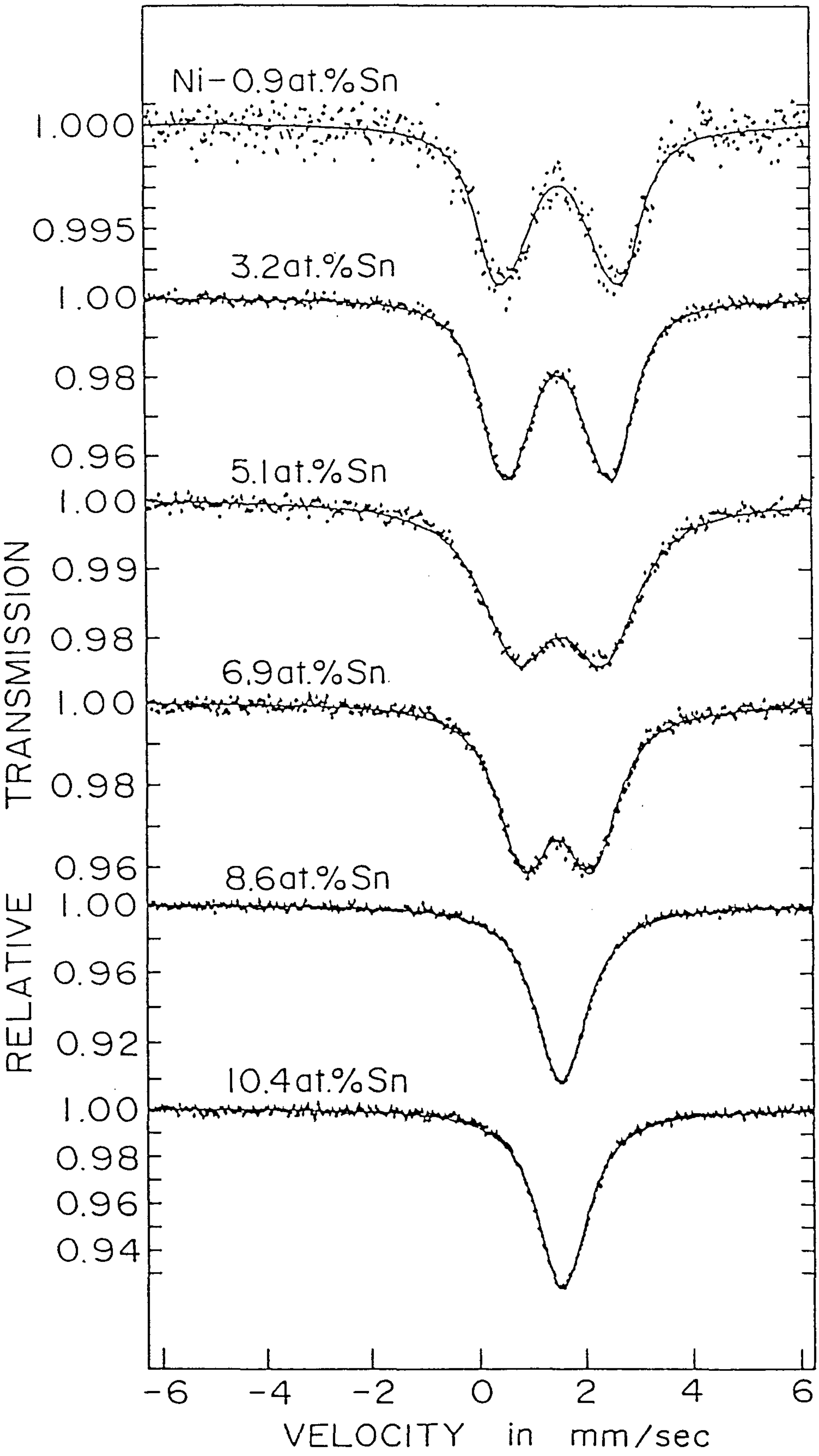

Fig. 3.1-6. ^{119}Sn TMS spectra of Ni-Sn solid solutions measured at room temperature. Velocity scale is relative to $BaSnO_3$ at room temperature.

6-line patterns whose subpeaks are well overlapped because of the small splitting by the hyperfine field compared with the natural line width of the ^{119}Sn spectrum. The spectrum of the Sn concentration below 8.6 at.% is analyzed by one 6-line pattern and the spectrum of 10.4 at.% Sn is analyzed by one singlet peak.

The values of the isomer shift are ranged from +1.50 mm/s to +1.54 mm/s and these are hardly changed by the Sn concentration. The magnitude of the hyperfine field decreases from 19.6 kG with an increase of the Sn concentration and fell in zero when the Sn concentration exceeds 10 at.%. This result coincides with the fact that Curie temperature of Ni-Sn solid solution falls with an increase of Sn concentration and the critical concentration where Curie temperature equals room temperature must be around 10 at.% 9).

The isomer shift values of these peaks are well agreed with those of the substitutional Sn atoms reported previously and the magnitude of hyperfine field of 19.6 kG at the Sn concentration of 0.9 at.% is also agreed with that of the Sn dissolved into Ni matrix10,11).

At the Sn concentration of 5.1 at.%, the full width at half maximum of the peak is 1.42 mm/s and this is much larger than the line width observed from β-Sn foil, 0.83 mm/s. This fact might suggest that the existence of another extra-component in the spectrum. But the further analysis of the spectrum using an additional component has not been successful because of the no improvement in chi-square value.

The TMS spectra of Ni_3Sn and Ni_3Sn_2 intermetallic compounds are shown in Fig. 3.1-7. The spectrum of Ni_3Sn is quite similar

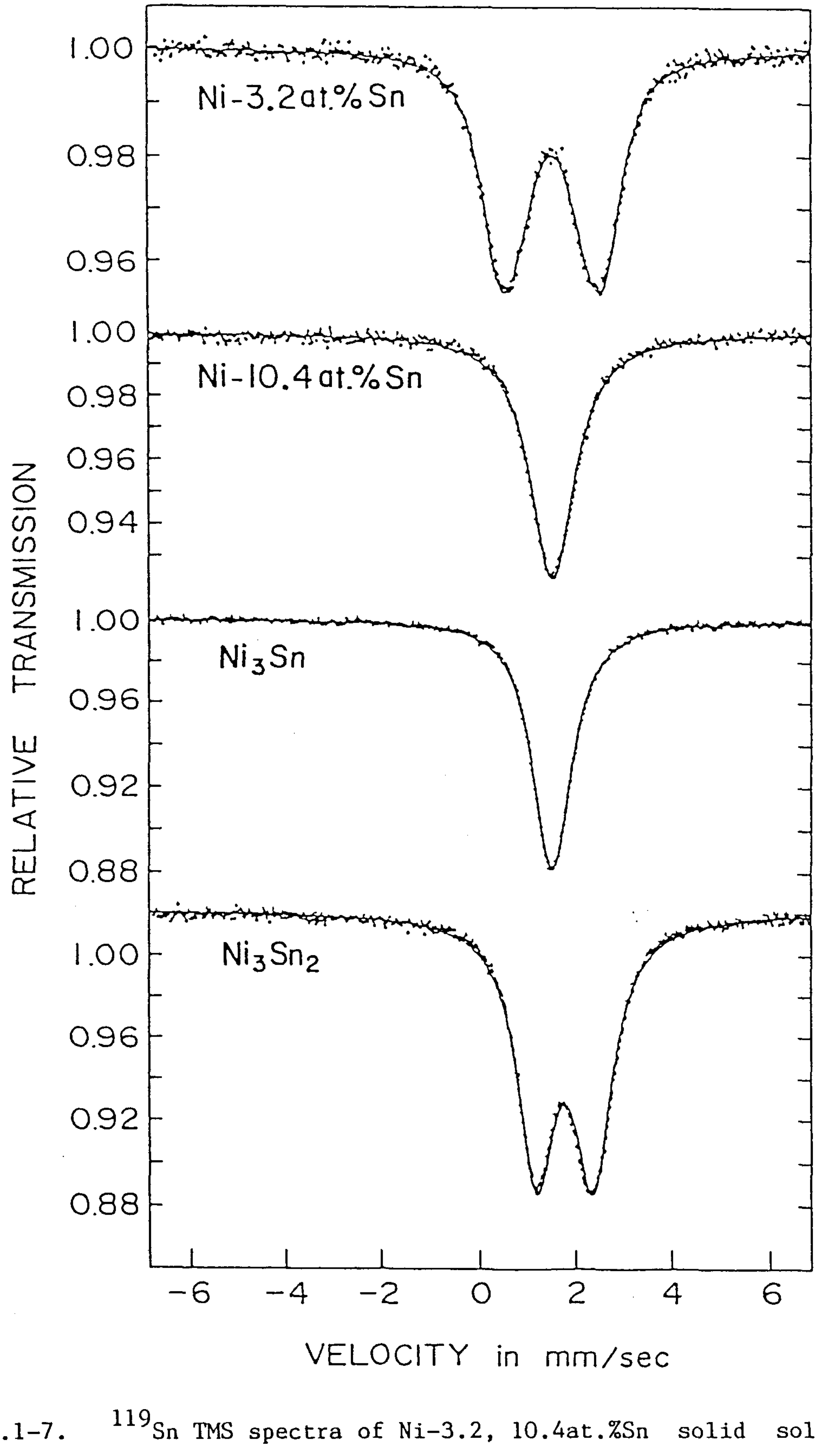

Fig. 3.1-7. ^{119}Sn TMS spectra of Ni-3.2, 10.4at.%Sn solid solutions, Ni_3Sn and Ni_3Sn_2 intermetallic compounds measured at room temperature. Velocity scale is relative to $BaSnO_3$ at room temperature.

to the spectrum of Ni-10.4at.%Sn solid solution and these two phase cannot be distinguished by Mössbauer spectra. The structure of Ni_3Sn is Mg_3Cd (DO_{19}) type so that X-ray diffraction measurement is a good method to distinguish these two phases[12).

b. ^{119}Sn CEMS spectra

^{119}Sn CEMS spectra measured for the specimens implanted by ^{119}Sn with the dose of $5x10^{16}$ ions/cm^2 are shown in Fig. 3.1-8. Each spectrum obviously consists of some components, but, widely split peaks which are attributed to the vacancy associated Sn atoms observed in source experiments[13,14) reported previously is not found in the observed spectra.

These spectra can be analyzed using two components. One is a ferromagnetic component (6-line pattern) and the other is a paramagnetic component (singlet peak). In this analysis, the amount of the ferromagnetic component increases with the increase of the accelerating energy. The value of isomer shift is around +1.51 mm/s for all peaks and this value is in good agreement with that of substitutional Sn in Ni[13,14), which is shown in Fig. 3.1-6. The magnitude of the hyperfine field is ranged from 13.8 kG to 14.5 kG and increases with the increase of the accelerating energy. So that, the ferromagnetic component in Fig. 3.1-8 is due to substitutional Sn in Ni-Sn solid solution where local Sn concentration is less than 10 at.%. The isomer shift values and the magnitude of hyperfine field suggest that the implanted Sn atoms are substitutional impurities in Ni-Sn solid solution. It is rather difficult to determine whether the paramagnetic component arises from substitutional Sn in Ni-Sn

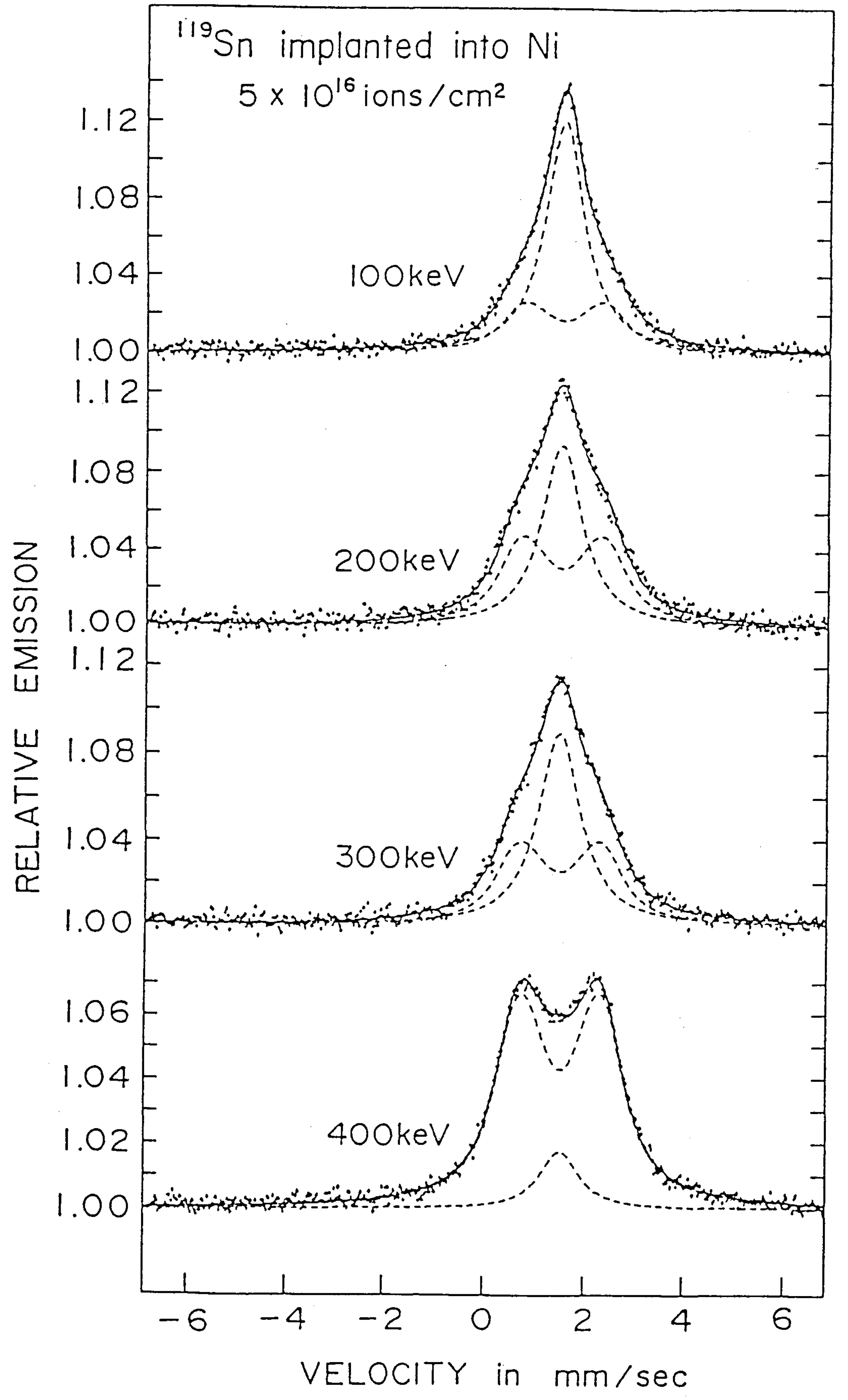

Fig. 3.1-8. ^{119}Sn CEMS spectra of ^{119}Sn implanted into Ni. Both of the implantations and the CEMS measurements were performed at room temperature. All spectra are well analyzed by the superposition of one singlet peak and one 6-line pattern like a doublet peak, which are shown by the broken lines in the spectra. Velocity scale is relative to $BaSnO_3$ at room temperature.

solid solution, of which Sn concentration is more than 10 at.%, or Sn in Ni_3Sn intermetallic compound, because these Mössbauer spectra show the nearly identical hyperfine interaction parameters and cannot be distinguished to each other. X-ray diffraction measurements for the specimens implanted with the accelerating energy of 100 and 200 keV in Fig. 3.1-9 clearly show the peaks of Ni_3Sn intermetallic compound[15)], so that a large part of the paramagnetic component must be due to Sn in Ni_3Sn intermetallic compound.

c. TRIM3D computer simulation

TRIM3D computer simulation is applied to the case of Sn implantation into Ni and the obtained results are shown in Fig. 3.1-10. The vertical scale at the left hand side indicates the depth distribution of Sn implanted into Ni and the right hand side scale the local Sn concentration. The hatched area, where local Sn concentration is lower than 10 at.%, increases with the increase of the accelerating energy. The contribution of the hatched area to whole histogram depends on the energy of ions. The dependence of the hatched area on the acceleration energy is similar to that of the area contribution of the ferromagnetic component in Fig. 3.1-8. The ratio of hatched area to the whole histogram in Fig. 3.1-10 is in good agreement with the ratio of 6-line area to the whole spectrum in Fig. 3.1-8.

X-ray diffraction patterns indicated that Ni_3Sn intermetallic compound must exist at around the depth of the non-hatched area in Fig. 3.1-8. However, Sn concentrations of non-hatched area are much less than 25 at.%, that is the composition of

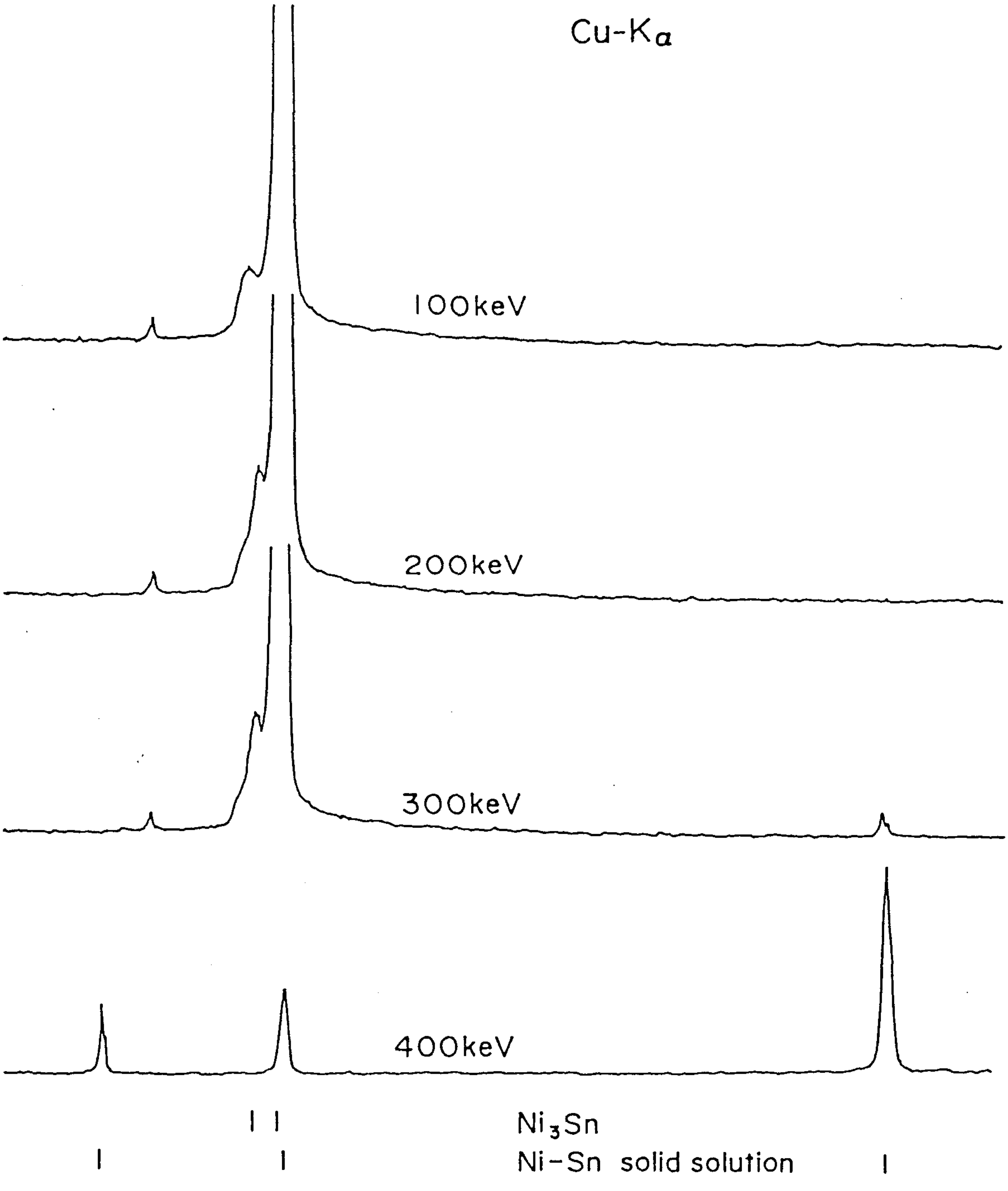

Fig. 3.1-9. Cu-K_α X-ray diffraction patterns obtained from the ^{119}Sn implanted Ni foils with the dose of 5x10^{16} ions/cm^2. The bars above the angular scale indicate the peak positions of Ni_3Sn[15] and Ni-Sn solid solution.

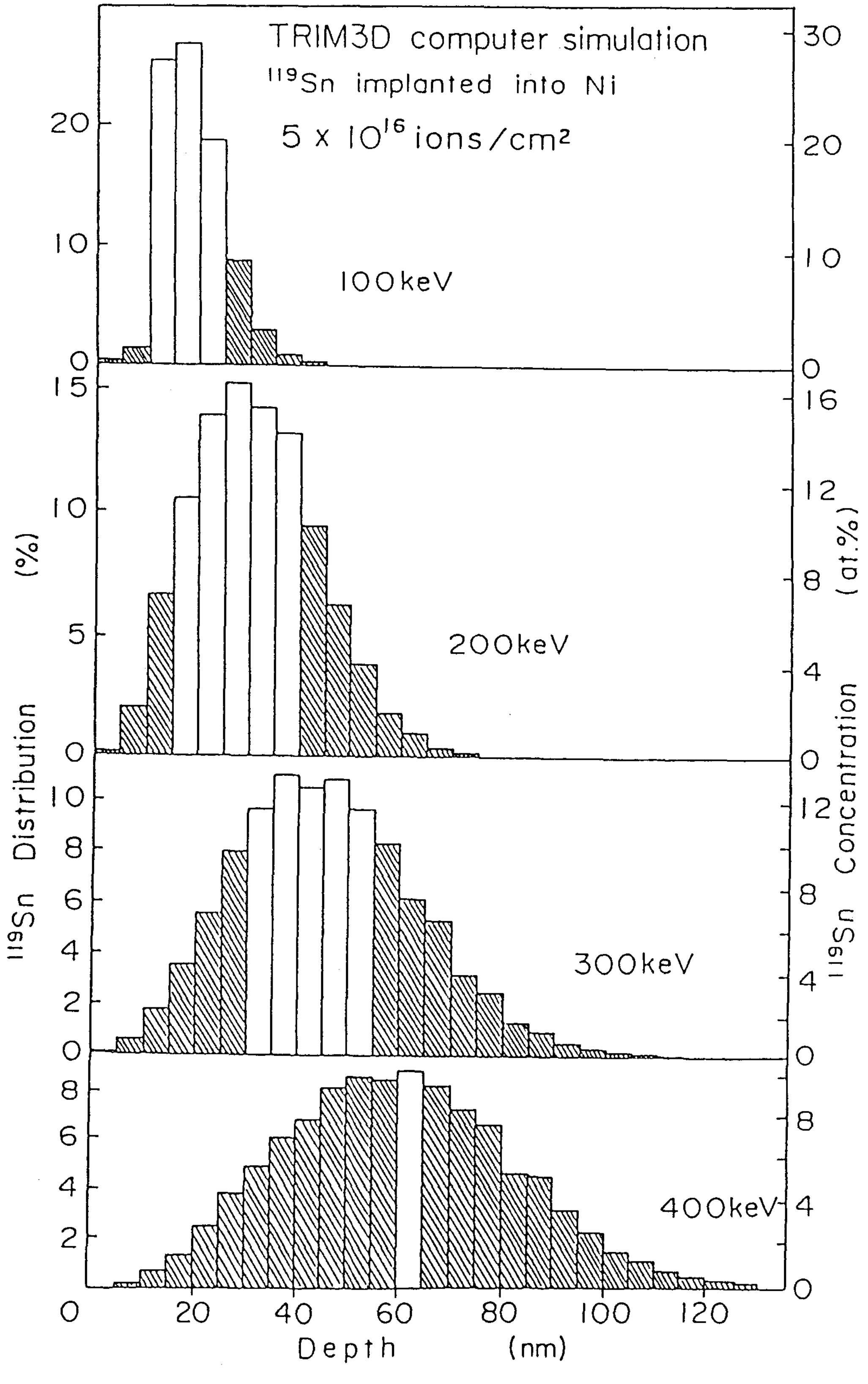

Fig. 3.1-10. ^{119}Sn depth distribution of ^{119}Sn implanted into Ni calculated by using TRIM3D code. The scale of the right hand side indicates the local Sn concentration evaluated by assuming that implanted ^{119}Sn atoms occupy the substitutional sites of Ni matrix. The hatched areas are where the local Sn concentration is lower than 10 at.%.

Ni_3Sn, except for the case of 100 keV.

This conflict can be explained by assuming that the local diffusion of Sn atoms occurs during the implantation in the area where Sn concentration is larger than 10 at.%. The diffusion may be the radiation assisted one, since the normal substitutional impurity diffusion cannot appreciably take place blow 320 K which is the measured highest temperature of the specimen during the ion bombardment. At 320 K, a vacancy in Ni is expected to jump only 10^{-10} times a second by the calculation using the value of migration energy, 1.5 eV16).

In the above analysis, each CEMS spectrum is decomposed into two components. The analysis by the decomposition into several kinds of 6-lines for the ferromagnetic component gives similar chi-square values to those obtained by two components analysis. The random collisions of the implanted particle with the target atoms give rise to the depth and the concentration distribution of the implanted particles, which is shown in the TRIM3D computer simulation as shown in Fig. 3.1-10. This leads to the idea that hyperfine field of the ferromagnetic component in Fig. 3.1-8 must have a distribution.

The satisfactory analysis of CEMS spectra using only two components as mentioned above can be understood by that the hyperfine field distribution of the Sn atoms implanted into Ni is considerably narrow as compared with the natural line width of Sn nucleus.

One could reproduce the observed CEMS spectrum by using the concentration distribution calculated by TRIM3D code, as in Fig. 3.1-10, combined with the Mössbauer parameters obtained from the measurement on various Ni-Sn alloys. Nevertheless, as a simplest way of analysis, the ferromagnetic component in the CEMS spectrum at the bottom of Fig. 3.1-8 (with accelerating energy, 400 keV) is decomposed into four subcomponents. The result well agrees with that of TRIM3D calculation except the subcomponent corresponding to the low Sn concentration around 4 at.% which has a larger area ratio than that by TRIM3D calculation. This discrepancy could arise from the secondary effect such as the diffusion of Sn atoms after implantation, which TRIM3D computer simulation does not take into account. This effect becomes important in the case of high doses such as $5\text{x}10^{16}$ ions/cm^2.

The dose dependence of CEMS spectra is also observed. In the case of the dose of $1\text{x}10^{16}$ ions/cm^2, CEMS spectra in Fig. 3.1-11 consist of only ferromagnetic components. These spectra reflect the result of TRIM3D computer simulation which shows maximum local Sn concentration is about 6 at.% leading to the formation of ferromagnetic Ni-Sn solid solution. The magnitudes of hyperfine field are larger than those at the dose of $5\text{x}10^{16}$ ions/cm^2 because of the low Sn concentration. The magnitude of the hyperfine field is related to the mean value of local Sn concentration. At the lowest dose of $5\text{x}10^{15}$ ions/cm^2, each CEMS spectrum shows the larger hyperfine split 6-line pattern because of the lower Sn concentration. Thus, the dependence of CEMS spectra on the decrease of the dose is well explained by the reduction of local Sn concentration.

The vacancy-associated lines reported in the source experiments are not observed in any CEMS spectra. The dose of the

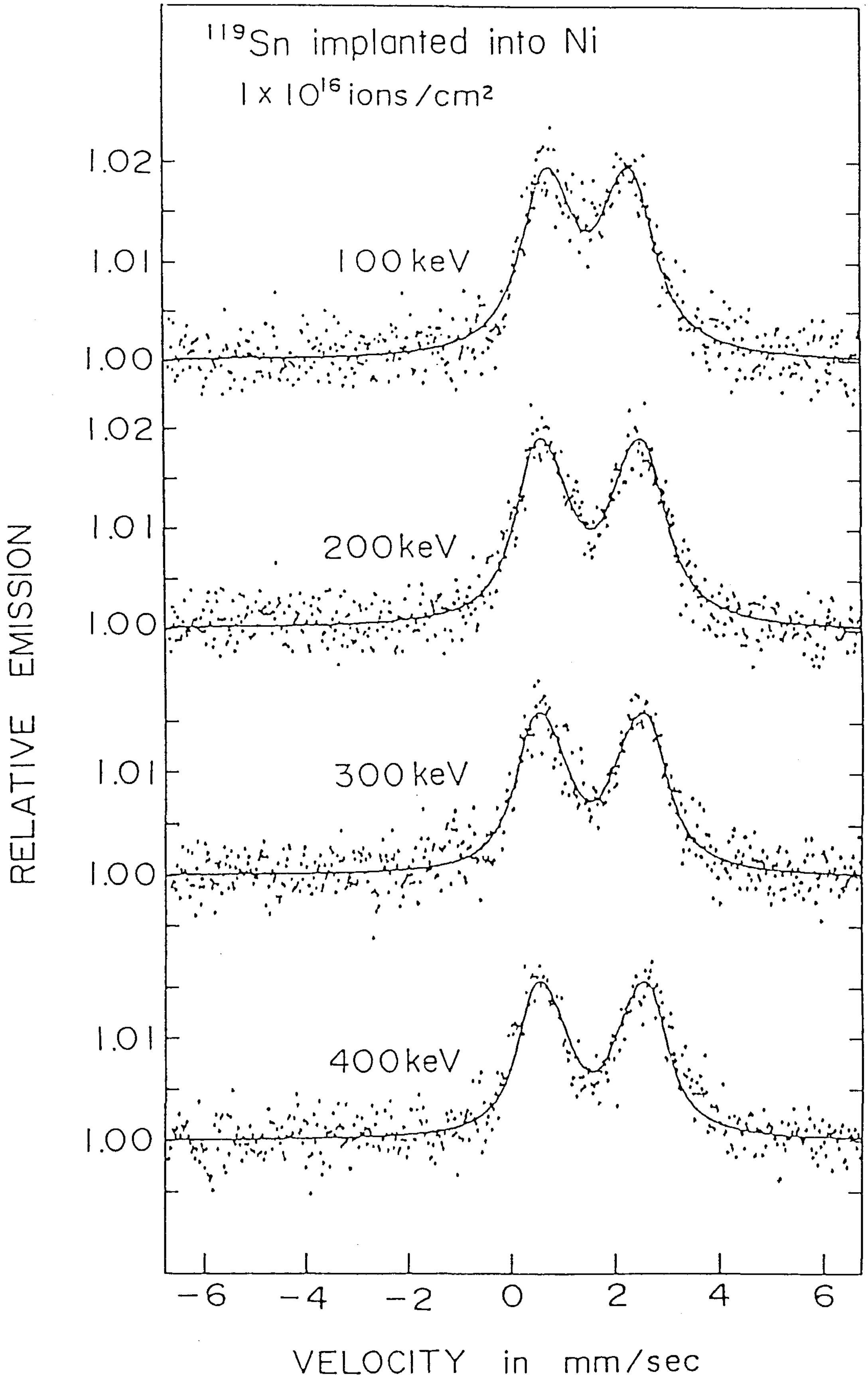

Fig. 3.1-11. ^{119}Sn CEMS spectra of ^{119}Sn implanted into Ni. Both of the ^{119}Sn implantations and the ^{119}Sn CEMS measurements were performed at room temperature. Velocity scale is relative to $BaSnO_3$ at room temperature.

source experiments in ref. 14 is 5×10^{13} ions/cm^2. That is much smaller than the least dose of 5×10^{15} ions/cm^2 in this study. At the dose of 5×10^{15} ions/cm^2, the local Sn concentrations are more than 1 at.%. The conditions in the target of this study are quite different from those of the source experiment so that defect associated lines could not be observed in this study.

2) ^{119}Sn implanted into Fe

a. Fe-Sn alloys

Figure 3.1-12 shows ^{119}Sn TMS spectra of Fe-Sn solid solutions whose Sn concentrations are 1.2, 3.5, 4.8, 5.9 and 8.2 at.%. The spectrum of Fe-1.2at.%Sn solid solution consists of only one 6-line pattern. This component is due to the Sn atom dissolved into Fe matrix, since the value of the isomer shift of +1.54 mm/s and the magnitude of hyperfine field of 85 kG are agreed with the values for isolated Sn in bcc Fe[11,17,18,19].

At higher concentrations of 3.5 and 4.8 at.%Sn, the spectra are decomposed into two kinds of 6-line patterns having the same line width. This analysis is well agreed with the results from the hyperfine distributions analysis in which the distributions have two peaks at the hyperfine field of about 60 and 85 kG as shown in Fig. 3.1-13. The values of the isomer shift and hyperfine field obtained from the larger split 6-line pattern are +1.53 and +1.57 mm/s and 81 and 85 kG respectively. These values well agree with those of the Sn atom dissolved into Fe.

The values of the isomer shift and hyperfine field for the smaller split 6-line pattern are 1.43 and 1.51 mm/s and 63 and 64

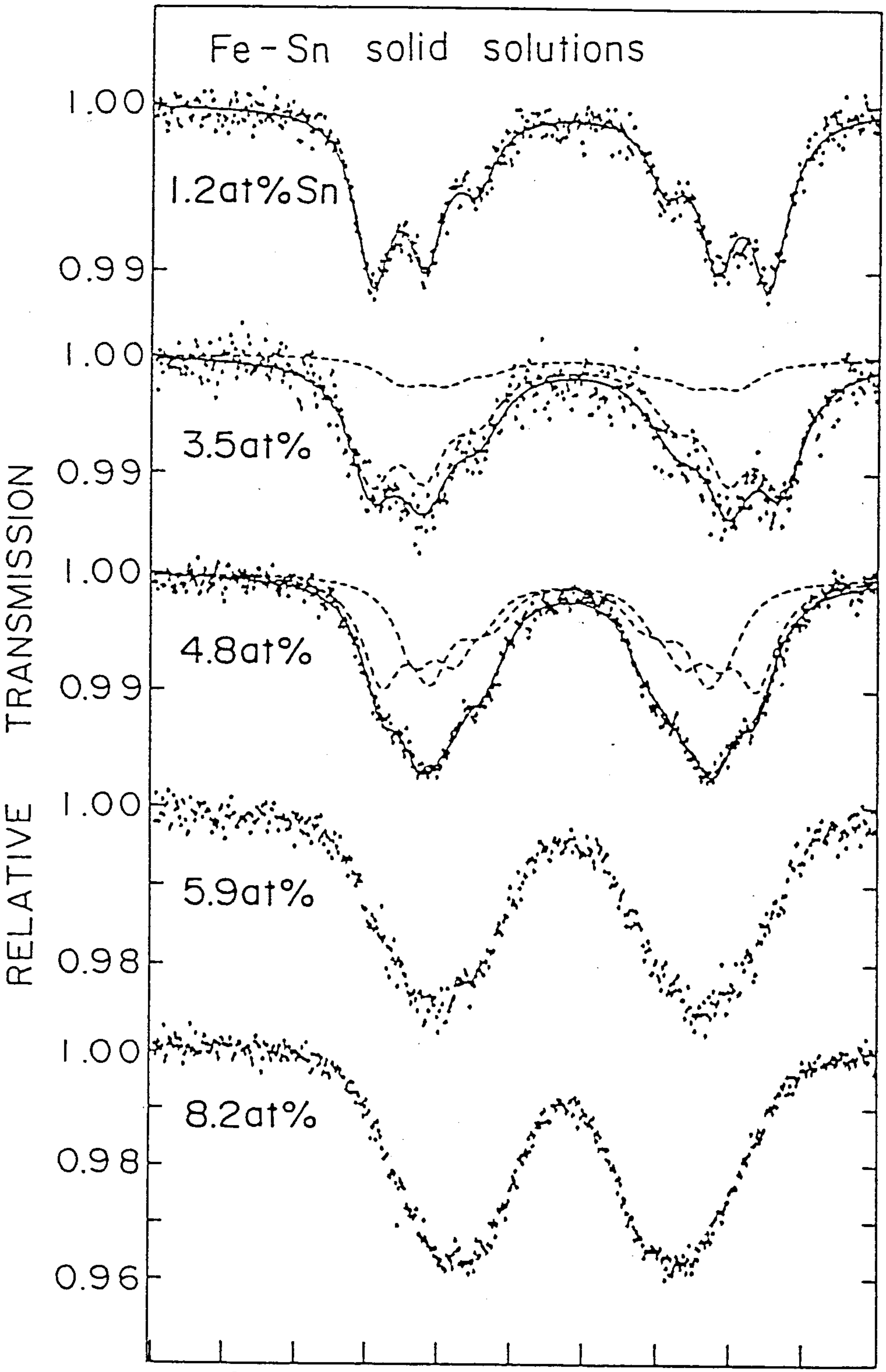

Fig. 3.1-12. ^{119}Sn TMS spectra of Fe-Sn solid solutions measured at room temperature. At the Sn concentrations of 1.2, 3.5 and 4.8 at.%, the spectra are well reproduced by the two kinds of 6-line patterns as shown by broken lines in the spectra. Velocity scale is relative to $BaSnO_3$ at room temperature.

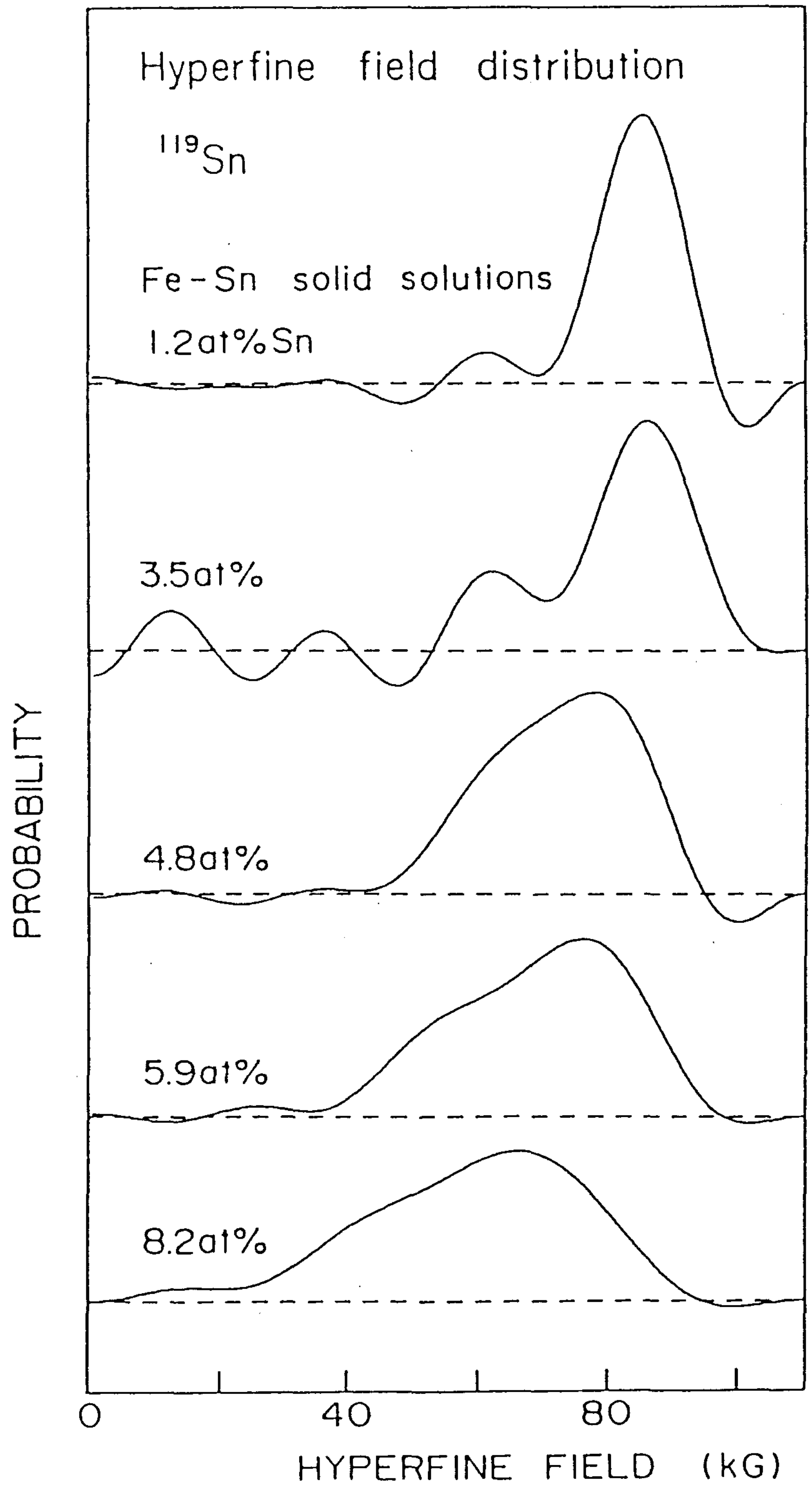

Fig. 3.1-13. Hyperfine field distributions obtained from the ^{119}Sn TMS spectra of Fe-Sn solid solutions shown in Fig. 3.1-12.

kG. The isomer shift values are almost same to those of larger split peaks. The hyperfine fields are smaller than those of the larger split 6-line pattern by about 20 kG. These values are close to 1.44 mm/s and 60 kG, evaluated for the Sn atom having one Sn atom at the first neighbor sites by ^{119}Sn TMS measurements of Fe-Sn solid solutions$^{19)}$.

The probability to find a Sn atom having n Sn atoms at the first and second neighbor lattice sites in bcc lattice is calculated by the following equation.

$$P(n)={}_{14}C_n(1-x)^{(1-n)}x^n$$

where x is atomic ratio of Sn atom in the Fe-Sn solid solution. The calculated values of P(n) and the areal contributions of each component in TMS spectra of Fe-1.2, 3.5 and 4.8 at.% Sn solid solutions are listed in Table 3.1-1. The values of P(0) well agree with the areal contributions of the larger split 6-line pattern to whole area at the Sn concentrations of 1.2, 3.5 and 4.8 at.%. So that the larger split 6-line patterns are due to the Sn atoms having no Sn atoms at the first and the second neighbor lattice sites and the smaller split peaks are due to the Sn atoms having more than one Sn atom at those sites.

At the Sn concentration higher than 5.9 at.%, the hyperfine field distributions become to be wide from low field up to high field continuously and show no clear peaks in spectrum. At the Sn concentration above 7 at.%, all of the Sn atoms in Fe-Sn solid solutions have at least one Sn atom at the first and the second neighbor lattice sites. In such case, the magnetic state of the Fe-Sn solid solution will wholly differ from that of the dilute Fe-Sn solid solutions, whose TMS spectra can be explained

Table 3.1-1. The areal contributions of the larger split 6-line pattern (a) and the smaller split 6-line pattern (b) in the spectra of Fig. 3.2-12 and the calculated values of P(n), the probability to find a Sn atom having n Sn atoms at the first and second neighbor lattice sites.

Sn Concent.(%)	6-line(a)	6-line(b)	P(0)	P(1)	P(2)
1.2	1.00	-	0.844	0.144	0.011
3.5	0.74	0.26	0.607	0.308	0.073
4.8	0.51	0.49	0.502	0.355	0.116

by the local Sn configuration.

Figure 3.1-14 shows the ^{119}Sn and ^{57}Fe TMS spectra of the FeSn intermetallic compound measured at room temperature. Both TMS spectra are well analyzed by the superposition of the two 6-line patterns. ^{57}Fe Mössbauer parameters obtained are agreed with the values previously reported$^{20)}$. In the case of the ^{119}Sn Mössbauer measurement, the Mössbauer parameters quite different from those in ref. 20.

b. ^{119}Sn CEMS spectra

Figure 3.1-15 shows ^{119}Sn CEMS spectra of ^{119}Sn implanted into Fe at the acceleration energy of 100, 200, 300 and 400 keV and the dose of 5x10^{16} ions/cm^2. The strong peaks corresponding to bcc structure were observed in the X-ray diffraction patterns of these specimens (Fig. 3.1-16). The quite weak peak by Cu-K_α radiation was observed at 43.61° in the diffraction pattern obtained from the specimen with the acceleration energy of 100 keV and at 44.27° in that of 300 keV, respectively. The intensity of these peaks was so small that the origin of these peaks could not be defined only by the X-ray diffraction measurement.

At the energy of 400 keV, the CEMS spectrum is symmetrical for the centroid of the peaks and similar to those of the dilute Fe-Sn solid solutions. The spectrum is well reproduced by the two 6-line patterns having different hyperfine fields. The line widths of two components were restricted in the same value. Hyperfine field distributions shown in Fig. 3.1-17 make it sure that this spectrum is composed of two kinds of the ferromagnetic components, whose hyperfine field values are about 60 kG and 82

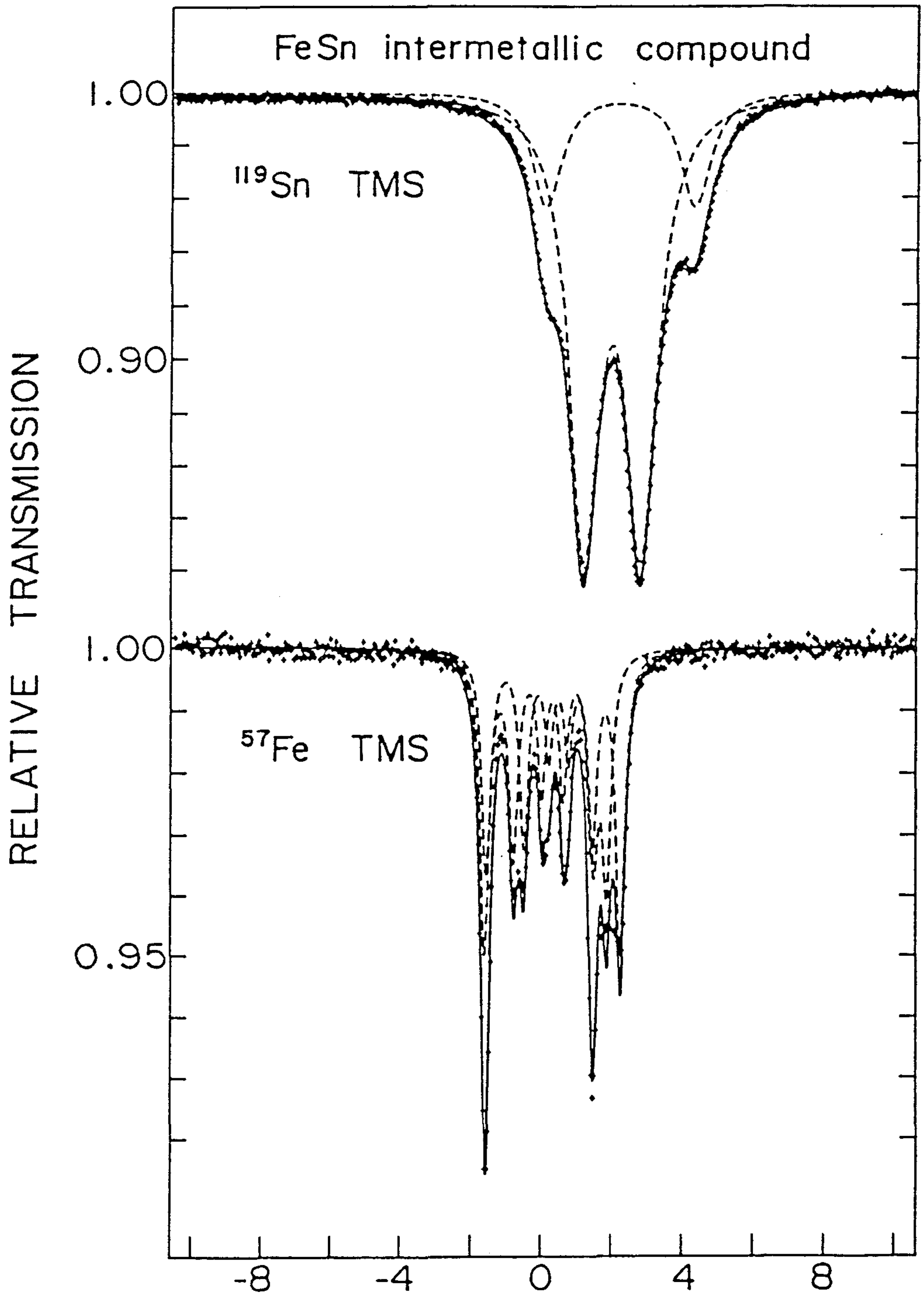

Fig. 3.1-14. ^{119}Sn and ^{57}Fe TMS spectra of FeSn intermetallic compound measured at room temperature. In both cases, the spectra are well analyzed by the two kinds of 6-line patterns, as shown by broken lines in the spectra. The velocity scale is relative to α-Fe at room temperature and 0 mm/s of ^{119}Sn TMS is determined by $BaSnO_3$ at room temperature.

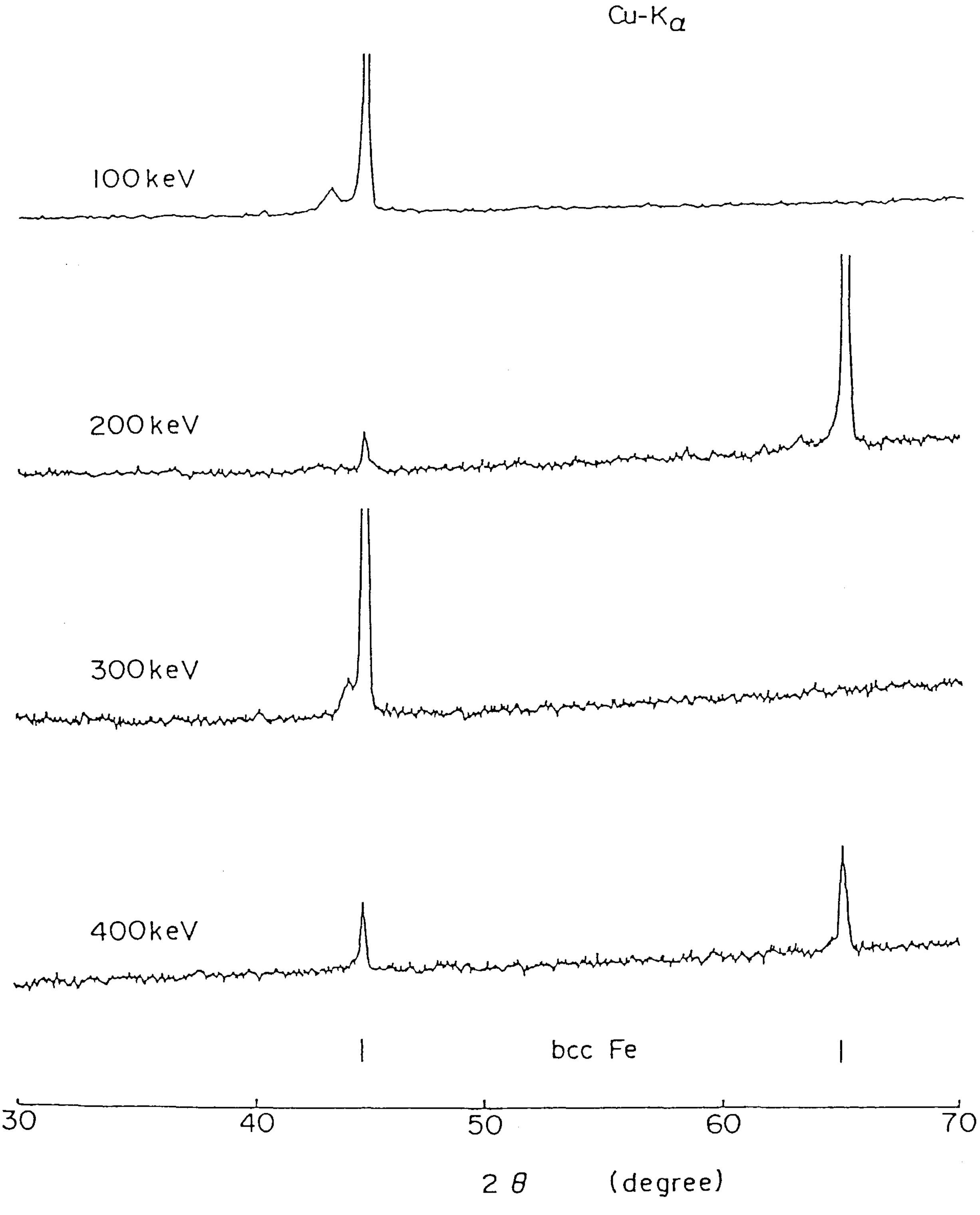

Fig. 3.1-15. Cu-K$_\alpha$ X-ray diffraction patterns obtained from the ^{119}Sn implanted Fe foils with the dose of 5x10^{16} ions/cm^2.

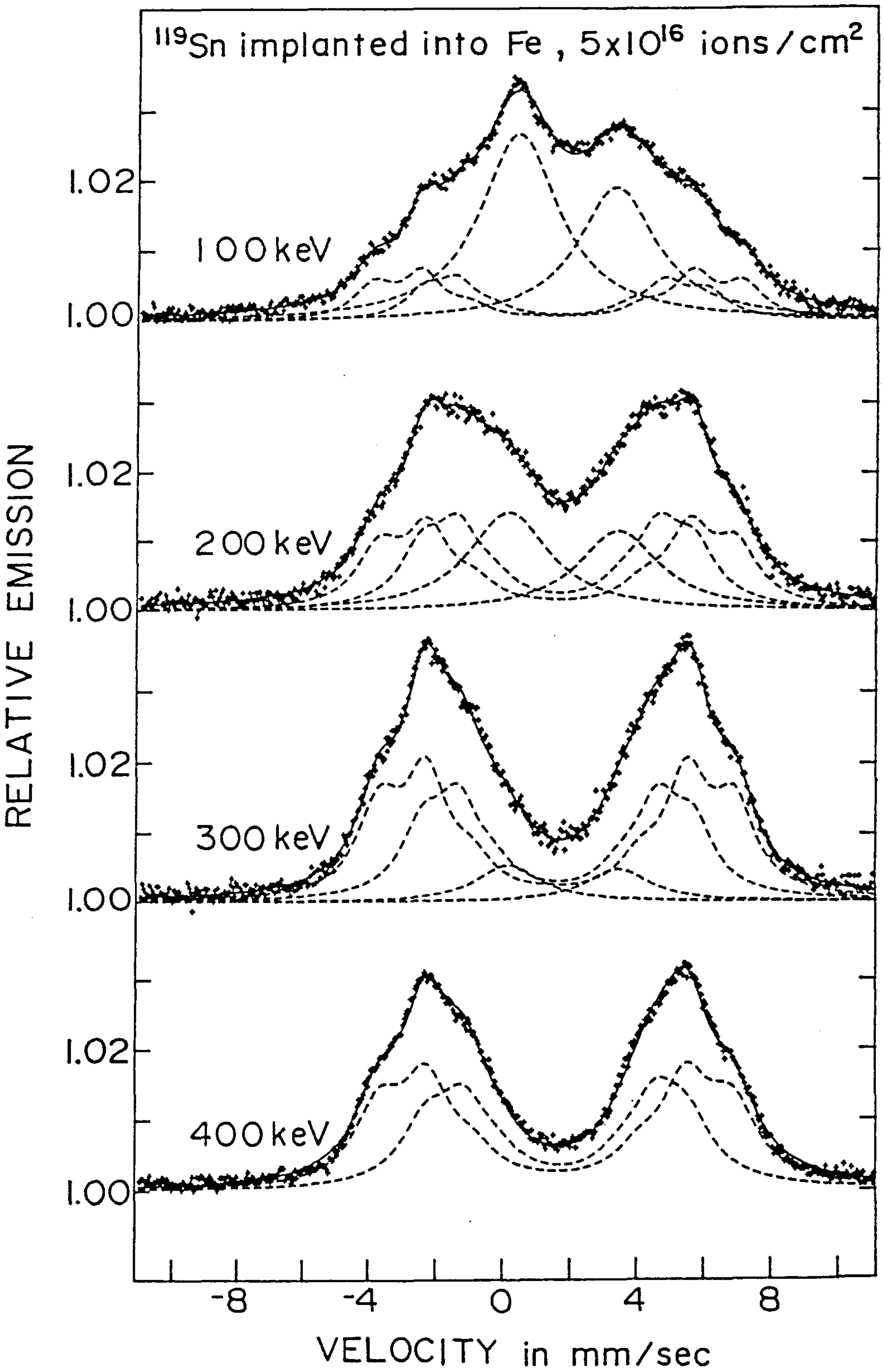

Fig. 3.1-16. ^{119}Sn CEMS spectra of ^{119}Sn implanted into Fe. Both of the ^{119}Sn implantations and ^{119}Sn CEMS measurements were performed at room temperature. Two singlet and two 6-line patterns are shown by broken lines in the spectra, except for the bottom spectrum which is decomposed by two 6-line patterns. Velocity scale is relative to $BaSnO_3$ at room temperature.

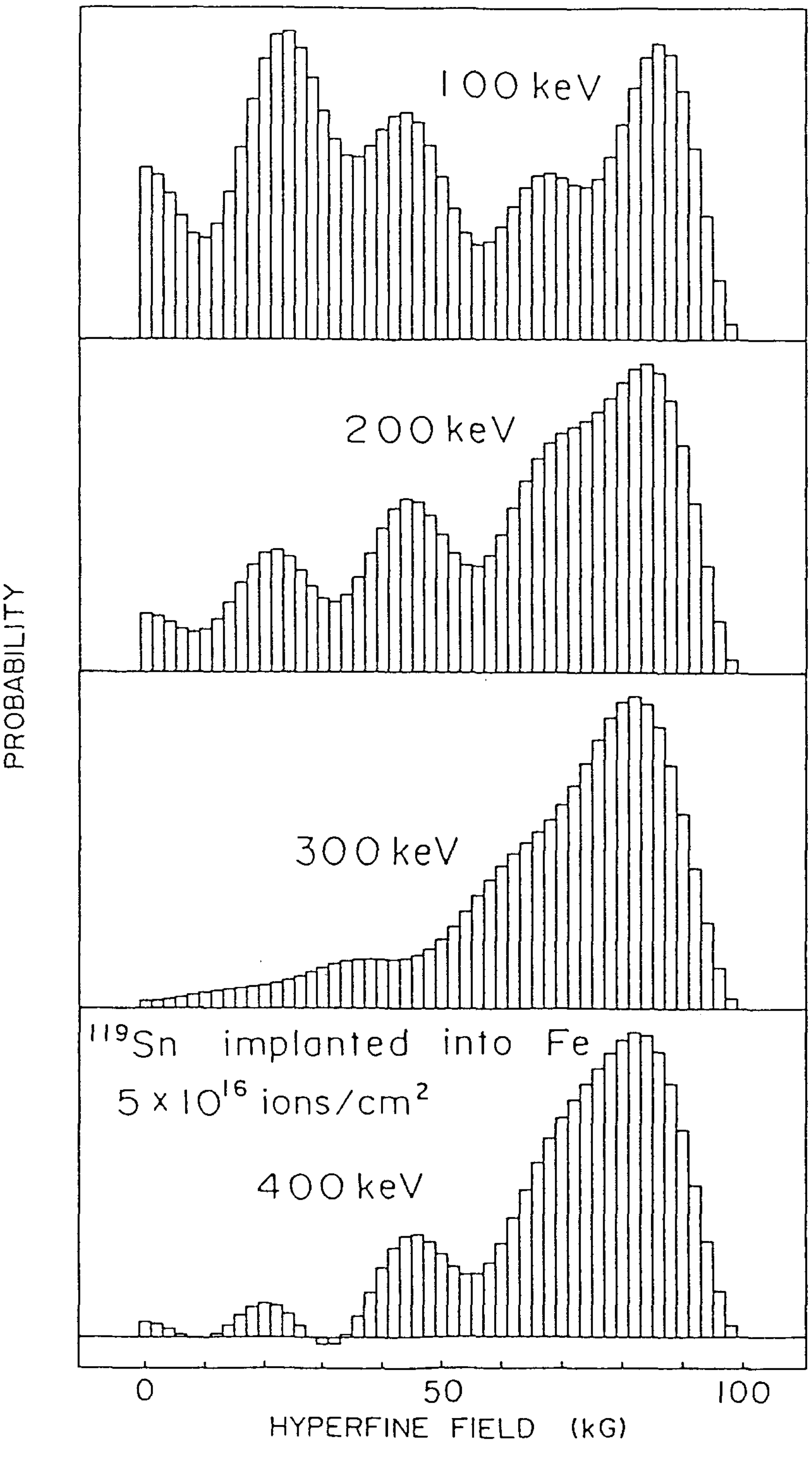

Fig. 3.1-17. Hyperfine field distributions obtained from the ^{119}Sn CEMS spectra of ^{119}Sn implanted into Fe shown in Fig. 3.1-14.

kG, respectively.

The isomer shift and hyperfine field values of the larger split components are +1.54 mm/s and 82 kG, respectively. These values are well agreed with those for the substitutional Sn atoms in Fe obtained from the source experiments$^{21,22)}$. These values are also similar to those of the substitutional Sn atoms having no Sn atoms at the first and the second neighbor lattice sites, obtained for the Fe-Sn solid solutions.

Magnitudes of the hyperfine field are 60 kG for the smaller split 6-line patterns. This value is similar to 64 kG of the Sn atoms having another Sn atoms at the first and the second neighbor lattice sites of Fe-Sn solid solutions. However the isomer shift value of this component is +1.64 mm/s. This is larger than the value of the corresponding components in the TMS spectra of Fe-Sn solid solutions.

The CEMS spectrum obtained from the specimen implanted by the acceleration energy of 200 and 300 keV was well analyzed by two kinds of 6-line patterns and two kinds of singlet peaks. The 6-line patterns in these CEMS spectra are same to those in the CEMS spectrum obtained from the specimen implanted by the acceleration energy of 400 keV. The singlet peak located at the smaller velocity side has the isomer shift about 0 mm/s. This value corresponds to the Sn^{4+} state. The value of the isomer shift for another singlet peak located at the larger velocity side is about 3.3 mm/s, that is close to the value for β-Sn of 2.53 mm/s.

For the implantation with the acceleration energy of 100 keV, the ^{119}Sn CEMS spectrum obtained is quite different from the other three spectra in Fig.3.1-15. This spectrum was similarly decomposed into two kinds of 6-lines and two kinds of singlet peaks to the spectra obtained from the specimens implanted by the acceleration energy of 200 and 300 keV. The intensities of the singlet peaks much increased compared with those in the spectra obtained from the specimen at the acceleration energy of 200 and 300 keV. At the low acceleration energy of 100 keV, the implanted ^{119}Sn atoms stop at the very shallow part of the target and the local Sn concentration becomes considerably higher than the case of the acceleration energy 300 and 400 keV. The higher concentration of the implanted ^{119}Sn atoms would enhance the formation of the Sn^{4+} state and some states close to β-Sn.

However, the components associated with the vacancy, which were observed in the source experiments13,22), are not observed in any spectra. This is because of the much higher dose of this study than the source experiments.

c) ^{57}Fe CEMS spectra

In the case of the ^{119}Sn ion-implantation into Fe, the microscopic information for Fe atoms of the target can also be obtained by ^{57}Fe CEMS measurements. Figure 3.1-18 shows ^{57}Fe CEMS spectra obtained from the α-Fe foils after the ^{119}Sn ion-implantations at the dose of $5x10^{16}$ ions/cm^2 and the acceleration energies of 100, 200, 300 and 400 keV.

In all CEMS spectra, a minor 6-line pattern was observed additionally to the main 6-line pattern whose isomer shift value and hyperfine field magnitude are almost 0 mm/s and 330 kG. This main 6-line pattern is arising from the α-Fe of the target.

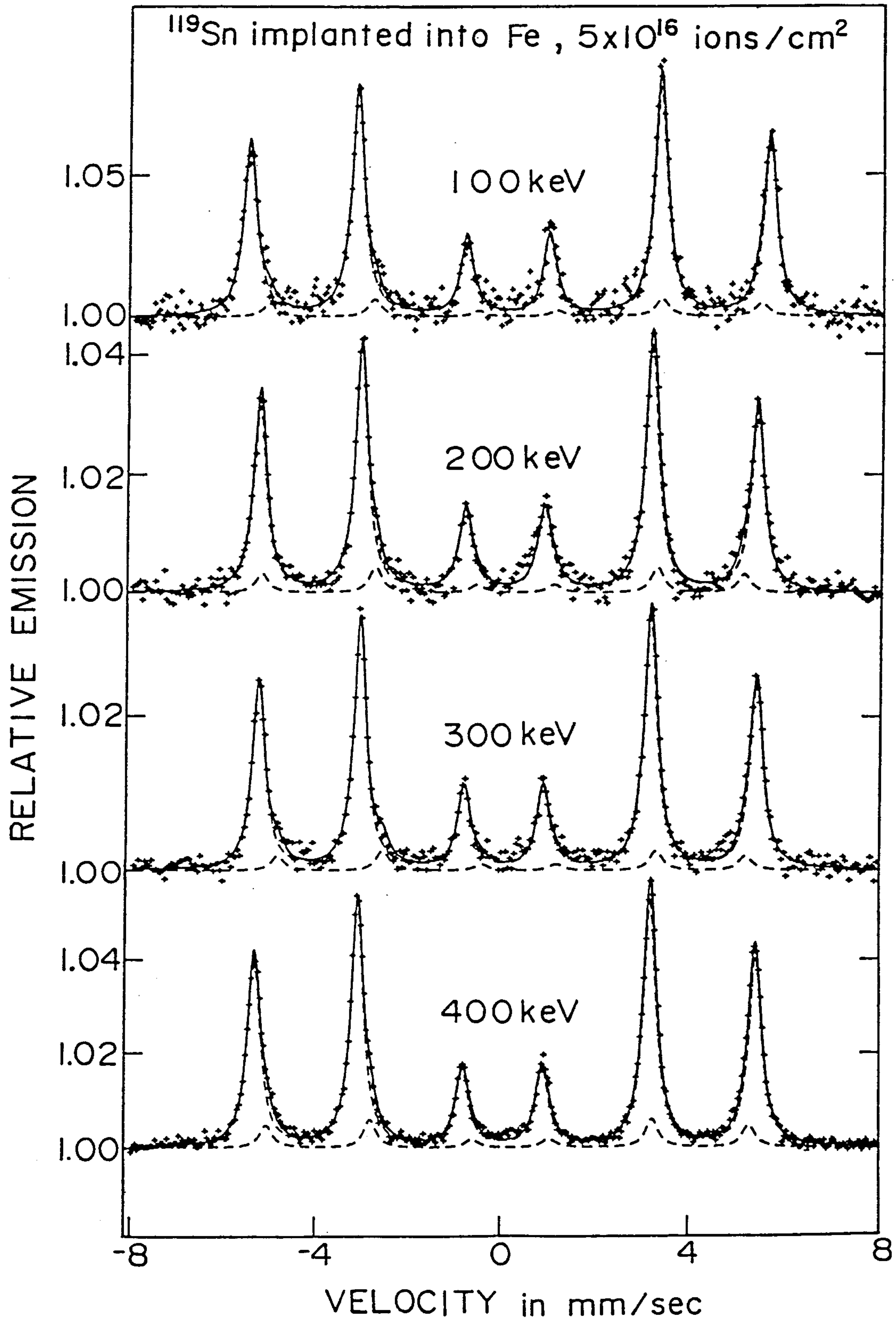

Fig. 3.1-18. ^{57}Fe CEMS spectra of α-Fe foils after ^{119}Sn implantations. Both of the ^{119}Sn implantations and the CEMS measurements were performed at room temperature. These spectra are well analyzed by two kinds of 6-line patterns, as shown by broken lines in the spectra. Velocity scale is relative to α-Fe at room temperature.

The isomer shift and hyperfine field values of minor 6-line patterns are about +0.20 mm/s and 320 kG. These values are a little larger than 0.06 mm/s and 310 kG, evaluated for the Fe atom having one Sn atom at the first neighbor lattice sites by TMS measurements of Fe-Sn solid solutions$^{19)}$. The small quadrupole splitting about +0.2 mm/s is also observed in these minor 6-line patterns. Judging from the results of the corresponding ^{119}Sn measurements, the minor 6-line patterns are due to the Fe atoms having substitutional Sn atoms at the first and second neighbor lattice sites.

The sharp peaks arising from the intermetallic compounds, such as FeSn spectra as shown in Fig. 3.1-14, were not observed in any ^{57}Fe CEMS spectra. In the ^{119}Sn CEMS spectrum obtained from the specimen with the acceleration energy of 100 keV in Fig. 3.1-15, additional singlet peaks to the 6-line patterns of the dissolved Sn into Fe were clearly observed. So that the implanted Sn atoms would form the clusters or oxides by themselves at the regions of the high Sn concentration in α-Fe target. These clusters and oxides may not contain Fe atoms. In the case of the ^{119}Sn implantation into Ni, however, Ni_3Sn intermetallic compounds have been formed at the regions of the high Sn concentration. This different behavior of the implanted Sn atoms in the different target spices may depend on the different defect structure and different mobility of the vacancies in each target.

Substitutional Sn atoms implanted into Ni lattice cannot move after implantation because of the nearly no mobility of the vacancies in Ni at room temperature. If Ni_3Sn intermetallic compounds are once formed, these will not be dissolved because of little mobility of vacancy in Ni metal at room temperature. It is mentioned that the formation of Ni_3Sn intermetallic compounds at the implantation is associated with the radiation enhanced diffusion of Sn atoms. But the radiation enhanced diffusion would not affect to dissolve the formed Ni_3Sn intermetallic compounds.

Sn atoms implanted into Fe can move even after implantation because of the large mobility of the vacancy in Fe at room temperature. On the implantation at room temperature, the effective temperature around the damaged regions would be considerably higher than the room temperature. At this condition, the formation of the Fe-Sn solid solutions would be preferred rather than the FeSn intermetallic compound though it is the equilibrium phase at the room temperature. It implies that the local free-energy of solid solution is lower than that of the intermetallic compound because of the larger configurational entropy of the solid solution than intermetallic compounds during implantation. So the peaks of the FeSn intermetallic compound were not observed in ^{57}Fe and ^{119}Sn CEMS spectra in the case of the ^{119}Sn implantations into Fe. Moreover, at the regions of the high Sn concentration, excess Sn atoms over the maximum solubility of Sn in Fe would form the oxides and clusters of Sn atoms containing no Fe atoms, rather than Fe-Sn intermetallic compounds.

d) TRIM3D computer simulation

TRIM3D computer simulations were carried out and their results are shown in Fig. 3.1-19. The vertical scale of the

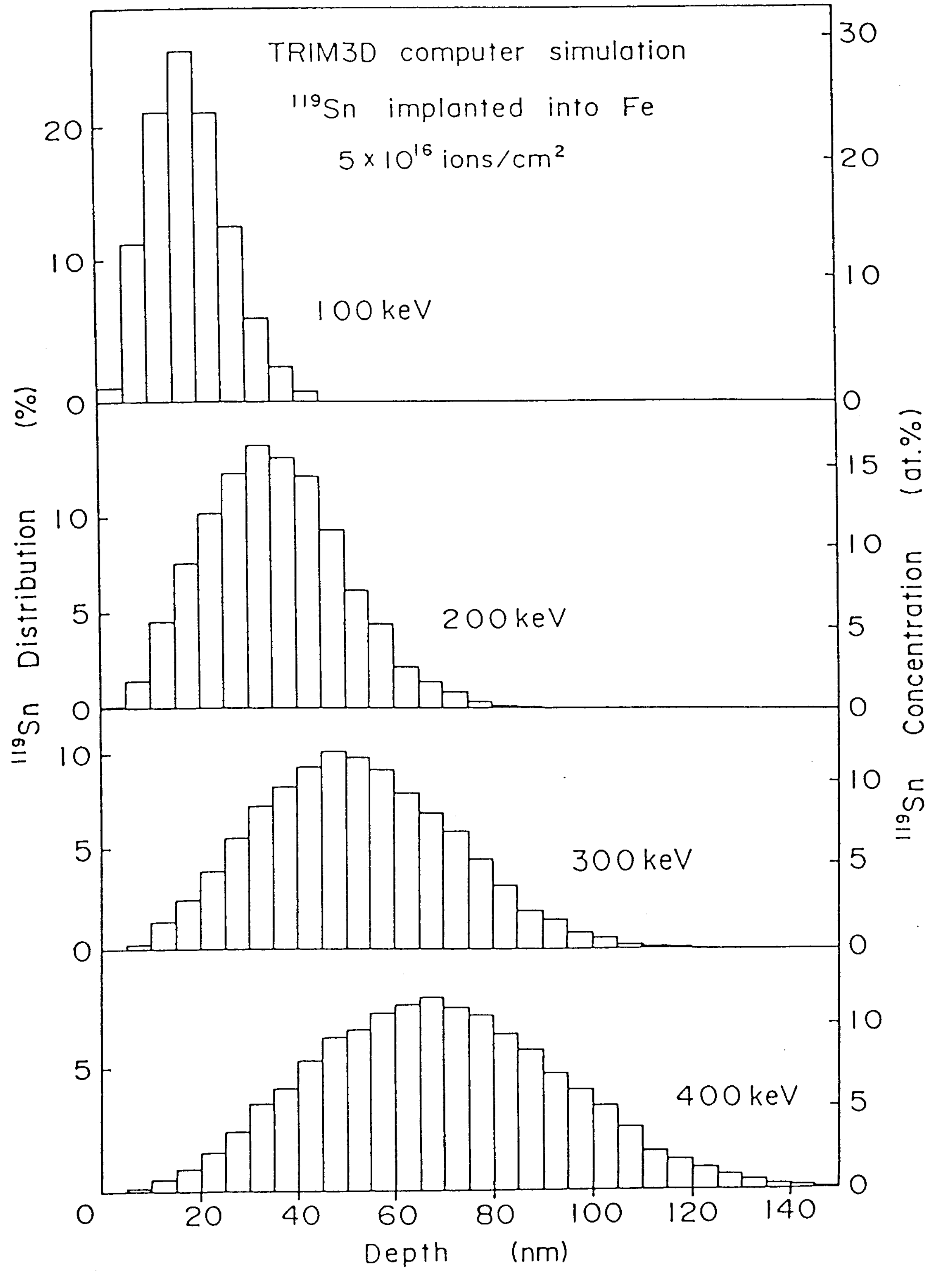

Fig. 3.1-19. ^{119}Sn depth distribution of ^{119}Sn implanted into Fe calculated by using TRIM3D code. The scale of the right hand side indicates the local Sn concentration evaluated by assuming that ^{119}Sn atoms occupy the substitutional sites of Fe matrix.

left hand side indicates the depth distribution of Sn implanted into Fe. The right hand side scale indicates the local Sn concentration calculated by assuming all implanted ^{119}Sn atoms are dissolved into α-Fe and occupy the substitutional sites of α-Fe.

To compare the results from the TRIM3D computer simulation with the CEMS spectra, it must be considered that the detectable efficiency of ^{57}Fe CEMS rapidly decrease with an increase of the depth comparing with the case of ^{119}Sn CEMS. This is due to the different energy of the conversion electrons between ^{57}Fe and ^{119}Sn CEMS. The energy of the mainly detected conversion electrons in ^{57}Fe and ^{119}Sn CEMS are 7.3 and 19.6 keV, respectively.

Figure 3.1-20 shows the ^{119}Sn depth distribution which is the distribution as the lowest figure in Fig. 3.1-19 and smoothly curved lines indicating a dependence of the detectable efficiency of ^{57}Fe and ^{119}Sn CEMS as a function of the distance from surface[23,24). For the small energy of the detected electrons in ^{57}Fe CEMS, the detectable efficiency of ^{57}Fe CEMS rapidly decreases with the depth and it is nearly zero at the depth of 160 nm. On the other hand, the efficiency of ^{119}Sn CEMS quickly decreases to the depth of 30 nm but it becomes nearly constant at the depth from 30 nm to 160 nm. So that the change of the detectable efficiency by the depth must be taken into account as a weight function when the ^{119}Sn depth distributions in Fig. 3.1-19 are compared with the CEMS spectra, especially in the case of ^{57}Fe CEMS.

The ^{119}Sn atoms in the regions of the Sn concentration over 7 at.%, where is hatched in Fig. 3.1-20, has at least one Sn atom at the first and second neighbor lattice sites. The ^{119}Sn

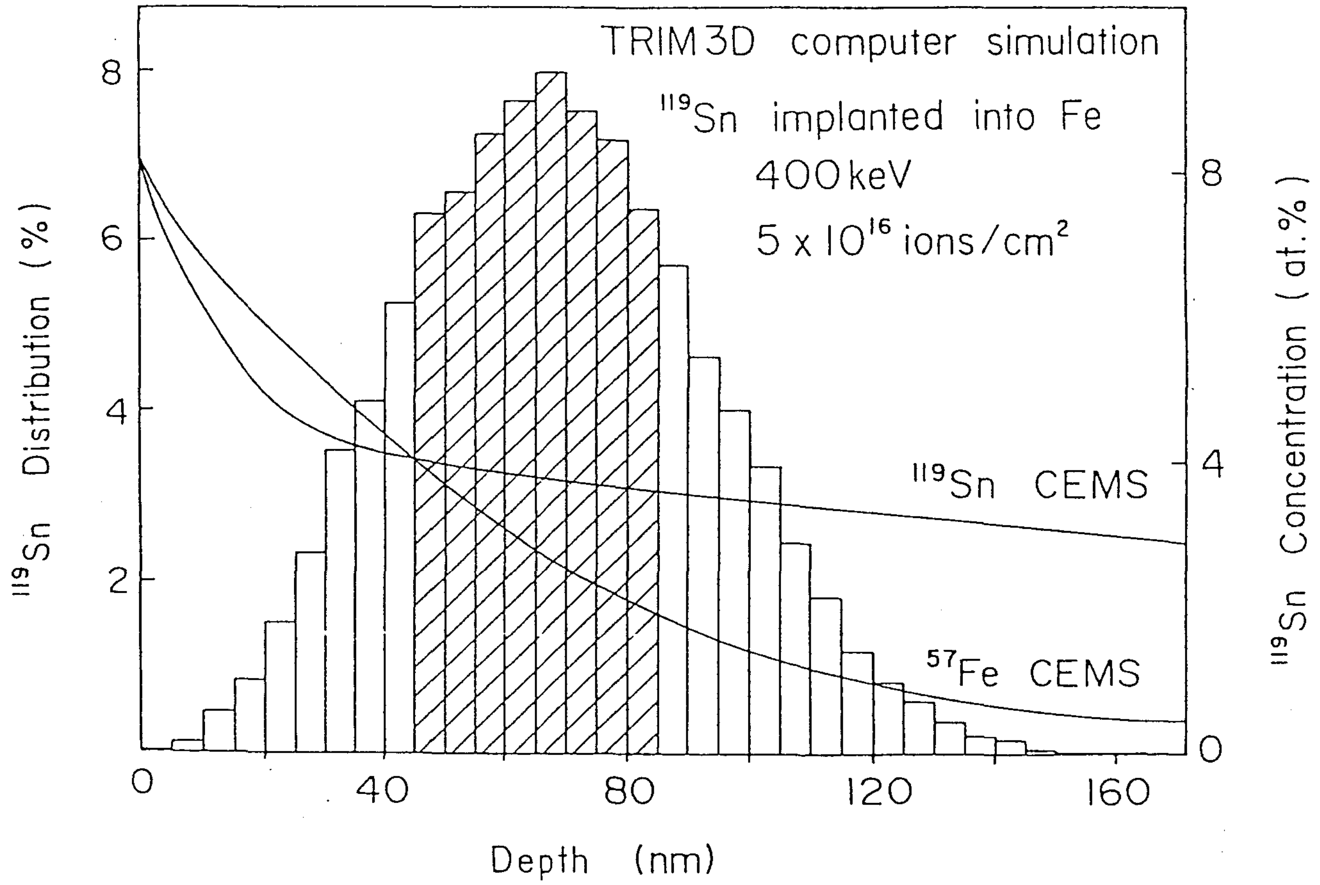

Fig. 3.1-20. ^{119}Sn depth distribution of ^{119}Sn implanted into Fe and the dependence of the detectable efficiency of ^{119}Sn and ^{57}Fe CEMS as a function of depth from the surface. The hatched area in the histogram is where the local Sn concentration is higher than 7 at.%.

atoms in this region will correspond to the 6-line pattern having the smaller split 6-line pattern in the bottom spectrum of Fig. 3.1-15. In the same way, ^{57}Fe atoms in this region will correspond to the minor 6-line pattern in the bottom spectrum of Fig. 3.1-18. The corrected areal ratio of the hatched regions in Fig. 3.1-20 by concerning the detectable efficiency of ^{57}Fe CEMS is 26 % and close to 10 %, which is the areal contribution of the minor component in the bottom spectrum of Fig. 3.1-18. The corrected areal ratio by using the detectable efficiency of ^{119}Sn CEMS is 56 % and close to 43 %, that is the areal contribution of the weak split 6-line pattern in the bottom spectrum of Fig.3.1-15.

In the case of the ^{119}Sn CEMS spectra, the increase of the components corresponding to the oxide and clusters of Sn atoms with the decrease of the acceleration energy is due to the increase of the regions where local Sn concentration are over the maximum solubility of Sn in Fe. But the areal contributions of the oxides and cluster components in ^{119}Sn CEMS spectra could not be explained quantitatively by the Sn depth distributions evaluated from TRIM3D simulations in the case of the specimens at the acceleration energy of 100, 200 and 300 keV. Also ^{57}Fe CEMS spectra obtained from these specimens could not be explained by the Sn depth distribution in Fig. 3.1-19. These are because of the formation of the oxide and clusters of Sn atoms by themselves.

3.1.4 Conclusion

CEMS measurements have been applied to study the microscopic behavior of implanted ^{119}Sn into Ni and Fe metals. The following conclusions are obtained from the analysis of the CEMS spectra and the comparison with the results from TMS and X-ray diffraction measurements and TRIM3D computer simulations.

In the case of the ^{119}Sn implantation into Ni, the implanted ^{119}Sn atoms are divided into two states. One is the substitutional Sn atoms dissolved into the Ni matrix and the other is the Sn atoms in the Ni_3Sn intermetallic compound. These states of the implanted Sn atoms are determined by the local Sn concentration. The Ni_3Sn intermetallic compounds are formed where the local Sn concentration excesses 10.4 at.%, which is the maximum solid solubility of Sn in Ni. The formation of Ni_3Sn intermetallic compound is associated with the radiation enhanced diffusion concerning from little mobility of the vacancy in Ni at room temperature. The dependence of the CEMS spectra on the dose and acceleration energy is well understood by the change of the distribution of the local Sn concentration.

In the case of the ^{119}Sn implantation into Fe, the implanted Sn atoms are divided into the dissolved Sn atoms into Fe matrix and the Sn atoms constructing the oxides and clusters by themselves. At the implantation of the acceleration energy of 400 keV, the implanted Sn atoms is dissolved into α-Fe and both ^{57}Fe and ^{119}Sn CEMS spectra are well explained by the local Sn concentration.

At the implantation of acceleration energy of 100, 200 and 300 keV, oxides and clusters of Sn atoms were formed additionally to the dissolved Sn atoms into Fe. The formed oxides and clusters do not contain Fe atoms. This is quite different from the fact that Ni_3Sn intermetallic compounds were formed by the Sn implantation into Ni. This different behavior between the implanted Sn atoms into Fe and Ni may be originated from the difference of the defect structure and the mobility of the vacancy in Fe and Ni at room temperature.

These results demonstrate that CEMS is a powerful method to study the behavior of the implanted atoms, especially to discuss the depth distribution of the implanted atoms.

3.1.5 References

1. "Ion-Implantation", Ed. by J.K.Hirvonen, Academic Press, New York, (1980).
2. S. Namba et al., "Ion Chunyu Gijutsu", Ed. by S.Namba, Kogyoh Chosakai, Tokyo, (1975).
3. The morning edition of the Mainichi dated July 6, 1988.
4. I.J.R.Baumvol, J. Appl. Phys., 52(1981)4583.
5. G.Dearnaley, "Applications of Ion Beams to Metals", Ed. by S.T.Picraux, E.P.EerNisse and F.L.Vook, Plenum, New York, (1974), p63.
6. J.P.Biersack and L.G.Haggmark, Nucl. Instrum. Methods, 174(1980)257.
7. M.J.Makin, S.N.Buckley and G.P.Walters, J. Nucl. Materials, 68(1977)161.
8. M.Hansen, "Constitution of Binary Alloys", McGraw-Hill, New York, (1958).
9. V.Marian, Ann. de Phys., 7(1937)494.
10. A.J.F.Boyle, D.St.P.Bunbury and C.Edwards, Phys. Rev. Lett., 5(1960)553.

11. D.C.Price, J. Phys. F, 4(1974)639.

12. "Index to the Powder Diffraction File (Inorganic)", Ed. by J.V.Smith, A.S. Beward, L.G.Berry, B.Post and S.Weissmann, ASTM, Philadelphia, (1963).

13. H.de Waard, F.Pleiter, D.O.Boerma, L.Niesen and G.L.Zhang, Nucl. Instrum. Methods, 209/210(1983)899.

14. G.Weyer, F.T.Pedersen H.Grann and K.Bonde Nielsen, Hyp. Int., 29(1986)1233.

15. P.Rahlfs, Metallwirt., 16(1937)343.

16. S.Ishino, "Shosha Sonsho", University of Tokyo Press, Tokyo, (1979).

17. O.C.Kistner, A.W.Sunyar and J.B.Swan, Phys. Rev., 123(1961)179.

18. T.E.Cranshaw, J. Phys. F, 17(1987)1645.

19. I.Vincze and A.T.Aldred, Phys. Rev. B, 9(1974)3845.

20. G.Trumpy, E.Both, C.Djéga-Mariadassou and P.Lecocq, Phys. Rev. B, 9(1970)3477.

21. H.de Waard, Proc. Int. Cof. on Mössbauer Effect, Jaipur, 1981, (Ind. Nat. Sci. Acad., New Delhi, 1982), p.5.

22. G.Weyer, F.T.Pedersen and H.Grann, Nucl. Instrum. Methods, B7/8(1985)103.

23. D.Liljequist, T.Ekdahl and U.Bäverstam, Nucl. Instrum. Methods, 155(1978)529.

24. F.Salvat, R.Mayol, J.D.Martinez and J.Parellada, Nucl. Instrum. Methods, B6(1985)547.

3.2 Work hardening of Hadfield steel

3.2.1 Hadfield steel

An austenitic high-manganese steel which contains 12 - 14 wt.% of manganese and 0.8 - 1.2 wt.% of carbon is well known as Hadfield steel named after its inventor. The remarkable hardening at the worked surface of Hadfield steels is demonstrated in Fig. 3.2-1. The values of micro Vickers hardness near surface of these steels are nearly three times larger than those of inner parts. From this remarkable hardening, Hadfield steel has been used widely as an abrasion resistant steel, such as the jaw of a power shovel and the crossing of rails. Moreover, the application of Hadfield steel to the structural materials of linear motor cars and nuclear fusion reactors is attempted owing to its nonmagnetic property1,2).

There are a lot of reports to discuss the mechanism for the remarkable work hardening of Hadfield steel. In the earlier reports, the transformation of austenite to α' martensite3,4) was given for the reason of work hardening of Hadfield steel, but the formation of α' martensite after cold-working has not been confirmed experimentally. Other reasons for work hardening of Hadfield steel, such as the formation of carbides5), the fragmentation of the grain boundary into small crystallites or blocks6,7), the formation of twins8-10), the interaction between solute carbon atoms, the stacking faults11) and the formation of ε martensite12,13), etc. are reported. In spite of these efforts, there is no explicit interpretation for the mechanism of work hardening of Hadfield steel. Recently, Mössbauer spectros-

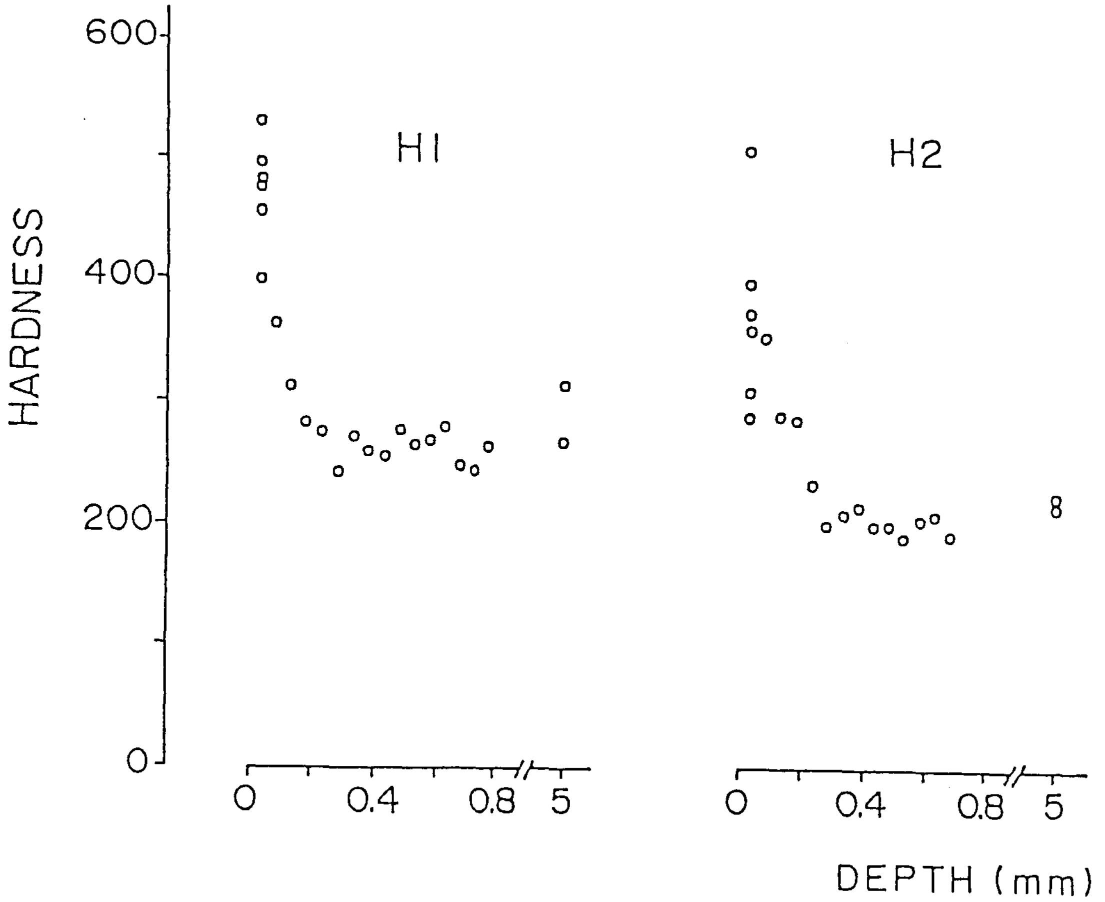

Fig. 3.2-1. Micro Vickers Hardness at various depths near the surface of high-manganese carbon steels, H1 and H2.

copy applied to the microscopic investigation of high-manganese steels. Dastur and Leslie[14)] reported that the Mössbauer spectra showed no change between before and after the tension of specimens at several temperatures. They concluded that work hardening of Hadfield steels is caused by dynamic strain aging effect, which cannot be detected by Mössbauer measurement. Saeki et al.[15)] applied Mössbauer measurements to study the increase of the magnetic permeability of high-manganese steels containing Cr by cold-rolling and heat-treatment. They concluded that the increase of the magnetic permeability is responsible for the formation of α' martensites. Huffman and Ouchi[16)] observed ε martensite in cold-rolled Hadfield steel by Mössbauer measurements at a low temperature, but did not observe α' martensite.

On the above investigations, the specimens used were deformed by the tensile deformation or the cold-rolling of the whole part of specimens, whose conditions are not similar to the conditions at practical use of Hadfield steel. In the present study, CEMS was applied to the measurement of microscopic property near the surface of Hadfield steels worked by shot-peening or sand blast treatments, whose conditions are just similar to the practical use. Since the X-ray backscattering Mössbauer spectroscopy (XBMS) provides the microscopic information of non-deformed deeper area from the worked surface in contrast to the CEMS, XBMS measurements were also performed using the same specimens with the CEMS measurements. The mechanism of work hardening of Hadfield steel is discussed by comparing the results from CEMS and those from XBMS. In addition, the transmission

Mössbauer measurements (TMS) at room temperature and 20 K were carried out for the foil specimen of Hadfield steel prior to and after heavy rolling in order to clarify the formation of ε martensite.

3.2.2 Sample preparation and experimental procedure

The chemical compositions of high-manganese steels investigated in this study are listed in Table 3.2-1. All of the specimens were melt in air and annealed for 3.6 ks at 1423 K. Ingots of H1, H2 and H3 were hot-rolled down to 11 mm in thickness and cut in 20x20 mm square. These specimens were subsequently annealed for 1.8 ks at 1323 K and then quenched into water. One of the specimens was shot by small steel balls (shot-peening treatment) to harden its surface layers. Before the above treatments, the specimen surfaces were pickled using some acid. Ingots of specimens of A and B were prepared by the same heat treatment as the specimens of H1, H2 and H3, but the specimens were cut into 0.5 mm in thickness and 20 mm in diameter and were sand-blasted for the surface work hardening.

For the specimen of H3, some foils whose thickness was about 110 μm, were cut out from the unshotted block and cold-rolled down until about 40 μm. One of these foils was annealed for 1.8 ks at 1323 K in silica tube under vacuum and then quenched into water. This was used as an original foil specimen. These foils were used for ^{57}Fe TMS at room temperature and 20 K.

The ^{57}Fe CEMS measurements at room temperature were performed by using a newly developed gas proportional electron

Table 3.2-1. Compositions of Hadfield steels used in the present study (wt.%).

specimen	Mn	C	Si	P	S	Al
A	12.0	1.1	-	-	-	-
B	15.0	0.75	-	-	-	-
H1	13.35	0.45	0.11	0.005	0.0057	0.006
H2	13.36	0.84	0.11	0.005	0.0064	0.006
H3	13.25	0.82	0.11	0.005	0.0059	0.006

counter in order to achieve the higher counting rate. The electron counter was operated in flowing Q gas (99 % He + 1 % C_4H_{10}) about 3 cm^3/min during all CEMS measurements. In the case of ^{57}Fe XBMS, the gas proportional X-ray detector which has the similar construction to the electron counter was used with 3 cm^3/min flow of PR gas (90 % Ar + 10 % CH_4).

All Mössbauer spectra were measured with a combination of a velocity transducer and a multichannel analyzer operating in a time mode. In every Mössbauer measurements, 25 mCi ^{57}Co in Rh at room temperature was used for the 14.4 keV Mössbauer γ-ray source and Doppler velocity scale was calibrated using a spectrum obtained from the metallic iron at room temperature. These Mössbauer spectra were analyzed by the least-square-fit assuming the superposition of Lorentzian lines (thin foil approximation). The X-ray diffraction measurements were also performed to determine the structure around the surface of specimens.

3.2.3 Results and discussion

1) Comparison of CEMS and XBMS spectra

Typical ^{57}Fe CEMS spectra of Hadfield steel of A before and after working are shown in Fig. 3.2-2. Only one singlet like peak is found in the spectrum of each specimen. For the detailed analysis, the CEMS measurements were done under magnifying the Doppler velocity scale near 0 mm/s. Figure 3.2-3 shows the CEMS spectra obtained from the specimen A, magnifying the Doppler velocity scale near 0 mm/s of Fig. 3.2-2. The existence of a minor peak additionally to the singlet peak is

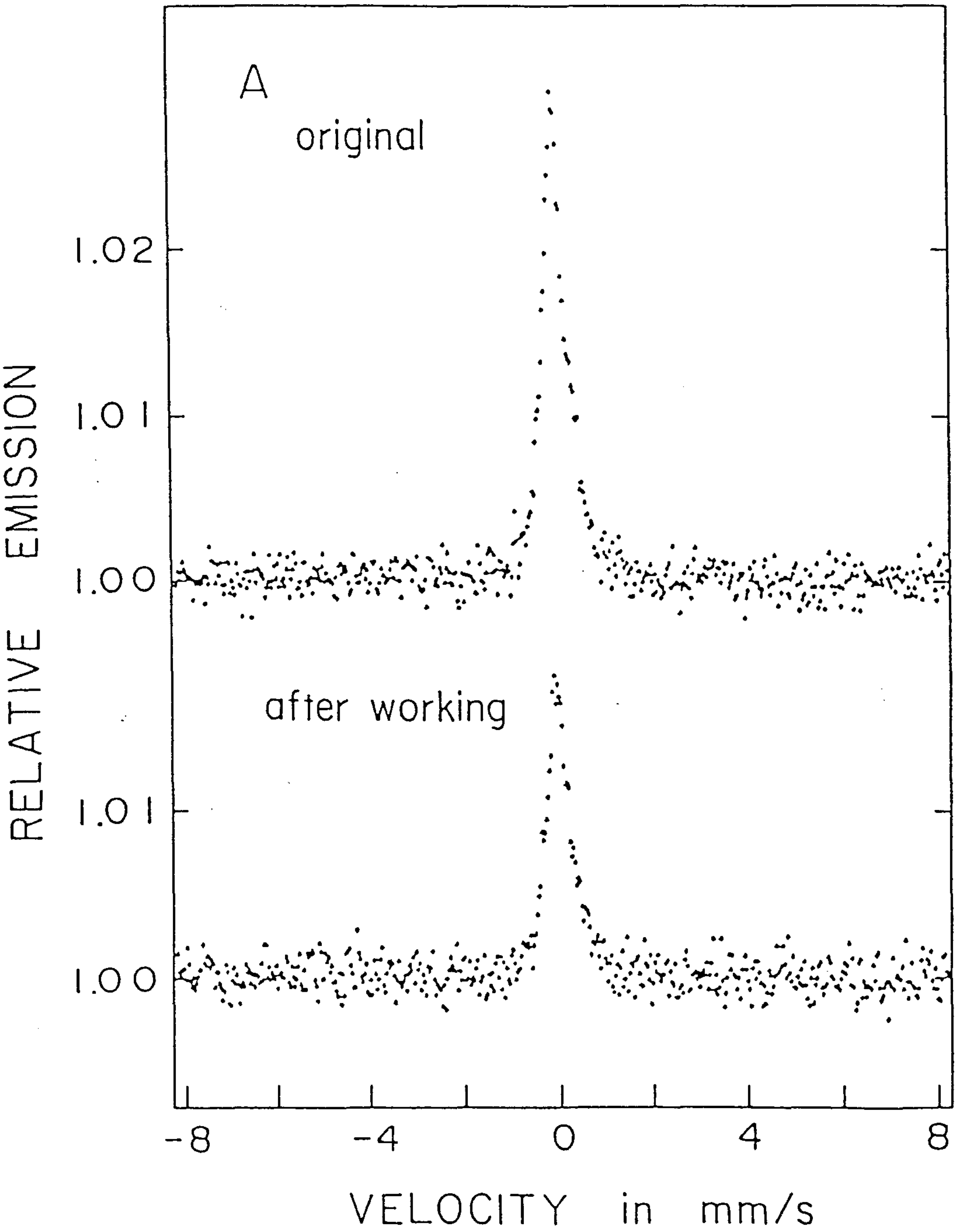

Fig. 3.2-2. ^{57}Fe CEMS spectra of the typical Hadfield steel, A, measured at room temperature. Only one singlet peak is observed. Velocity scale is relative to α-Fe at room temperature.

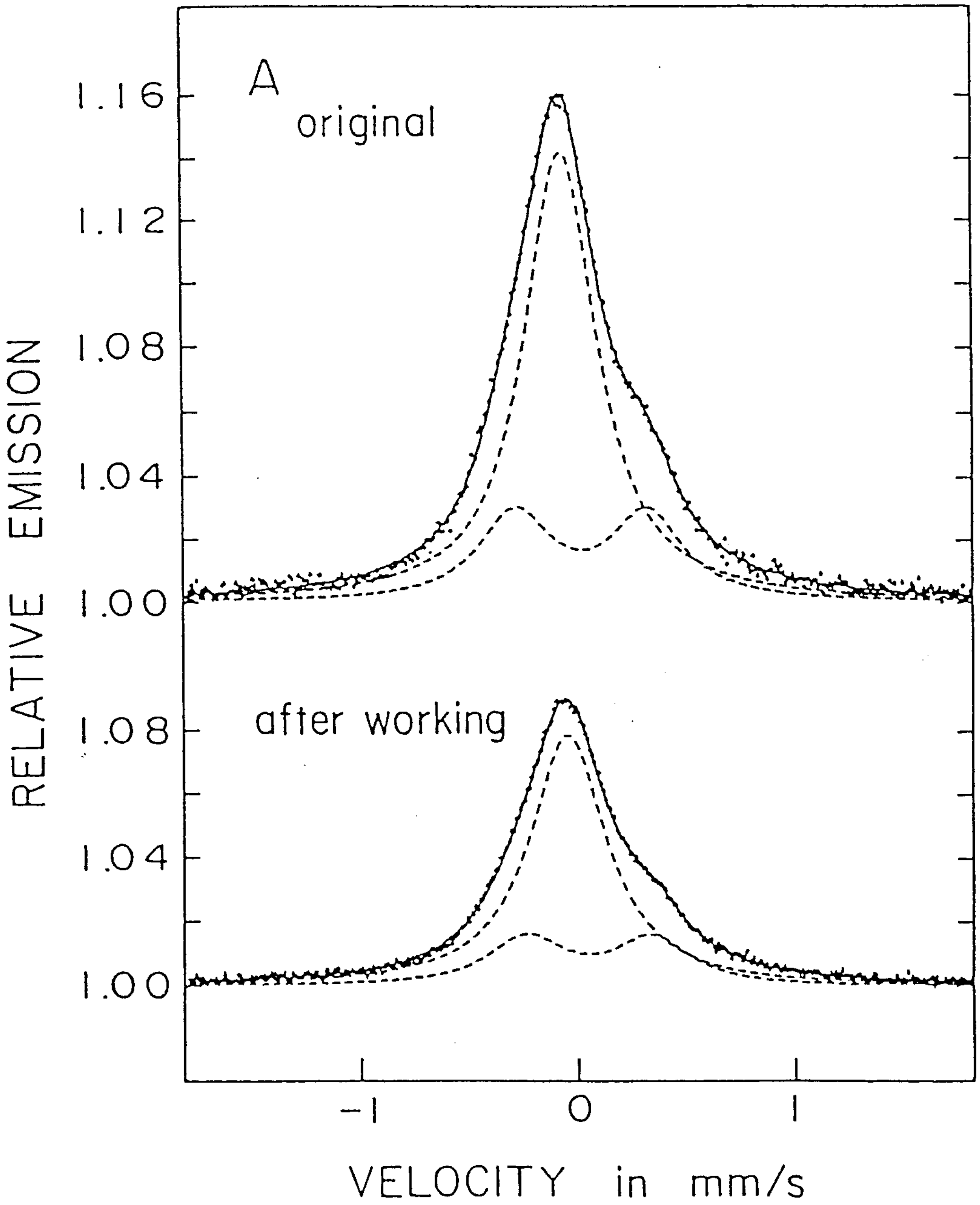

Fig. 3.2-3. ^{57}Fe CEMS spectra of Hadfield steels, A, measured at room temperature. All spectra were analyzed into two components, except for the steel B. Velocity scale is relative to α-Fe at room temperature.

found as shown in Fig. 3.2-3. The spectra in Fig. 3.2-3 can be well reproduced by the superposition of one singlet peak and one doublet peak except for the specimen of B, which was decomposed into one singlet peak and two doublet peaks.

Similar spectra in Fig. 3.2-4 to CEMS spectra in Fig. 3.2-3 were acquired by XBMS and analyzed into the same components as those of CEMS spectra. It should be noted that the full width at half maximum (FWHM) of the doublet peak constrained to be the same with that of the singlet peak in above analysis.

Comparing the CEMS or XBMS spectrum between before and after working, the shape of Mössbauer spectra did not change distinctly in any specimens, so that Mössbauer spectra recorded after working were decomposed into same components as those before working.

At room temperature, TMS spectra of H3 as shown in Fig. 3.2-5 hardly changed between before and after rolling. These spectra are quite similar to XBMS spectra. At 20 K, the spectrum as shown in Fig. 3.2-6 was a broad and complex one because of the mixed hyperfine interaction of electric quadrupole and magnetic dipole interactions. Electric field gradients are due to the near neighbor interstitial carbon atoms and the magnetic splittings are due to the antiferromagnetic order of iron atoms in the high-manganese steel at low temperatures. An additional paramagnetic component was found in the spectrum after rolling as shown in Fig. 3.2-6, which is clearly seen in the differential spectrum shown at the bottom of Fig. 3.2-6.

Mössbauer parameters obtained from the two components fitting procedure are listed in Table 3.2-2.

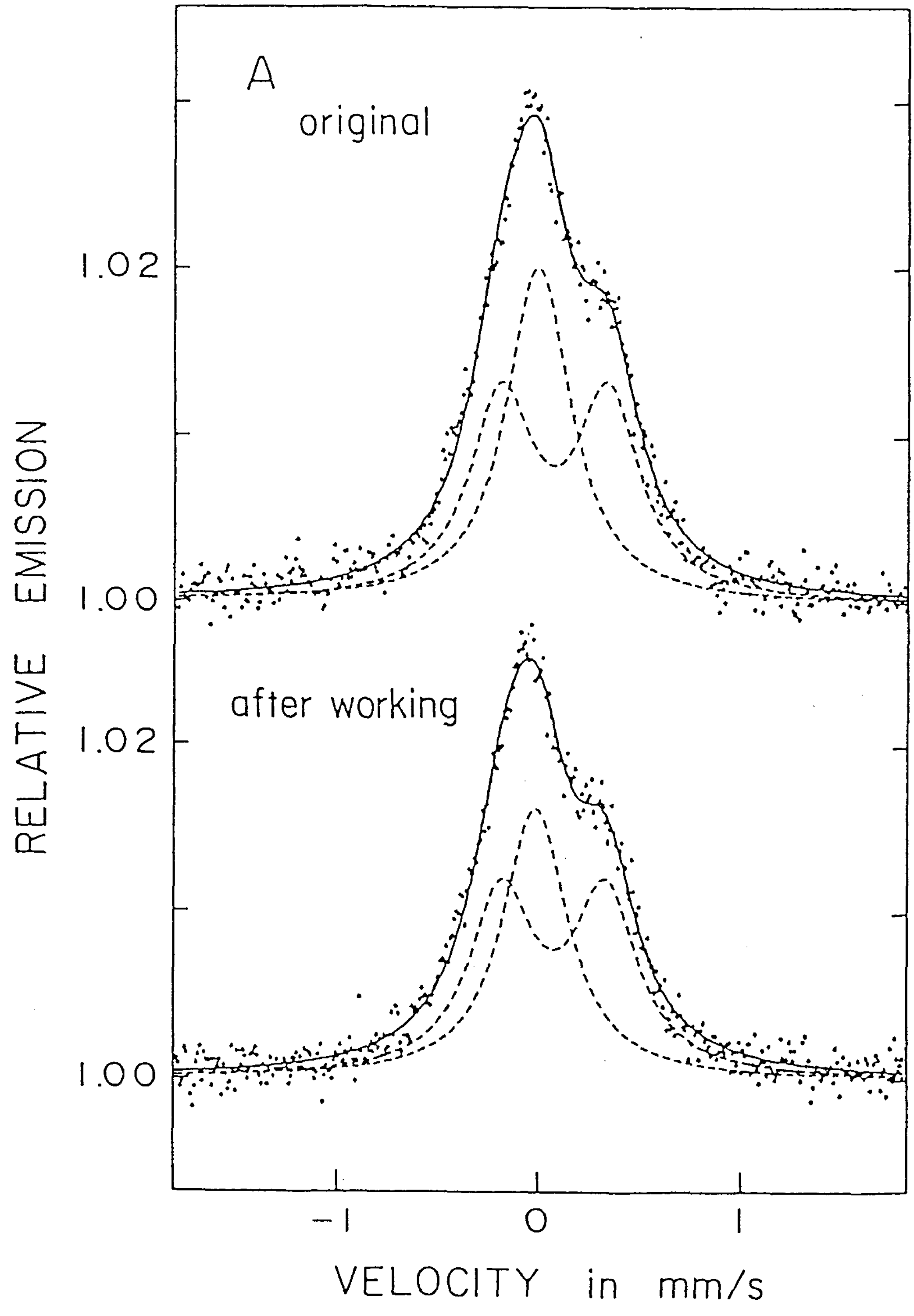

Fig. 3.2-4. ^{57}Fe XBMS spectra of Hadfield steel, A, measured at room temperature. These are similar to CEMS spectra. Velocity scale is relative to α-Fe at room temperature.

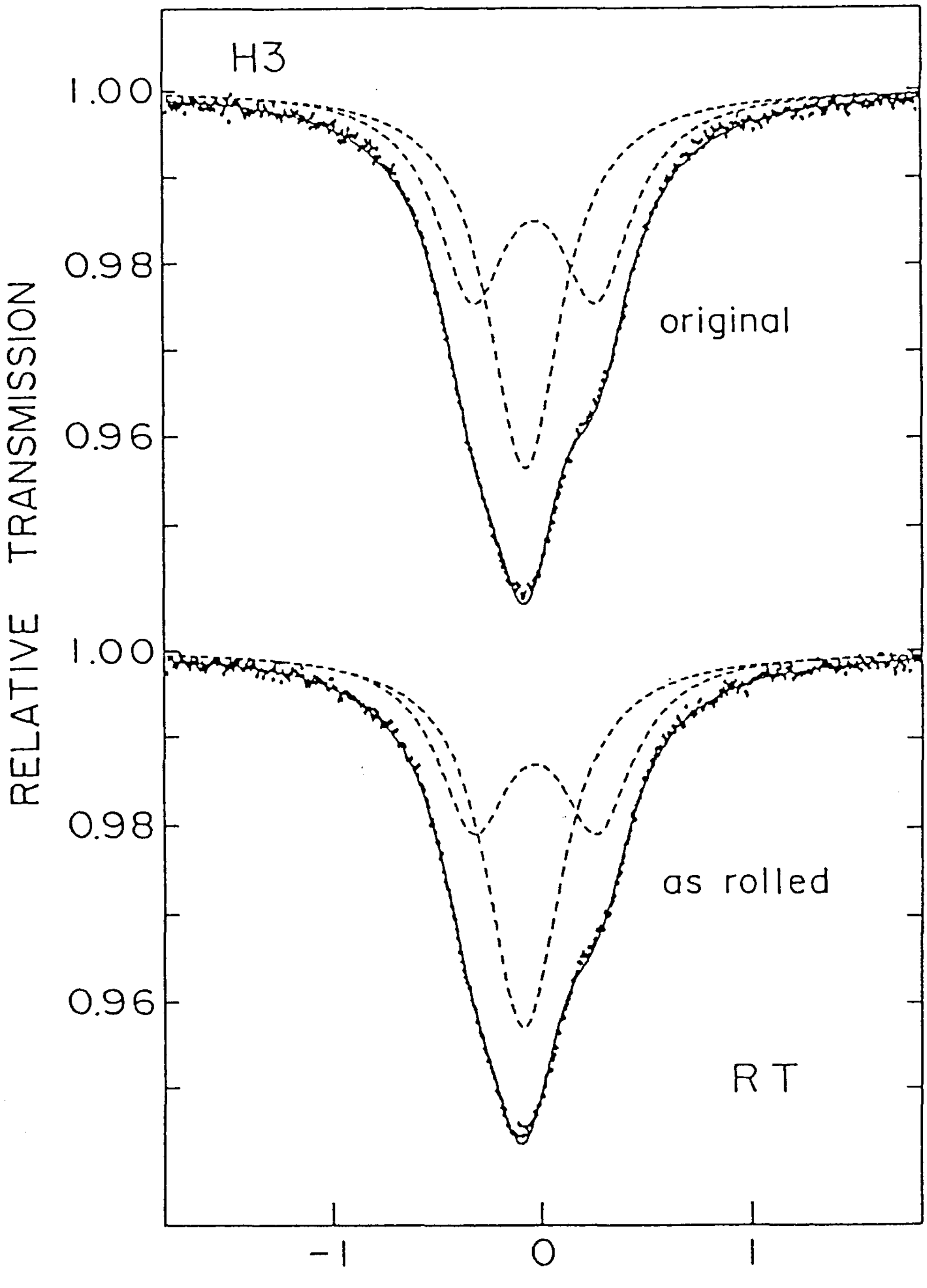

Fig. 3.2-5. ^{57}Fe TMS spectra of Hadfield steel, H3, before and after cold-rolling, measured at room temperature. Velocity scale is relative to α-Fe at room temperature.

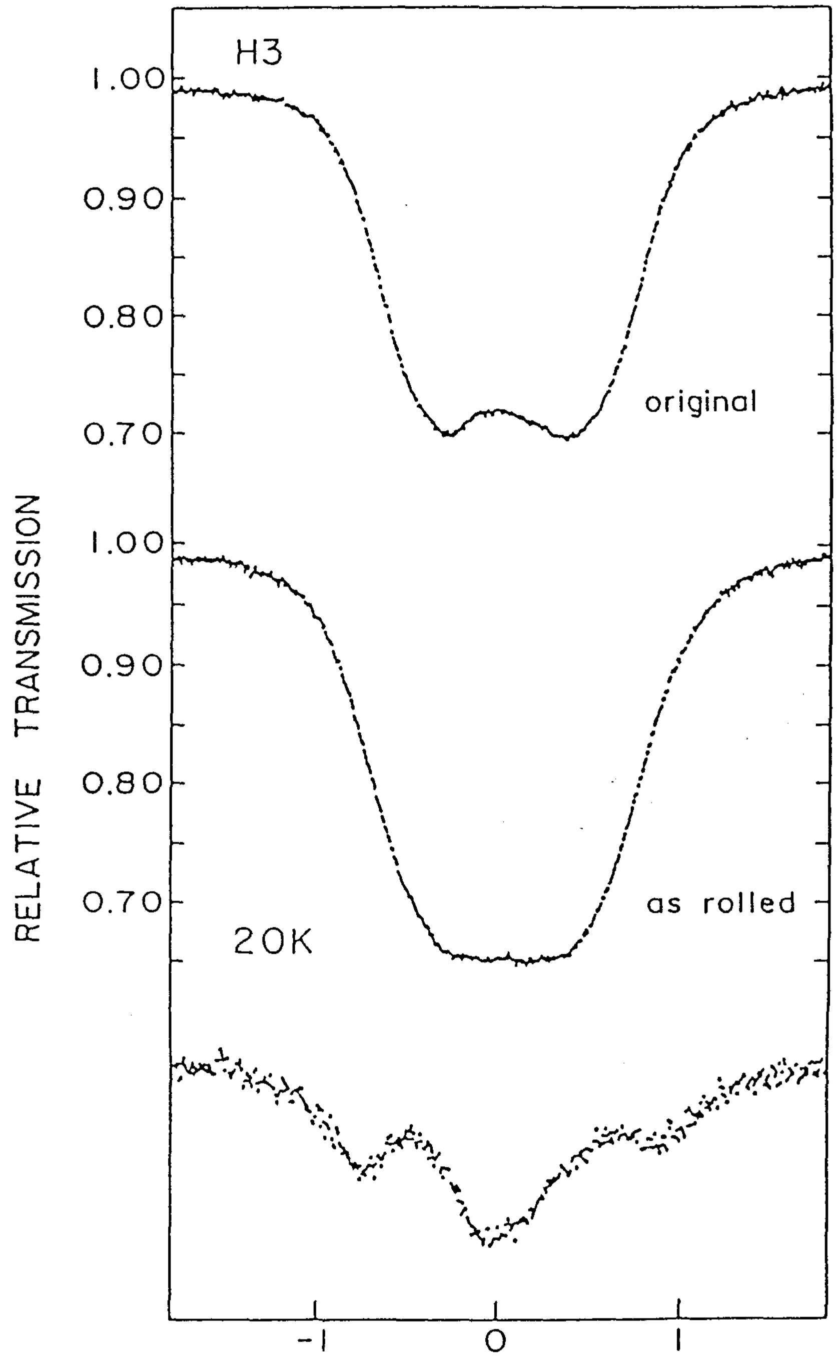

Fig. 3.2-6. ^{57}Fe TMS spectra of Hadfield steel, H3, before and after cold-rolling, measured at 20 K. The figure at the bottom is the differential spectrum between original and rolled specimens. Velocity scale is relative to α-Fe at room temperature.

Table 3.2-2. Mössbauer parameters of CEMS, XBMS and TMS spectra measured at room temperature. I.S. is isomer shift relative to α-Fe at room temperature. Q.S. is electric quadrupole splitting $1/2e^2qQ(1+\eta^2/3)^{1/2}$.

* An additional doublet peak corresponding to oxide.

		Singlet	Doublet		
method	specimen	I.S. (mm/s)	I.S. (mm/s)	Q.S. (mm/s)	Area (%)
CEMS	A original	-0.074(3)	0.01(1)	0.604(7)	29(2)
	worked	-0.053(3)	0.04(1)	0.579(8)	27(2)
	B original	-0.088(3)	0.007(7)	0.544(4)	15(2)
	worked*	-0.09(1)	-0.04(2)	0.48(2)	26(2)
	H1 original	-0.090(3)	0.00(1)	0.54(1)	9(1)
	worked	-0.094(3)	0.08(3)	0.53(2)	8(1)
	H2 original	-0.080(2)	0.013(8)	0.598(6)	19(1)
	worked	-0.083(5)	0.02(2)	0.581(9)	20(1)
XBMS	A original	-0.001(4)	0.07(2)	0.52(1)	54(3)
	worked	-0.014(7)	0.07(2)	0.51(1)	57(4)
	B original	-0.043(3)	0.04(2)	0.53(2)	41(3)
	worked	-0.020(7)	0.08(3)	0.50(2)	53(3)
	H1 original	-0.102(5)	-0.06(3)	0.56(3)	19(6)
	worked	-0.109(4)	-0.02(6)	0.56(6)	21(6)
	H2 original	-0.085(5)	-0.06(3)	0.57(5)	29(5)
	worked	-0.052(4)	0.00(2)	0.55(4)	34(4)
TMS	H3 original	-0.080(7)	-0.036(9)	0.585(5)	50(1)
	rolled	-0.089(4)	-0.037(7)	0.586(6)	47(1)

2) Effects of working on Mössbauer spectra

The singlet peak observed in CEMS spectra of Fig. 3.2-2 is responsible for the paramagnetic property of austenitic high-manganese steel. A widely spread sextet peak of ferromagnetic phase such as α' martensite is not found in any spectra. If α' martensite were formed by working, a ferromagnetic sextet peak could appear in CEMS spectra of Fig. 3.2-2. Since no sextet peak is observed in the spectra of the specimens after working, α' martensite is not formed by working and α' martensite has no relation to work hardening of Hadfield steel.

CEMS and XBMS spectra of the original specimens in Figs. 3.2-3 and 3.2-4 make it clear that the Fe atomic state in the single austenitic phase before working is divided into two states, corresponding to one singlet peak and one doublet peak. This is because for the existence of the carbon atom at the octahedral interstitial site[14,16,17]. The carbon atom at the near neighbor interstitial site distorts the cubic symmetry of fcc Fe lattice and gives rise to the electric field gradient at its neighbor ^{57}Fe nucleus. Under certain electric field gradient, the first excited state of ^{57}Fe nucleus is split into two by the electric quadrupole interaction and such ^{57}Fe nuclei will appear as a doublet peak in the Mössbauer spectrum.

The values of quadrupole splitting, which is denoted by the velocity difference between two tops of the doublet peak, are ranged from 0.51 mm/s to 0.60 mm/s and are similar to 0.598 mm/s of Fe-16wt.%Mn-0.75wt.%C-1.7wt.%Cr reported by Huffman and Ouchi[16), but smaller than 0.63 mm/s of Fe-11.4wt.%Mn-1.13wt.%C by Dastur and Leslie[14), 0.659 mm/s of Fe-12.3wt.%Mn-1.01wt.%C by Sastri and Ray[17)] or 0.62-0.66 mm/s of Fe-C austenitic steels[18)].

The doublet peaks in Figs. 3.2-3 and 3.2-4 correspond to the ^{57}Fe atoms having some carbon atoms at the neighbor interstitial sites and the singlet peaks are due to the ones having no carbon atom at that site.

Areal ratio of doublet and singlet peaks in the spectrum corresponds to the ratio of their products between their number of iron atoms and recoil-free fractions, when the saturation effects rising from the thick absorber[19)] and the polarization effects in hyperfine interactions can be neglected. Since effective thickness for the CEMS measurements is always much smaller than the case of XBMS and TMS measurements, the areal ratio in CEMS spectra contains almost no saturation effect, but in XBMS and TMS spectra, the saturation effects should be taken into account. Detailed analysis containing the saturation effects have been performed and will be reported in elsewhere[20)]. In present study, we used a thin foil approximation in which the spectrum is assumed to be an overlapped Lorentz functions. Under this approximation, the number of iron atoms and recoil-free fraction for each component can be discussed from their areal ratio in spectrum.

Assuming the random distribution of carbon atoms at interstitial sites of fcc lattice, the probability P(n) to find the iron atoms, which have n carbon atoms at the neighbor interstitial sites, is given by

$$P(n) = {}_{14}C_n (1-x)^{(14-n)} x^n$$

where $x=c/(100-c)$.

Where c is the atomic concentration of carbon atom in austenite fcc lattice. The number of 14 in the above equation corresponds to the sum of the number of the first and the second nearest octahedral interstitial sites of fcc lattice. The values of P(n) for each specimen are tabulated in Table 3.2-3.

In order to determine the correct values of the areal intensity ratio for each component in a spectrum, the difference of recoil-free fraction in each component must be taken into account when the ^{57}Fe atoms corresponding to each peak are surrounded by different environments. Recoil-free fraction, which is defined by the probability to observe the zero phonon absorption of γ-ray by the ^{57}Fe nucleus, depends on the local vibrational state of the lattice at the probe ^{57}Fe atom. It will become different when the carbon atom occupies the near neighbor interstitial site of probe ^{57}Fe atoms. In the present investigation, however, the recoil-free fraction is supposed as the constant whether the carbon atom exists or dose not exist at the near neighbor interstitial site.

The values of areal ratio of the doublet peak to the whole area are shown in Table 3.2-2 and it is found that P(0) of each specimen well agrees with the areal ratio of the singlet peaks in XBMS and TMS spectra. So the doublet peaks in Mössbauer spectra are owing to the ^{57}Fe atoms having more than one carbon atom at the first or the second nearest interstitial sites. It should be noted that the existence of the carbon atoms at the neighbor interstitial sites causes the slightly larger isomer shift value of the doublet peak, which is shown by the center of Doppler velocity of the two peaks, than that of the singlet. In

Table 3.2-3. The values of P(n), probabilities of the iron atom having n carbon atoms at the nearest and the second nearest neighboring interstitial sites in fcc lattice. Random distribution of interstitial carbon atoms is assumed.

specimen	P(0)	P(1)	P(2)	P(3)	P(4)
A	0.477	0.363	0.128	0.028	0.004
B	0.606	0.309	0.073	0.011	0.000
H1	0.738	0.227	0.032	0.003	0.000
H2	0.569	0.327	0.088	0.014	0.002
H3	0.579	0.323	0.084	0.013	0.001

the case of CEMS measurement, the isomer shift values of singlet peaks range from -0.094 mm/s to -0.053 mm/s and those of doublet peaks from +0.00 mm/s to +0.08 mm/s relative to α-Fe at room temperature.

The intensity of the doublet peak in CEMS spectrum of specimen A, H1 and H2 is nearly half of that in XBMS spectra for each specimen. This reduction in intensity of the doublet peak, which depends on the carbon concentration, suggests that the decarburization occurred at the surface layers of specimens even before working21).

After working, the shape of CEMS or XBMS spectra is almost same and hardly distinguishable with that of original one as shown in Figs. 3.2-3 or 3.2-4 except for specimen B. An additional peak to one singlet and one doublet peaks is observed in CEMS spectrum of worked specimen B. The isomer shift and quadrupole splitting values of this peak were 0.46(3) mm/s relative to α-Fe at room temperature and 0.72(4) mm/s respectively. These values are close to the values of Fe-Mn oxide reported in ref. 16 so that the oxidization at the surface of specimen B occurred during the sand blast treatment. The specimen B is eliminated from the following discussion for its superposition of the unexpected oxide component.

In each specimen, CEMS or XBMS spectra did not show any appreciable change between before and after working. The doublet peak intensity, which reflects the local carbon concentration, is almost same before and after working. This implies that no carbide and no segregation of carbon atoms occurred during the working treatment. The formation of carbides and carbon segregations is not the origin of work hardening of Hadfield steels.

X-ray diffraction measurements (Fig. 3.2-7) show that ε martensite is formed in the specimen of H1 by working, although the CEMS and XBMS spectra hardly changed by working. Mössbauer parameters rising from ε martensite and γ austenite of high-manganese steels give quite similar values at room temperature. The isomer shift value of an Fe-23.9at.%Mn steel, which does not contain carbon and higher manganese concentration than Hadfield steels, is -0.100(5) mm/s for γ phase obtained from the foil specimen annealed at 1373 K and subsequently quenched. On the other hand, the isomer shift value of that steel is -0.115(3) mm/s for ε phase obtained from the strongly cold-rolled foil specimen. These values are measured at room temperature. The dependence of isomer shift values of both phases on manganese concentration is quite similar22) with each other. On the Mössbauer measurement at room temperature, it is so difficult to distinguish the peak of ε phase from the γ matrix for their similarity of Mössbauer parameters that the evidence for the formation of ε phase could not be found by the room temperature Mossbauer spectra of H1 after working.

From the fact that the less carbon high-manganese steels than Hadfield steel easily transform from γ phase to ε phase by working11,23), the low carbon concentration of specimen H1, nearly half of Hadfield steel composition, enhances the formation of ε phase by working. The decarburization at near the surface of other specimens, A, B and H2 suggests the possibility of the transformation of ε from γ. Although no peaks corresponding to

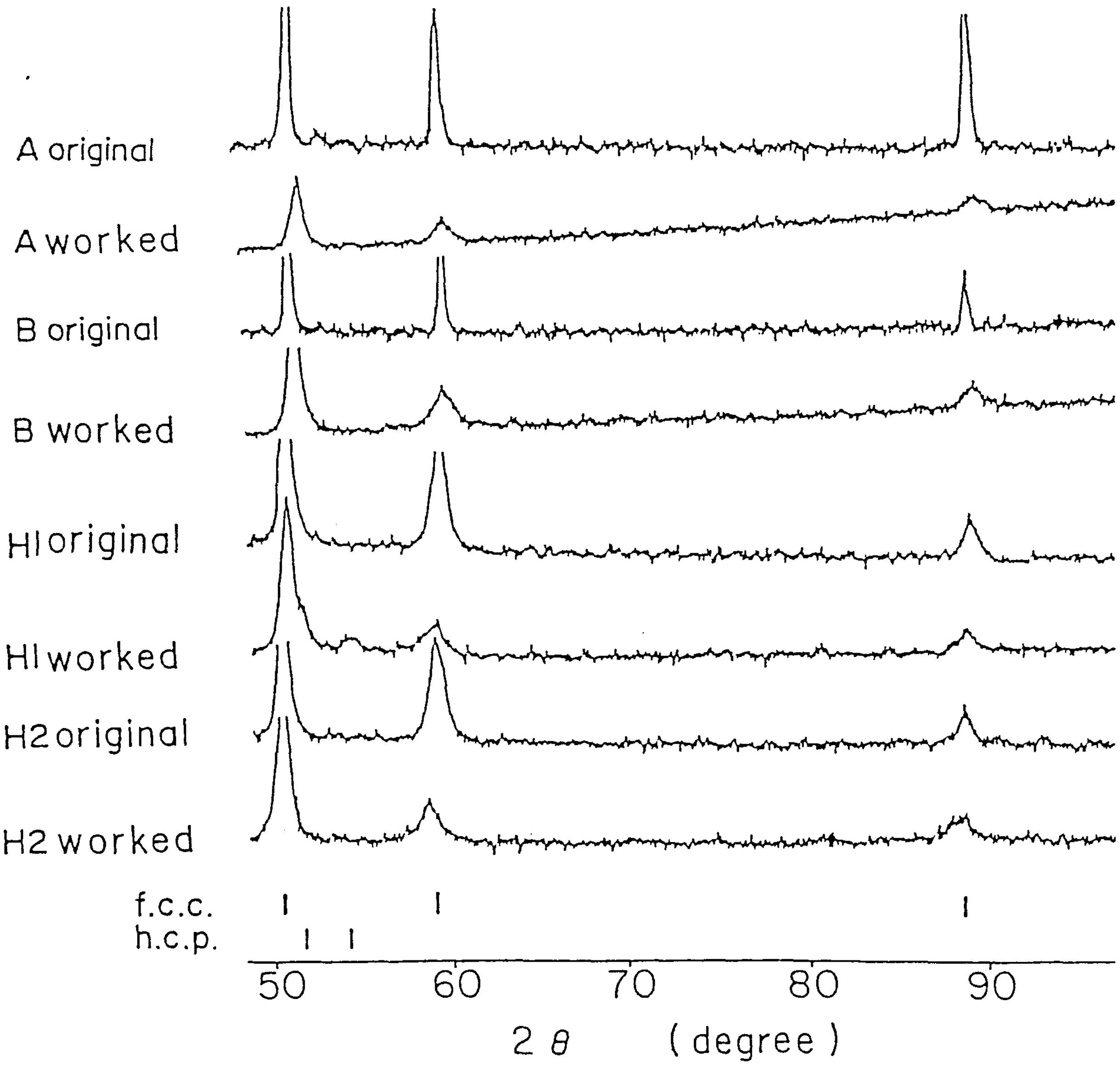

Fig. 3.2-7. X-ray diffraction patterns of high-manganese steels of A, B, H1 and H2 before and after working measured with Co-K$_\alpha$ radiation. The bars above the angle scale indicate the peak positions for the Fe-Mn-C alloy of fcc and hcp structures.

ε phase have been detected in X-ray diffraction patterns of these worked specimens, it is rather difficult to confirm that ε transformation did not occur in these specimens by working because of the limitation in the sensitivity of X-ray diffraction measurement. When ε phase is formed just near surface, the total amount of ε phase may be too small to be detected by our X-ray diffraction measurement. Since γ phase is known to be antiferromagnetic at certain lower temperatures[24,25], Mössbauer measurements below its Neel temperature could be a good method to identify the ε phase from γ phase according to their different magnetically split spectrum.

Figure 3.2-6 shows TMS spectra measured at 20 K for specimen of H3. These spectra showed large difference between before and after rolling. The differential spectrum between original and rolled specimens is shown at the bottom of Fig. 3.2-6. This differential spectrum exhibits clearly the existence of paramagnetic component at near 0 mm/s which is due to the ε phase. Other peaks are observed at both side of ε component in the differential spectrum, but their origin is not yet clear.

In contrast with the absence of the change in spectrum shape obtained at room temperature, the total area of CEMS spectra was reduced to almost half by working. In the case of XBMS, there was no appreciable reduction in total area after working. Two explanations will be considered for the reduction of the total area in CEMS spectra. One is the introduction of a plenty of dislocations and stacking faults by working. The dislocation and the stacking fault will change the local vibrational state leading to the smaller recoil-free fraction than the defect-free lattice. These defects might decrease the emission of resonance electrons by the small probability of recoil-free resonant absorption. The other is the effect of surface roughness of worked steels. CEMS has the high surface sensitivity[26)] and it may be affected by the topographical conditions of the surface. The rough surface such as shot-peened or sand-blasted specimens would scatter resonance electrons by its topographical roughness and decreases the portion of electrons which can emerge from the sample surface.

3) Stacking fault and ε martensite in γ austenite

After working, the values of electric quadrupole splitting decrease by about 3 % compared to the original values in CEMS measurements. White and Honeycombe[11)] have reported that work hardening of Hadfield steel is responsible for the combination of formation of stacking faults and the interaction of carbon atoms with the dislocations and associated stacking faults. Considering their conclusion, the reason for the decrease of electric quadrupole splitting value, which is the reduction of electric field gradient at ^{57}Fe probe atoms around carbon atom, is due to the interaction of the interstitial carbon atoms with dislocations or stacking faults introduced by working.

It is noteworthy that the hcp stacking can be obtained from the fcc lattice through the formation of (111) stacking faults[27,28)]. Figure 3.2-8 shows (111) planes of fcc structure. A displacement of C plane by $a/6[11\bar{2}]$ relative to B plane generates a stacking fault between B and C planes and then C plane becomes same stacking to A plane, that is one of the hcp stack-

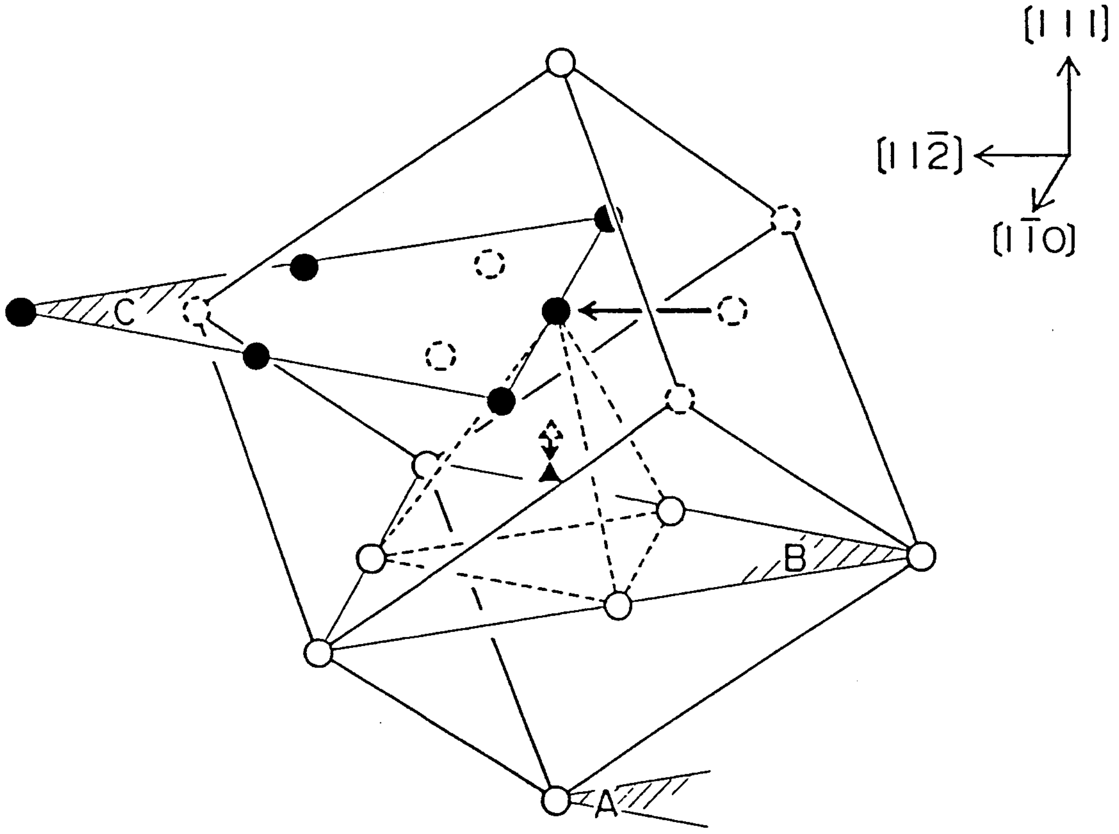

Fig. 3.2-8. Schematic view of the transformation of fcc structure to hcp structure. A shear movement between two (111) planes, B and C, by a/6[11$\bar{2}$] of fcc generates an hcp type stacking fault structure in the ABC stacking of fcc. The stacking fault changes the environment of the carbon atom marked by ▲ in the figure from the octahedral interstitial site to the tetrahedral one.

ing. If this stacking fault occurs at every two planes, ε martensite is formed by repetition of the hcp stacking.

Nishiyama et al.[13)] have found the stacking faults and thin and plane ε martensite in worked high-manganese steels from their electron microscopic observations. Huffman and Ouchi[16)] also identified the formation of ε martensite in cold-rolled Hadfield steel containing Cr by Mössbauer measurements at liquid helium temperature. Our Mössbauer results at 20 K well agree with above reports and make sure the formation of ε martensite by working.

It has been already mentioned that the surface of Hadfield steels is decarburized even before working and ε martensite is easily formed in low-carbon and high-manganese steels by working. These facts lead to the idea that the introduction of a high density of the stacking faults in the worked surface layers of Hadfield steel enhances the formation of ε martensite through the piling of these stacking faults. The influence on the environment of carbon atom at interstitial site is divided into two kinds when stacking faults are introduced in every two (111) planes. One is the carbon atom sandwiched between the two stacking fault planes and the other is out of them. In both cases, the carbon atom occupies the octahedral interstitial site in the initial fcc structure. The carbon atom between the stacking fault planes changes its environment from the octahedral to the tetrahedral interstitial site. In the case of the carbon atom out of the stacking fault planes, the octahedral interstitial site should be occupied in spite of the formation of ε martensite. Neglecting the additional lattice deformation by the interstitial carbon atom, the carbon atom sandwiched by stacking fault planes moves with the distance of $\sqrt{3}a/12$ along $[\bar{1}\bar{1}\bar{1}]$ direction. The distance and the number of the nearest iron lattice site around the carbon atom occupied at the tetrahedral interstitial site decrease from a/2 to $\sqrt{3}a/4$ and 6 to 4 comparing with the case of the octahedral interstitial site. The decrease of the electric quadrupole splitting by working in Table 3.2-2 can be explained by these changes in occupancy of the interstitial sites by carbon atoms.

Twin deformation is also possible to explain the decrease of the electric quadrupole splitting. Because a twin structure can be generated by (111) twin planes in fcc structure. Adler et al.[10)] concluded from their tensile and compressive testing that the strain hardening of Hadfield steel is owing to the formation of modified twin (they called "pseudotwinning" for the existence of the interstitial carbon atom in twin plane[29,30)]). But, in this study, the decarburization around surface of the worked specimens and the certification for the existence of ε martensite in rolled foil specimen incline the reason for work hardening around deformed surface of Hadfield steel to be the formation of ε martensite rather than twin deformation.

From above discussion, it is concluded that the work hardening of Hadfield steel around surface results from the formation of ε martensite through stacking faults introduced by working and this process is enhanced by the decarburization around surface.

3.2.4 Conclusion

Applying the measurements of CEMS, XBMS and TMS to Hadfield steels before and after working, following results have been obtained.

Any ferromagnetic peaks are not observed in all of the CEMS spectra obtained from worked specimens. This implies that α' martensite is not produced by working and it has no relation to work hardening of Hadfield steel.

The intensity of the doublet peak, which reflects the carbon concentration, does not change through working in each specimen. The carbon concentration dissolved into γ-matrix did not change through the working and it is suggested that any carbides and carbon segregations have not been formed by the working, which means that carbides and carbon segregations do not contribute to work hardening of Hadfield steel.

Decarburization at near surface of the original specimen is found from the reduction of intensity of the doublet peak in CEMS spectrum compared with that of XBMS spectrum in each specimen. So the surface layers of Hadfield steels are the low-carbon and high-manganese steel which can transform easily from γ austenite to ε martensite through the introduction of stacking faults. Also ε martensite is detected in the heavily cold-rolled foil specimen by TMS at 20 K. Therefore the work hardening of Hadfield steel around surface originates from the formation of thin ε martensites through the piling of the stacking faults introduced by working. The formation of ε martensites is most probably promoted by the decarburization around surfaces.

3.2.5 References

1. K.Hashiura, Bul. Jpn. Inst. Metals, 16(1977)681.

2. C.Ouchi, Y.Kohsaka and M.Ueda, Tetsu To Hagane, 69(1983)694.
3. J.H.Hall, Trans. AIME, 84(1929)382.
4. V.N.Krivobok, Trans. ASST, 15(1929)893.
5. R.K.Buhr, S.L.Gertsman and J.Reekie, Trans. ASM, 49(1957)706.
6. N.P.Goss, Trans. ASM, 34(1945)630.
7. D.Niconoff, Trans. ASM, 31(1943)716.
8. W.N.Roberts, Trans. Met. Soc. AIME, 230(1964)372.
9. K.S.Raghavan, A.S.Sastri and M.J.Marcinkowski, Trans. Met. Soc. AIME, 245(1969)1569.
10. P.H.Adler, G.B.Olson and W.S.Owen, Met. Trans. A, 17A(1986)1725.
11. C.H.White and R.W.K.Honeycombe, J. Iron Steel Inst., 200(1962)457.
12. Y.Imai and T.Saito, J. Jpn. Inst. Metals, 26(1962)77.
13. Z.Nishiyama, M.Oka and H.Hasegawa, J. Jpn. Inst. Metals, 28(1964)403.
14. Y.N.Dastur and W.C.Leslie, Met. Trans. A, 12A(1981)749 ;B.K.Zuidema, D.K.Subramanyan and W.C.Leslie, ibid., 19A(1988)2269.
15. O.Saeki, H.Takada, M.Sudo and T.Ohki, Tetsu To Hagane, 67(1981)A93.
16. G.P.Huffman and C.Ouchi, "Industrial Appl. of the Mossbauer Effect", Ed by G.J.Long and J.G.Stevens, Plenum, New York, (1986), p.171.
17. S.A.Sastri and R.Ray, Met. Trans., 5(1974)1501.
18. S.Nasu, H.Tanimoto and F.E.Fujita, to be submitted.

19. S.Nasu, U.Gonser, A.Blasius and F.E.Fujita, J. de Phys., C2(1979)619.

20. H.Tanimoto and S.Nasu, to be submitted.

    It should be noted that the saturation effects in XBMS is rather large and the spectral area of the doublet peak in Fig. 3.2-4 shows about 30 % larger than the true areal ratio even under the non-overlapping approximation.

21. A.J.Sedriks and T.O.Mulhearn, J. Iron Steel Inst., 202(1964)907.

22. S.Nasu, H.Tanimoto and F.E.Fujita, to be published.

23. Y.Imai and T.Saito, J. Jpn. Inst. Metals, 26(1962)283.

24. C.Kimball, W.D.Gerber and A.Arrott, J. Appl. Phys., 34(1963)1046.

25. Y.Endou and Y.Ishikawa, J. Phys. Soc. Jpn., 30(1971)1614.

26. M.Ismal and D.Liljequist, Hyp. Int., 29(1986)1509.

27. Z.Nishiyama, "Martensitic Transformation (Fundamentals)", Ed by S.Meshizumi, Maruzen, Tokyo, (1971), P.36.

28. Z.Nishiyama and K.Shimizu, Bul. Jpn. Inst. Metals, 2(1963)153.

29. F.Laves, Naturwissenschaften, 39(1952)546.

30. J.W.Cahn, Acta. Met., 25(1977)1021.

3.3 Al_2O_3 layers on Fe foil

3.3.1 Al_2O_3 deposition on Fe foil

Chemical vapor deposition (CVD) technique is widely used to construct the coating layers on the substrate materials$^{1)}$. CVD utilizes the thermal decomposition of materials at high temperatures. For example, the thermal decomposition of $Al(OH)_3$ is described as the following reaction,

$$2Al(OH)_3 \rightarrow Al_2O_3 + 3H_2O.$$

In this case, Al_2O_3 is deposited on the substrate. Other depositions of SiO_2, GaAs, SiC, etc. are performed on the semiconductor materials.

In this section, Al_2O_3 layers were deposited on α-Fe substrates by CVD and the interface between the Al_2O_3 layer and α-Fe substrate was investigated by CEMS. The effect of the annealing on the interface was also studied.

3.3.2 Sample preparation and experimental procedure

Commercially used 20 μm α-Fe foils (99.9 % up) were the substrates of the depositions. These foils were cleaned up by the ultrasonic cleaning with acetone. Al_2O_3 layers of 10, 20, 30, 50 and 60 nm were deposited on these foils by CVD technique. The deposited foils with 10 and 50 nm of Al_2O_3 layers were annealed in high vacuum for 5 hrs at 873, 1073 and 1273 K. These preparations were made at Manufacturing Development Laboratory, Mitsubishi Electric Corporation, Amagasaki.

These foils were observed by ^{57}Fe CEMS at room temperature using the newly developed electron counter. All CEMS spectra were recorded by the combination of a velocity transducer and a multichannel analyzer operated in time mode. ^{57}Co in Rh was used for Mössbauer γ-ray source and velocity scale was calibrated by using the spectrum obtained from α-Fe at room temperature. The acquired spectra were analyzed by the least-square-fit assuming the superposition of Lorentzian functions (thin foil approximation). The details of ^{57}Fe CEMS measurements were same as those of the former sections.

3.3.3 Results and discussion

1) As deposited specimens

Figure 3.3-1 shows the ^{57}Fe CEMS spectra of the Fe foils covered with the various thickness of Al_2O_3 layers deposited by CVD technique. The CEMS spectrum of the original α-Fe foil is also shown in Fig. 3.3-1. The small singlet peak was observed at the velocity around 0 mm/s in the spectrum obtained from the original α-Fe foil. This peak would be due to the oxide at the surface of the α-Fe foil. Only one 6-line pattern rising from the α-Fe substrate was observed in the CEMS spectra obtained from the Al_2O_3 deposited specimens. These spectra are almost same to each other in spite of the change in thickness of coated Al_2O_3 layers. However, the intensities of the second and fifth peaks in the 6-line pattern slightly increase with the increase of the thickness of Al_2O_3 layers.

The intensity ratio for each subpeak in the 6-lines depends on the direction of the magnetic moments of Fe atoms to γ-ray. When θ is put as the angle between the magnetic moment and γ-ray,

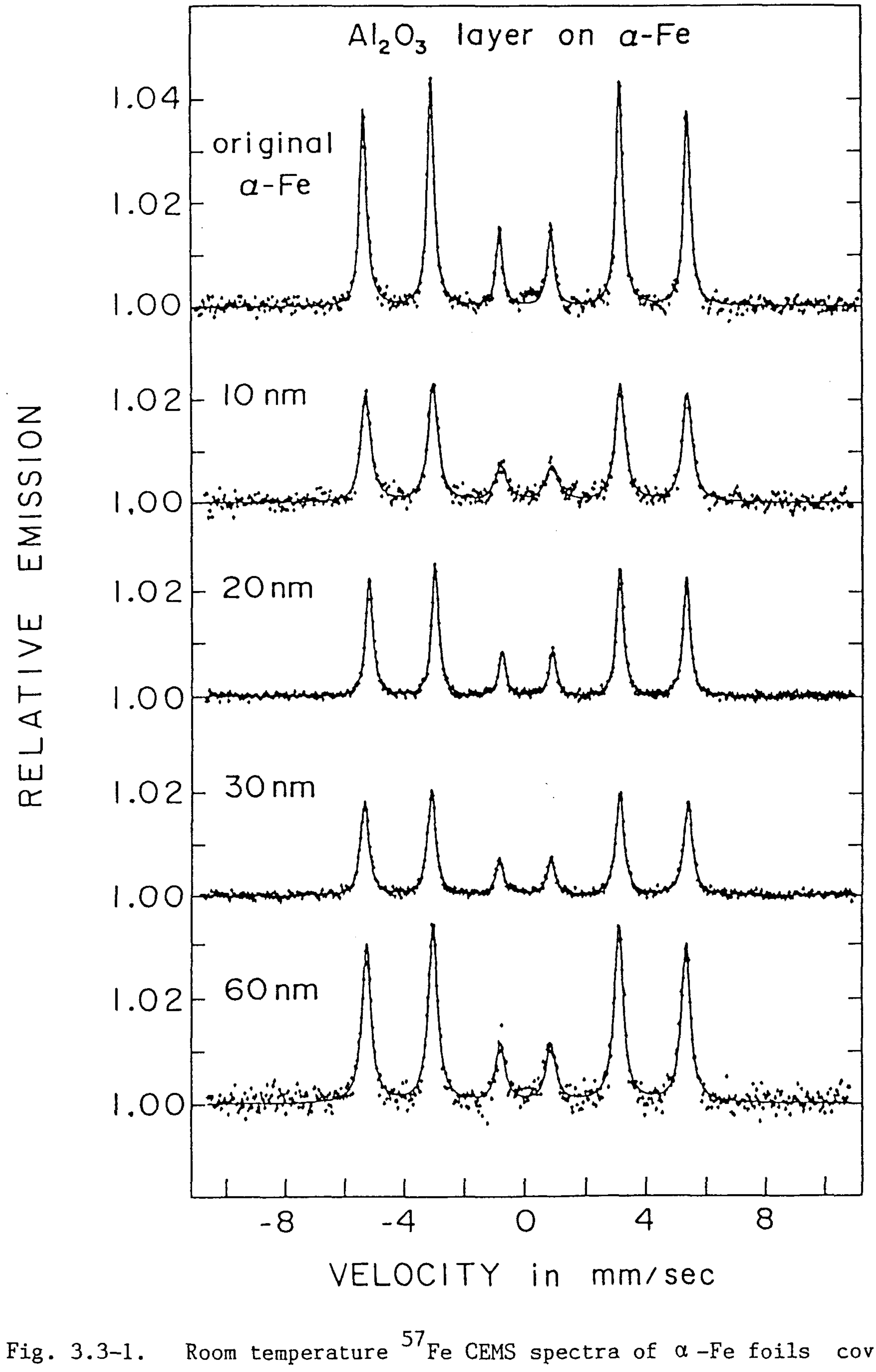

Fig. 3.3-1. Room temperature ^{57}Fe CEMS spectra of α-Fe foils covered with the various thickness of Al_2O_3 layers deposited by CVD. Only α-Fe component was observed. Velocity scale is relative to α-Fe at room temperature.

Table 3.3-1. Intensity ratio of I_2/I_1, where I_1 is the first peak intensity and I_2 is the second peak intensity of the 6-line spectra in Fig. 3.3-1, respectively.

Thickness(nm)	Original	10	20	30	60
I_2/I_1	1.14(2)	1.09(2)	1.10(2)	1.09(2)	1.11(2)

the intensities of the subpeaks in a 6-line peak (I_1, I_2, ..., I_6) are described by the following relation[2].

$$I_1:I_2:I_3:I_4:I_5:I_6 = 3:x:1:1:x:3 \qquad x=4\sin^2\theta/(1+\cos^2\theta)$$

In the case of $\theta = 90°$, the ratio becomes 3:4:1:1:4:3. The intensity ratio of the 6-line peak in CEMS spectra obtained from the original Fe foil is about 1:1.14:0.39:0.39:1.14:1. The direction of γ-ray is perpendicular to the surface of the Fe foil so that the direction of the magnetic moments of Fe atoms at the surface of the original α-Fe foil are almost parallel to the surface.

In general, the magnetic moments of Fe atoms at the surface tend to be parallel to the surface in order to lower the magnetic anisotropy energy by the formation of the closed circuit of spins, namely closure domains[3]. The figure at the left hand side in Fig. 3.3-2 shows the magnetic domain structure around the surface of α-Fe.

CEMS has the small detectable range about 10 nm from the surface according to the small straggling range of the electron in solids. With the increase of the Al_2O_3 thickness, the detectable range of CEMS shifts to the shallower part of the α-Fe substrate than the original Fe foil, where the nearly all magnetic moments of Fe atoms are parallel to the surface (the figure at the right hand side in Fig. 3.3-3). The increase of the second and fifth peak intensities with the increase of the Al_2O_3 thickness would be explained by the shift of the detectable range of CEMS to the shallower region of the α-Fe substrate with the Al_2O_3 thickness.

However, the second or fifth peak intensity is largest when

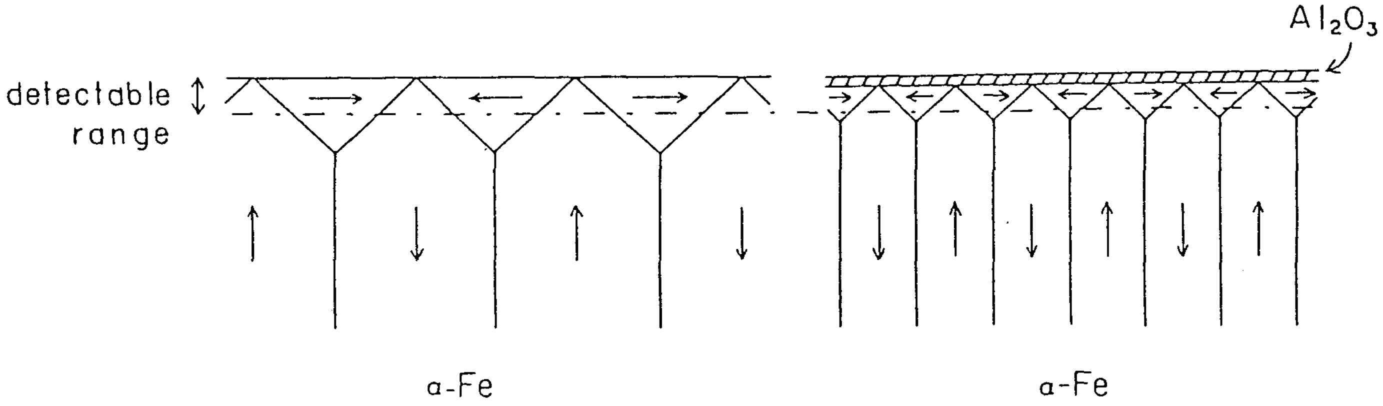

Fig. 3.3-2. Closure domains around the surface of α -Fe[3)] and fragmentation of the closure domains of α -Fe by the deposition of Al_2O_3 layer. Detectable range in the figure corresponds to the area where is effectively measured by CEMS.

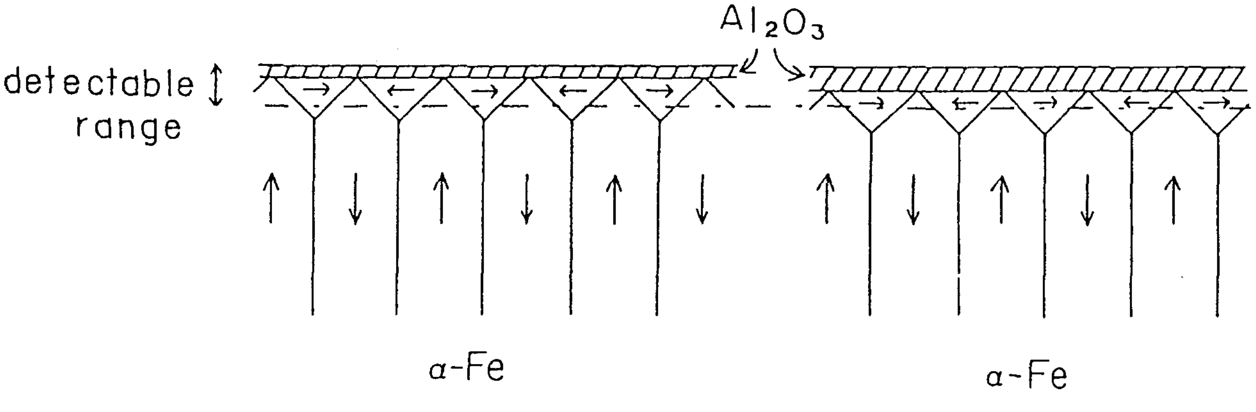

Fig. 3.3-3. The decrease of the range of α -Fe detected by CEMS with the increase of the thickness of Al_2O_3 layer.

the Fe foil is not covered with the Al_2O_3 layers, that is the original Fe foil. This confliction can be interpreted by the smaller magnetic domain structure of α-Fe at the interface to the Al_2O_3 layer than the original Fe foil. The smaller domain size exists at the surface, the larger volume fraction of the domains where the magnetic moments are perpendicular to the surface becomes to be detectable in CEMS (Fig. 3.3-2). The Al_2O_3 deposition on the Fe foil would make the magnetic domain structure of α-Fe around the interface smaller than the original Fe foil.

2) Effect of annealing

Figure 3.3-4 shows the ^{57}Fe CEMS spectra of the Fe foils coated with 10 nm of Al_2O_3 layers after annealing for 5 hrs at 873, 1073 and 1273 K. The spectrum of the as deposited specimen is also shown in Fig. 3.3-4. In the CEMS spectra obtained from the specimens after annealing at each temperature, a weak paramagnetic singlet peak was observed additionally to the ferromagnetic 6-line pattern of the α-Fe substrate. The areal contribution of this component increased from 5 to 11 % with the increase of the annealing temperature from 873 to 1073 K. But it decreased to 5 % as rising the annealing temperature from 1073 to 1273 K. The isomer shift values of these singlet peaks are about 0.25 mm/s and they are close to the value of Fe^{3+} ionic state4).

Figure 3.3-5 shows CEMS spectra of the Fe foils with 50 nm of Al_2O_3 layers annealed for 5 hrs at 873, 1073 and 1273 K and the as deposited Fe foil. An additional small singlet peak was observed at the velocity of around 0 mm/s in the CEMS spectrum

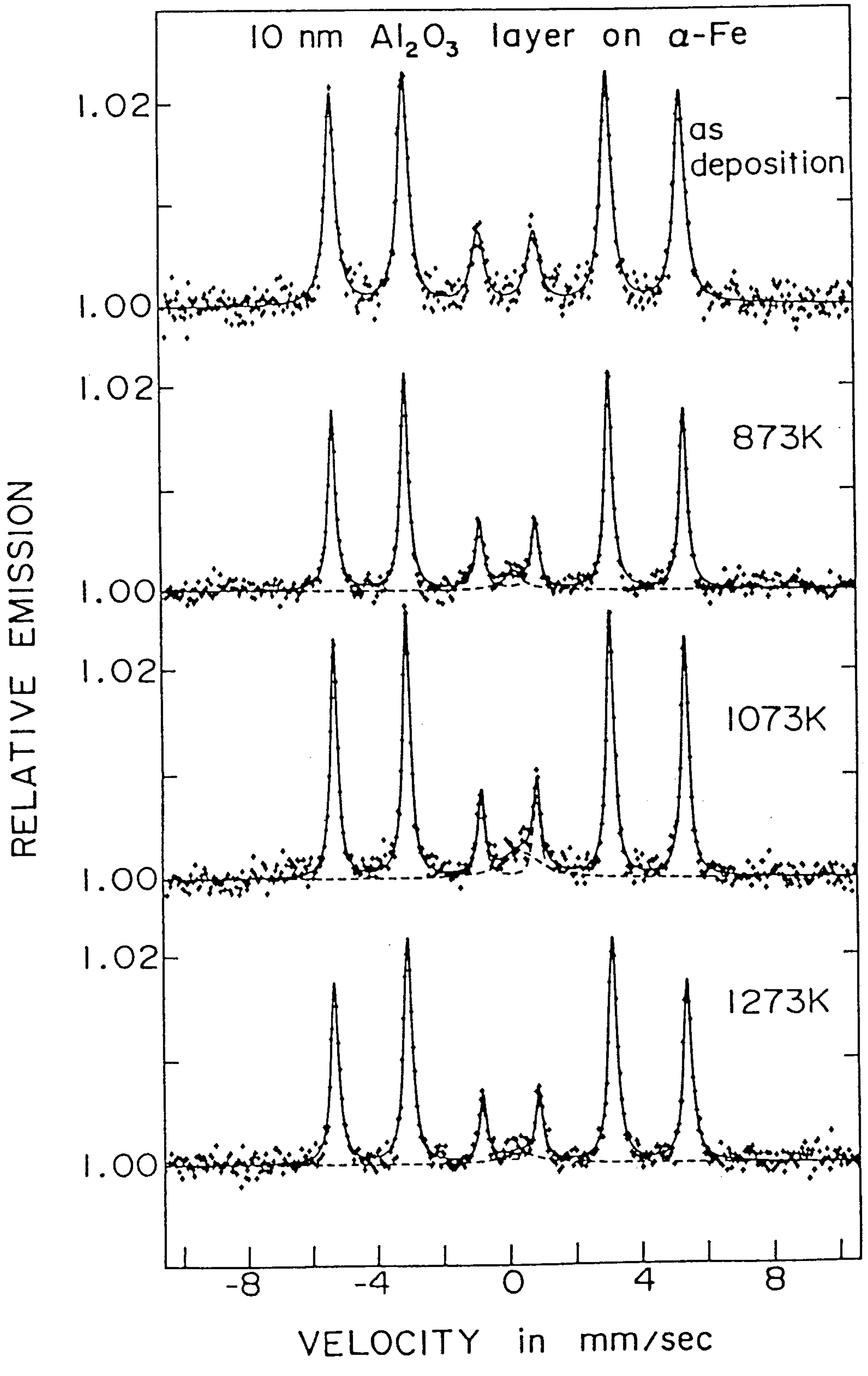

Fig. 3.3-4. ^{57}Fe CEMS spectra of α-Fe foils covered with 10 nm of the Al_2O_3 layers after annealing for 5 hrs at various temperatures. Additional paramagnetic components to the α-Fe component from the substrate were observed around the velocity of 0 mm/s. The CEMS measurements were performed at room temperature. Velocity scale is relative to α-Fe at room temperature.

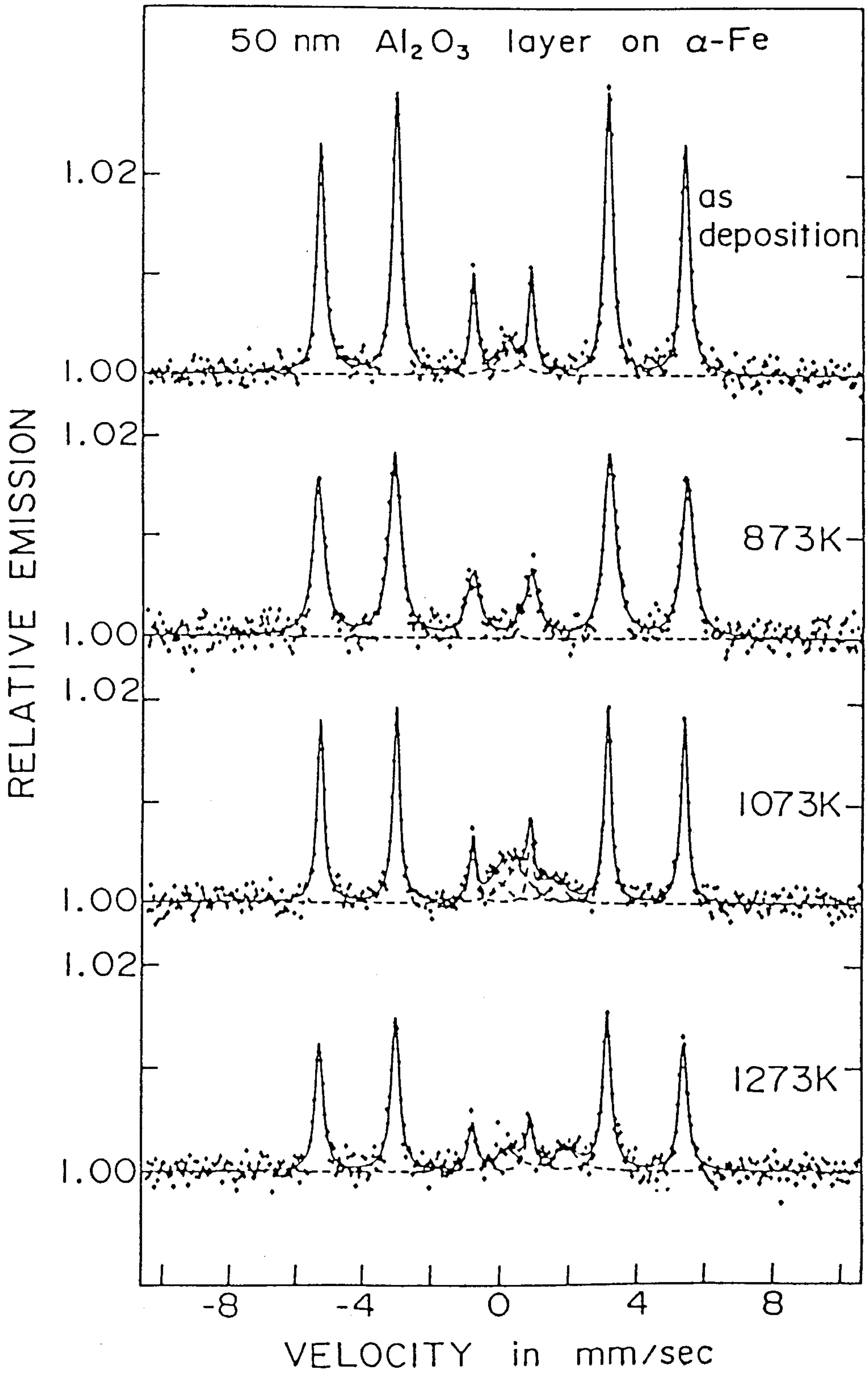

Fig. 3.3-5. ^{57}Fe CEMS spectra of α-Fe foils covered with 50 nm of the Al_2O_3 layers after annealing for 5 hrs at various temperatures. Additional components to the α-Fe component from the substrate were observed around the velocity of 0 mm/s. The CEMS measurements were performed at room temperature. Velocity scale is relative to α-Fe at room temperature.

obtained from the as deposited specimen. The similar peak was not detected in the spectra of other as deposited specimens. It is considered that the surface of the α-Fe substrate had already oxidized before the Al_2O_3 deposition in the case of the as deposited specimen in Fig. 3.3-5.

The CEMS spectrum obtained from the specimen annealed at 873 K in Fig. 3.3-5 can be analyzed by the 6-line pattern corresponding to the α-Fe substrate and the singlet peak. However the areal contribution of the singlet peak is almost zero. The CEMS spectrum of the specimen annealed at 1073 K in Fig. 3.3-5, a doublet peak newly appeared near the singlet peak around the velocity of 0 mm/s. The intensity of the singlet peak increased with rising the annealing temperature from 873 to 1073 K. Only doublet peak was observed additionally to the 6-line pattern of the α-Fe substrate in the CEMS spectrum obtained from the specimen annealed at 1273 K. The isomer shift values of the singlet peaks are around +0.20 mm/s. These values are close to the value of Fe^{3+} ions. The values of the isomer shift and the electric quadrupole splitting for the doublet peaks are about 1.0 and 1.7 mm/s, respectively. These values are close to the values of Fe^{2+} ions4,5).

In the case of the Al_2O_3 deposition with 50 nm thickness, Fe^{3+} and Fe^{2+} ionic states were formed by annealing and their formations depend on the annealing temperature. Annealing at 873 K, only Fe^{3+} ionic state was formed at the interface between the Al_2O_3 layer and the α-Fe substrate. However, only Fe^{2+} ionic state was formed after annealing at 1273 K. This difference of the oxidized state of Fe atoms by the annealing temperature has been discussed using a thermal equilibrium phase diagram of Fe-O system.

Figure 3.3-6 shows the phase diagram of Fe-O system. By the annealing at 1273 K, α-Fe of the substrate is transformed to γ-Fe. The formation of Fe^{3+} ionic state may have some relations to the structural transformation of the substrate Fe metal. If Fe atoms in the γ-Fe substrate cannot get into the Al_2O_3 layers, O atoms which can contribute to the oxidation of Fe atoms are placed only at the interface. This condition would cause Fe^{2+} ionic state because of the small amount of O atoms contributing to the oxidation. Annealing at 1273 K, Fe atoms would not mix into the Al_2O_3 layers and Fe^{2+} ionic state was generated by the annealing.

If Fe atoms in α-Fe can get into the Al_2O_3 layers, the larger amount of O atoms than the case of the α-Fe substrate contribute to the oxidization of Fe atoms, which leads to Fe^{3+} ionic state. By annealing at 873 K, Fe atoms would mix into the Al_2O_3 layers and Fe atoms were oxidized to Fe^{3+} ionic state. By annealing at 1073 K, both of Fe^{2+} and Fe^{3+} ionic states were formed at the interface for the intermediate condition between the annealing at 873 and 1273 K.

The formation of these two ionic states also depends on the thickness of the Al_2O_3 layers. In the case of the Al_2O_3 deposition of 50 nm, Fe^{2+} and Fe^{3+} ionic states were generated by the annealing and their amounts were changed by the annealing temperature. Only Fe^{3+} ionic state was formed by the annealing at 873 K and only Fe^{2+} state was formed by the annealing at 1273 K. On the other hand, in the case of the deposition of 10 nm, only Fe^{3+}

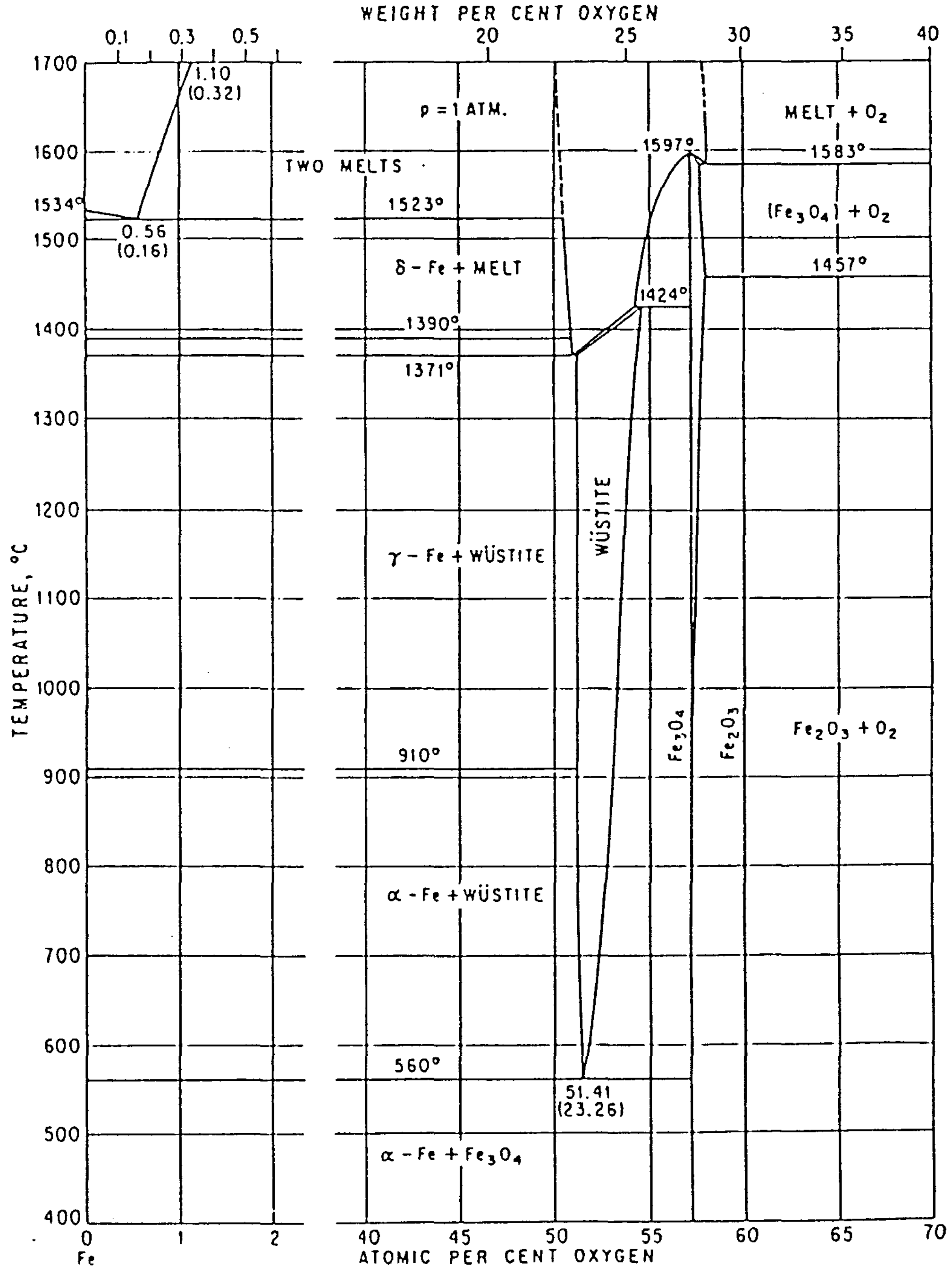

Fig. 3.3-6. Phase diagram of Fe-O system6).

ionic state was generated by the annealing at any temperature. But its amount decreased with the increase of the annealing temperature from 1073 to 1273 K. The inherent property of the thin deposited layers might suppress the formation of Fe^{2+} ionic state during the annealing. The further experiments are necessary to clarify the relation between the thickness of the Al_2O_3 layers and the oxidation behavior of the Fe atoms at the interface.

3.3.4 Conclusion

The interface between the deposited Al_2O_3 layers and α-Fe substrates was studied by CEMS and following results are obtained.

The interface between an α-Fe foil and deposited Al_2O_3 layers is clear and Al_2O_3 and Fe atoms do not mix with each other. The size of the magnetic domain of α-Fe substrate becomes to be small by the Al_2O_3 deposition.

After the annealing of the deposited foils having 50 nm Al_2O_3 layer, Fe^{2+} and Fe^{3+} ionic states were observed at the interface of the deposition. But only Fe^{2+} state was formed by the annealing at 1273 K and only Fe^{3+} state was formed by the annealing at 873 K. The difference of the oxidative behavior between the annealing at 873 and 1273 K may be explained by the structural transformation of the substrate Fe metal.

In the case of the Al_2O_3 deposition of 10 nm, only Fe^{3+} ionic state was observed by the annealing at any temperature. The mechanism of this behavior has not been clear yet.

3.3.5 References

1. A.Kinbara and H.Fujiwara, "Thin Films", Shokabo, Tokyo, (1979), p.26.
; H.Watanabe, "Saishin Kagoubutu Handoutai Handbook", Ed. by T.Ikoma, Science Forum, Tokyo, (1982), p.121.
2. N.N.Greenwood and T.C.Gibb, "Mössbauer Spectroscopy", Chapman and Hall, London, (1971), p.66.
3. S.Chikazumi, "Physics of Ferromagnetism, Vol.II", Shokabo, Tokyo, (1984), p.203.
4. R.Ingalls, F.van der Woude and G.A.Sawatzky, "Mössbauer Isomer Shifts", Ed. by G.K.Shenoy and F.E.Wagner, North-Holland, Amsterdam, (1978), p.363.
5. E.Murad and J.H.Johnston, "Mössbauer Spectroscopy Applied to Inorganic Chemistry Vol.2", Ed. by G.J.Long, Plenum, New York, (1987), p.507.
6. M.Hansen, "Constitution of Binary Alloys", McGraw-Hill, New York, (1958).

3.4 Nd-Fe-B permanent magnet (NEOMAX)

3.4.1 Nd-Fe-B ($Nd_2Fe_{14}B$) permanent magnet

Nd-Fe-B permanent magnet (NEOMAX) has the excellent maximum energy products over 290 kJ/m^3 compared to other permanent magnets (Fig. 3.4-1). This magnet was invented by Sagawa et al.[1)] in 1983. The lower production cost of this magnet than other rare-earth cobalt permanent magnets such as $SmCo_5$ and Sm_2Co_{17} is also one of the benefit of this magnet.

The typical composition of the Nd-Fe-B permanent magnet is around Nd:Fe:B = 15:77:8 in atomic ratio. The main component of the Nd-Fe-B permanent magnet is a $Nd_2Fe_{14}B$ ternary intermetallic compound, whose structure is tetragonal as shown in Fig. 3.4-2[2,3)].

The master alloy of this magnet is prepared by using a high frequency induction furnace. The master alloy is ground to the powder of about 3 μm in diameter. This powder is press-formed under the magnetic field to achieve the good alignment of the magnetic domains. The formed plate is sintered at 1370 K in Ar gas atmosphere. After the polishing of the surface, the heat-treatment for 1 hr at about 1173 K is performed and subsequently a quenching treatment is carried out.

After these heat-treatments, the magnetic properties at the surface of the Nd-Fe-B permanent magnet quite differ from that of the inner parts. It is reported that the coercive force of Nd-Fe-B magnet around the surface is considerably smaller than that of the inner parts[4,5)].

In this section, CEMS was applied to study the magnetic

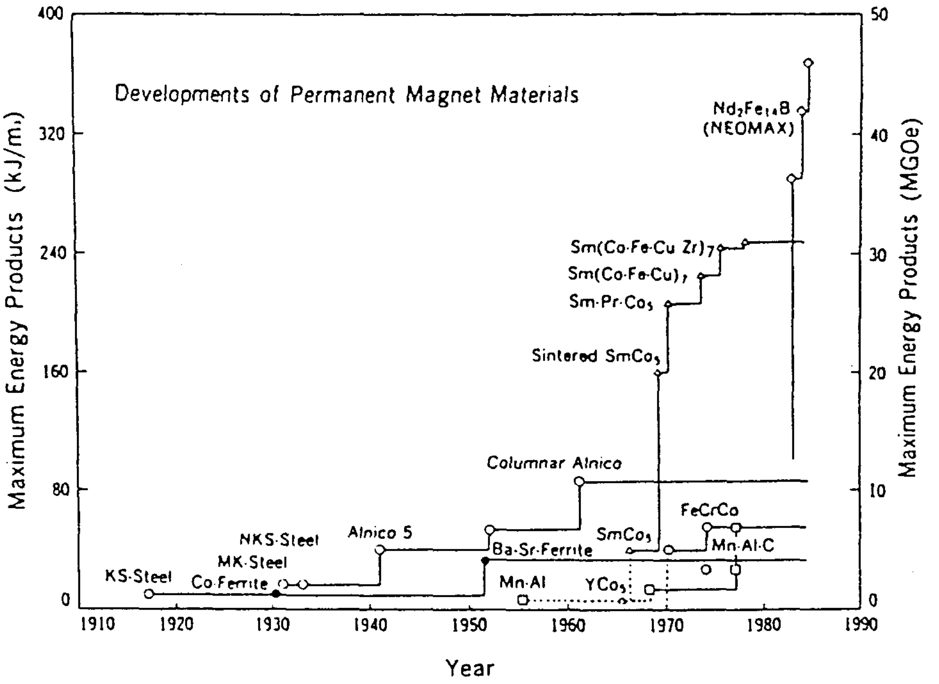

Fig. 3.4-1. Development of the permanent magnet material[2)]

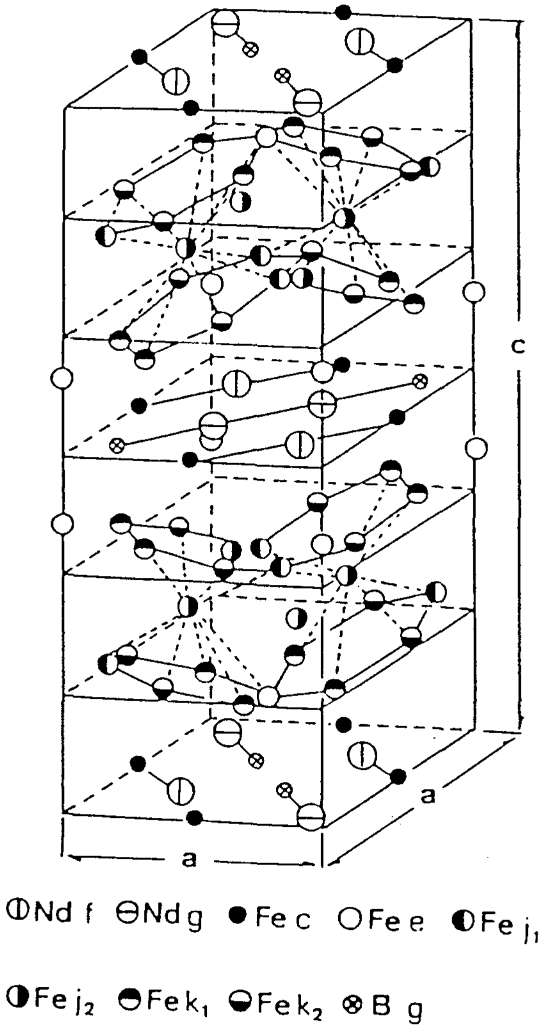

Fig. 3.4-2. Structure of $Nd_2Fe_{14}B$ ternary intermetallic compound[2)].

properties at the surface of Nd-Fe-B permanent magnet in order to clarify the reason for the decrease of the coercive force around surface.

3.4.2 Experimental procedure

The plates of $Nd_2Fe_{14}B$ alloys were supplied from Sumitomo Special Metals Co., Ltd, Mishimagun, Osaka. The dimensions of the plates were about 15x15x2 mm^3. Two kinds of the specimens were prepared having different alignments of the c-axis of the crystal. One specimen has a perpendicular alignment of the c-axis to the surface and the other specimen has a parallel alignment of the c-axis to the surface. At room temperature, the direction of the magnetic moments of Fe atoms is parallel to the c-axis6). For these two specimens having different c-axis alignments, further different kinds of preparations were performed. The surface of one plate was polished and the other was heat-treated after the polishing process. The heat-treatment was performed for 1 hr at 1173 K in vacuum of $1x10^{-6}$ Torr and cooled down to room temperature at a cooling rate about 100 K/min.

^{57}Fe CEMS measurements were performed for these plates at room temperature using the newly developed electron counter. The direction of γ-ray was always normal to the surface of the specimens in all of the ^{57}Fe CEMS measurements. The powder specimen of the $Nd_2Fe_{14}B$ permanent magnet was also measured by ^{57}Fe TMS at room temperature. All of the Mössbauer spectra were recorded by the combination of a multichannel analyzer operated in time mode and a velocity transducer. ^{57}Co in Rh was used for the Mössbauer γ-ray source and velocity scale was calibrated using the spectrum obtained from α-Fe at room temperature. The obtained spectra were analyzed by the least-square-fit assuming the superposition of the Lorentzian functions (thin foil approximation). The details of ^{57}Fe Mössbauer measurements are same as those described in the former sections.

3.4.3 Results and discussion

1) As polished specimens

Figure 3.4-3 shows the ^{57}Fe CEMS spectra of as polished specimens whose alignments of c-axis are perpendicular (a) and parallel (b) to the surface, respectively. Figure 3.4-4 shows the TMS spectrum of the powder specimen of $Nd_2Fe_{14}B$ magnet. The TMS spectrum is well analyzed by the six kinds of 6-line patterns[6,7]. In this analysis, the line width was restricted in the same value and all 6-line patterns had the same intensity ratio.

The CEMS spectra in Fig. 3.4-3 are similar to the TMS spectrum in Fig.3.4-4. These CEMS spectra can be well reproduced by the six 6-line patterns having identical values of the isomer shift, electric quadrupole splitting and hyperfine field to those in the TMS spectrum of Fig. 3.4-4, but having the different intensity ratio of the 6-line patterns. The areal contribution of each 6-line pattern in the both CEMS spectra is almost same to that of the TMS spectrum. These suggest that the chemical state at the surface of the $Nd_2Fe_{14}B$ compound is not different from that of the bulk after polishing the surface.

However, the intensity ratio of the 6-line pattern in the

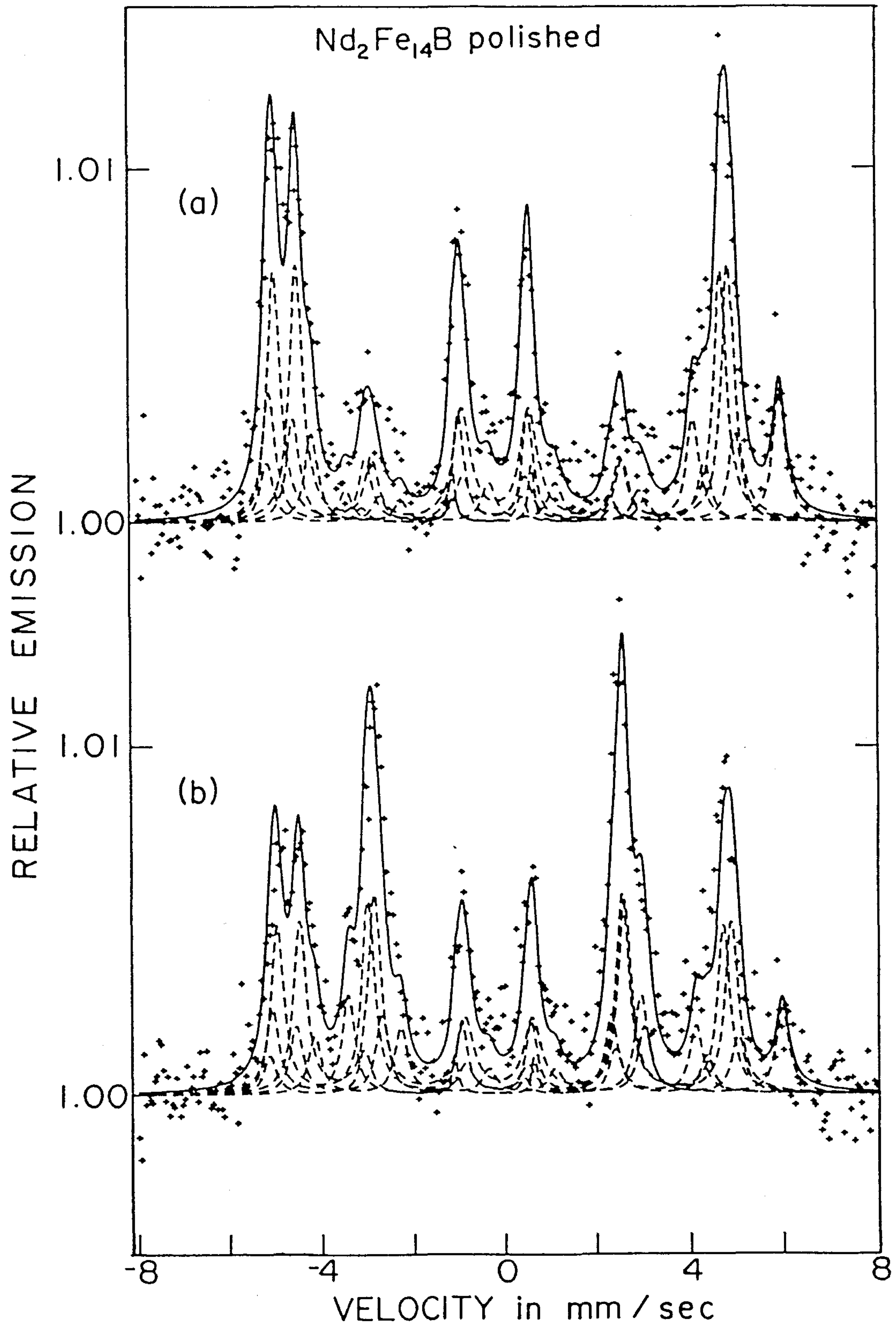

Fig. 3.4-3. ^{57}Fe CEMS spectra of $Nd_2Fe_{14}B$ compounds just after polishing the surface measured at room temperature. The alignment of c-axis is perpendicular (a) and parallel (b) to the surface. Velocity scale is relative to α-Fe at room temperature.

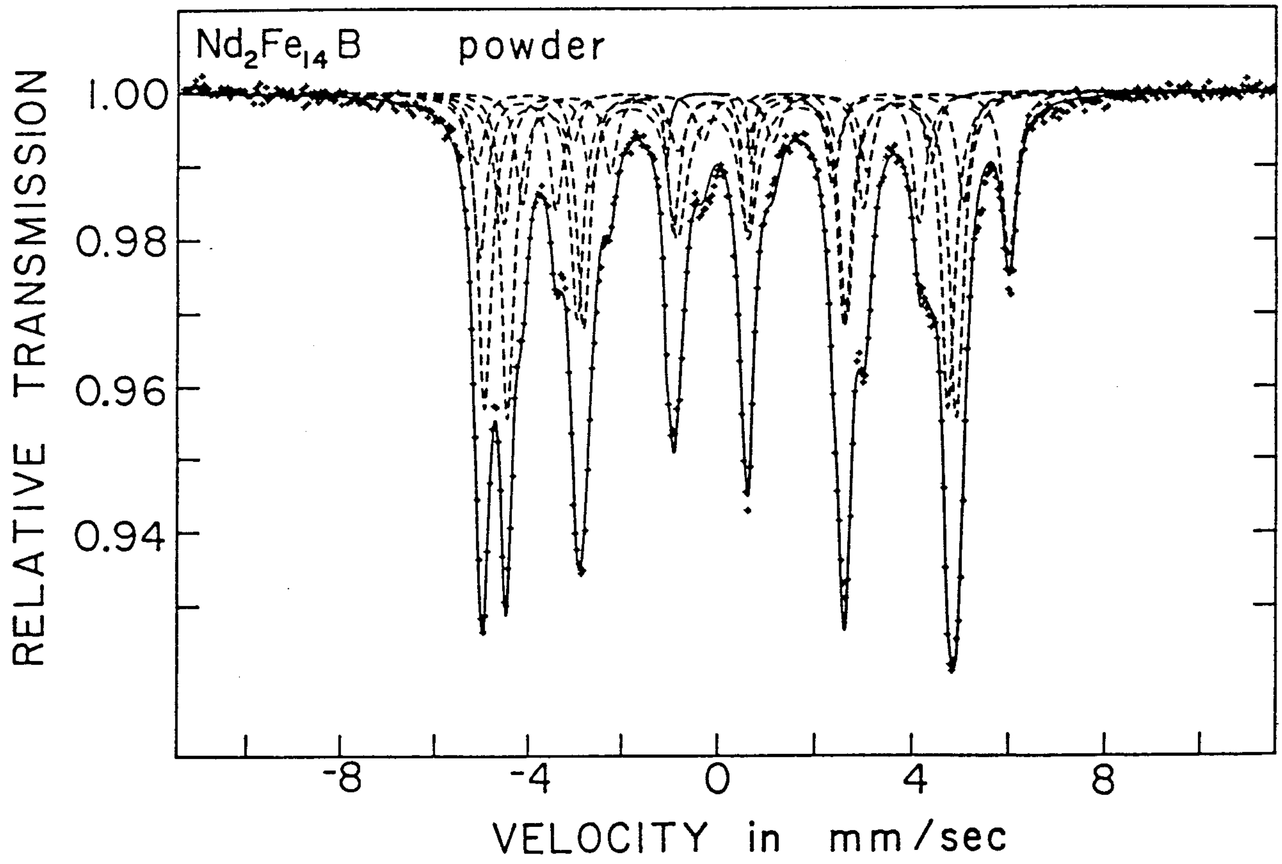

Fig. 3.4-4. ^{57}Fe TMS spectrum of the powder of the $Nd_2Fe_{14}B$ compound measured at room temperature. The spectrum was well reproduced by six kinds of 6-line patterns shown by broken lines. Velocity scale is relative to α-Fe at room temperature.

CEMS spectra is quite different from that of the corresponding pattern in the TMS spectrum. It is caused from the different alignment of the c-axis between the platelet specimens for CEMS measurement and the powder specimen for TMS.

The intensity ratio of a 6-line pattern depends on the angle between the direction of the magnetic moments of the Fe atoms and γ-ray. When the magnetic moments of Fe atoms are parallel to the direction of γ-ray, the intensity ratio of the 6-line pattern becomes 3:0:1:1:0:3. When the magnetic moments of Fe atoms are perpendicular to the direction of γ-ray, the intensity ratio becomes 3:4:1:1:4:3. When the magnetic moments of Fe atoms are random to the direction of γ-ray, the intensity ratio becomes 3:2:1:1:2:3 8), that is close to the case of the TMS spectrum obtained from the powder specimen in Fig. 3.4-4.

The intensity ratio of the 6-line pattern in the spectrum (a) of Fig. 3.4-3 is close to 3:0:1:1:0:3. It suggests that the most of magnetic moments of Fe atoms are perpendicular to the surface because the incident direction of γ-ray is normal to the surface of the specimen. On the other hand, the intensity ratio of the 6-line pattern in the spectrum (b) in Fig. 3.4-3 is close to 3:4:1:1:4:3. It suggests that most of the magnetic moments of Fe atoms are parallel to the surface. Since the magnetic moment of Fe atom in the Nd-Fe-B magnet at room temperature is parallel to the c-axis, the c-axis around the surface of the specimen is perpendicular to the surface for the case of the spectrum (a) and parallel for the spectrum (b). So the alignment of the magnetic moments of Fe atoms around the surface is same as that of the inner bulk even after polishing the surface, namely the magnetic structure around surface is same as that of the inner part of the bulk.

2) As heat-treated specimens

Figure 3.4-5 shows the ^{57}Fe CEMS spectra obtained from the heat-treated specimens whose alignments of the c-axis at the press-forming process are perpendicular (a) and parallel (b) to the surface.

Comparing with the TMS spectrum observed from the powder specimen in Fig. 3.4-4, only one 6-line pattern is observed in each CEMS spectrum in Fig.3.4-5. The isomer shift and hyperfine field values of this 6-line pattern are 0 mm/s and 330 kG, respectively. Those values are agreed well with the values of α-Fe. This means that the surface layers of Nd-Fe-B permanent magnet consist of only α-Fe after the heat-treatment. The other elements of Nd and B would be decomposed completely from the $Nd_2Fe_{14}B$ compound at the surface layers and form their own oxide phases during the heat-treatment.

The intensity ratio of the 6-line pattern of the spectrum (a) was determined to be 1:0.86:0.35:0.36:0.82:1.00 by the fitting procedure using one sextet peak. On the other hand, the intensity ratio of the 6-line pattern of the spectrum (b) was also determined to be 1:0.82:0.35:0.35:0.81:1.03 by the same way. These ratios are far from 3:0:1:1:0:3 or 3:4:1:1:4:3, which are the expected values from the alignments of c-axis at the press-forming process. These ratios are rather close to 3:2:1:1:2:3, which corresponds to the case of the random alignment of c-axis. So that the surface layers of $Nd_2Fe_{14}B$ com-

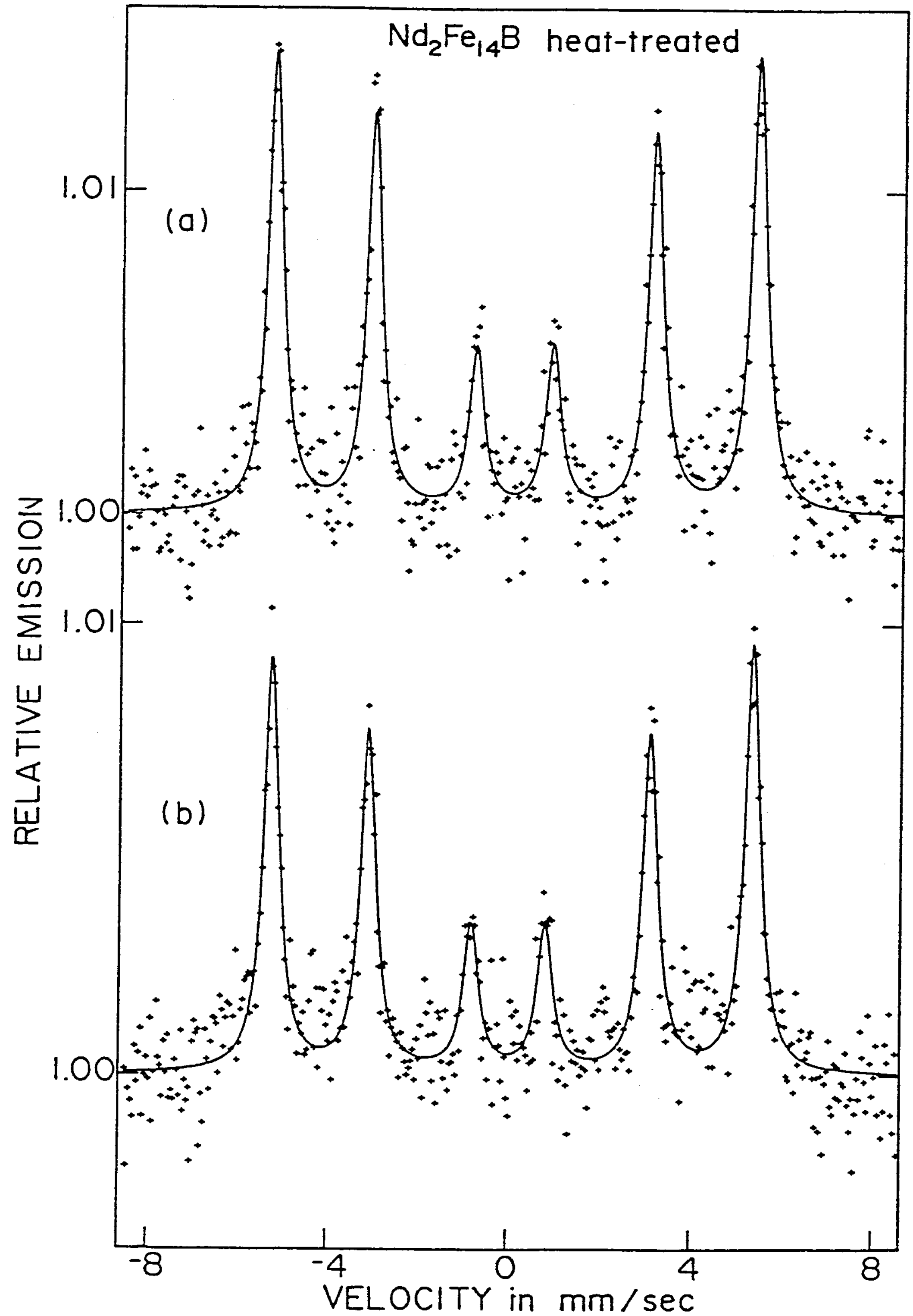

Fig. 3.4-5. ^{57}Fe CEMS spectra of heat-treated Nd-Fe-B compounds measured at room temperature. The alignment of c-axis is perpendicular (a) and parallel (b) to the surface. Only one 6-line pattern was observed in each spectrum. Velocity scale is relative to α-Fe at room temperature.

pounds after the heat-treatment would be covered with the randomly aligned small clusters of α-Fe. The thickness of the α-Fe layers will be over 100 nm, estimated from the detectable range of CEMS measurement.

The intensities of the second and fifth patterns in the spectrum (a) of Fig. 3.4-5 are slightly larger than those of the spectrum (b). At the surface layers of heat-treated specimens, the magnetic moments of Fe atoms in the specimen whose c-axis stands up to the surface are rather parallel to the surface than those whose c-axis is along to the surface. This is due to the crystal structure of the $Nd_2Fe_{14}B$ compound as discussed as follows.

The $Nd_2Fe_{14}B$ compound has the layer structure along the c-axis, constructed by the two layers of an Fe layer and a Nd-B layer containing small amount of Fe atoms (Fig. 3.4-2). At the alignment of the c-axis perpendicular to the surface, the Fe layers in $Nd_2Fe_{14}B$ are parallel to the surface and α-Fe layers will be formed at the surface by the decomposition of Nd and B atoms from the $Nd_2Fe_{14}B$ compound. The magnetic moments of Fe atoms at α-Fe layers would be parallel to the surface.

At the alignment of c-axis parallel to the surface, the Fe layers in $Nd_2Fe_{14}B$ compound are perpendicular to the surface and needle shape α-Fe clusters will be formed on the surface by the decomposition of Nd and B atoms from the compound. The magnetic moments of Fe atoms in the α-Fe needle formed at the surface would be perpendicular to the surface.

From CEMS measurements of heat-treated $Nd_2Fe_{14}B$ compounds, it is suggested that the low coercive force at the surface of

Nd-Fe-B permanent magnet is due to the decomposition of Nd and B atoms from the $Nd_2Fe_{14}B$ compound and the formation of platelet shape α-Fe and needle shape α-Fe clusters by the heat-treatment.

3.4.4 Conclusion

CEMS measurements were performed for the platelet specimens of Nd-Fe-B permanent magnets before and after the heat-treatment. Following results were obtained.

CEMS spectra obtained from the specimens without the heat-treatment could be well analyzed by the same components as those in the TMS spectrum obtained from the powder specimen. It suggests that the chemical state of $Nd_2Fe_{14}B$ compound is not different from the bulk state after the polishing of the surface. The intensity ratio of the 6-line patterns in the CEMS spectrum indicates the alignment of the c-axis at the surface of as polished specimens without any heat-treatment. The alignments of the c-axis around the surface of as polished $Nd_2Fe_{14}B$ compounds without any heat-treatment are same as those obtained at the press-forming process.

After the heat-treatment, only α-Fe component was observed in CEMS spectra. It seems that Nd and B atoms decomposed from the surface layers and only Fe atoms remained at around the surface by the heat-treatment. The surface layers of $Nd_2Fe_{14}B$ compounds are covered with α-Fe clusters after the heat-treatment.

From the above discussion, the low coercive force at the surface of Nd-Fe-B permanent magnet is due to the decomposition of Nd and B atoms from the $Nd_2Fe_{14}B$ compound during the heat-treatment. The surface of heat-treated Nd-Fe-B permanent magnets is covered with α-Fe clusters.

3.4.5 References

1. M.Sagawa, S.Fujimura, N.Togawa, H.Yamamoto and Y.Matsuura, J. Appl. Phys., 55(1984)2083.
2. M.Sagawa, J. Magn. Soc. Jpn., 9(1985)25.
3. J.F.Herbst, J.J.Croat, F.E.Pinkerton and Y.B.Yelon, Phys. Rev. B, 29(1984)4176.
4. S.Hirosawa, K.Tokuhara and M.Sagawa, J. Jpn. Appl. Phys., 26(1987)L1356.
5. D.Givord, P.Tenaund and T.Viadieu, J. Appl. Phys., 60(1986)3263.
6. H.Onodera, Y.Yamaguchi, H.Yamamoto, M.Sagawa, Y.Matsuura and H.Yamamoto, J. Magn. Magn. Mat., 46(1984)151.
7. H.Onodera, H.Yamauchi, M.Yamada, H.Yamamoto, M.Sagawa and S.Hirosawa, J. Magn. Magn. Mat., 68(1987)15.
8. N.N.Greenwood and T.C.Gibb, "Mössbauer Spectroscopy", Chapman & Hall, London, (1971), p.66.

3.5 Fe-doped Y-Ba-Cu oxide superconductor

3.5.1 Y-Ba-Cu oxide superconductor

$YBa_2Cu_3O_{7-y}$, which is so called 1-2-3 compound, has a superconducting critical temperature well above 90 K and so much efforts have been devoted to investigate the physical, structural and chemical properties of this high-T_c Y-Ba-Cu oxide[1-7]. It is now well established that the crystal structure and the superconducting transition temperature, T_c, of this compound depends on the oxygen concentration. There are two crystallographically different Cu sites as shown in Fig. 3.5-1, those are Cu1 chain site sandwiched by the two Ba layers and Cu2 planar site forming a nearly two dimensional CuO_2 sheet. When the Cu1 chain site has four oxygen planar coordination, the compound has an orthorhombic structure and shows a high-T_c superconductivity. When the Cu1 chain site has only two oxygen coordination, the compound has an tetragonal structure indicating a long-range antiferromagnetic order of CuO_2 sheets[7] and does not show any superconductivity. Oxygen arrangements around the Cu1 chain sites and the disappearance of the antiferromagnetic long-range order of CuO_2 plane are recognized as the important key to create the high-T_c superconductivity of this compound.

Oxygen concentration of this compound depends sensitively on the specimen treatments like an annealing temperature and the atmosphere. It is also well recognized that the oxygen desorption occurred easily by the low temperature annealing in vacuum[8] and this compound is not always stable during the specimen handling like a crushing from a disk shaped pellet into powder

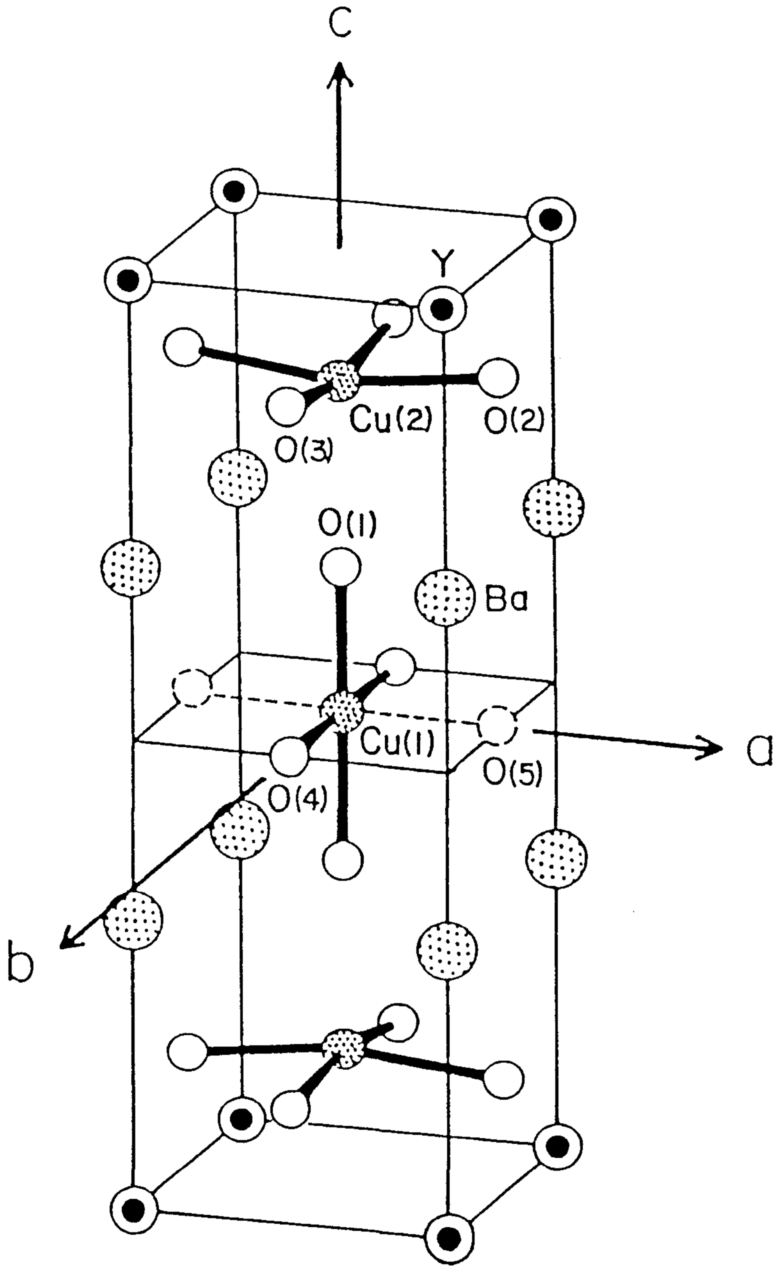

Fig. 3.5-1. Structure of $YBa_2Cu_3O_7$. Cu1 chain and Cu2 planar sites are shown as Cu(1) and Cu(2), respectively.

specimen.

Hyperfine interaction studies utilizing the ^{57}Fe Mössbauer spectroscopy have been performed by several research groups$^{9-25)}$ and reported a microscopic nature of the Fe-doped compounds. It has been generally accepted that the Fe atoms mainly occupy the Cu1 chain sites and has at least three different kinds of oxygen coordination number around them$^{8)}$.

All of the ^{57}Fe Mössbauer measurements reported previously have been performed using powder specimens under a transmission geometry and there is no reports concerning CEMS measurements of this compound using disk shaped pellet under a scattering geometry. In this section, the results from the CEMS measurements using the disk shaped 1-2-3 compounds have been described and compared with the γ-ray transmission measurements using the powder specimens which were prepared by the crushing from disk shaped pellet.

3.5.2 Sample preparation and experimental procedure

$YBa_2(Cu_{1-x}Fe_x)_3O_{7-y}$ (x = 0.04, 0.06 and 0.10) specimens were prepared by a usual solid state reaction method using Y_2O_3, $BaCO_3$, CuO and ^{57}Fe enriched Fe_2O_3. All specimens were annealed in air at high temperatures and slowly cooled down to room temperature in air. All of the specimen have a tetragonal structure and show the superconductivity whose critical temperatures, T_c, decreases as an increase of the Fe concentration. Details of the specimen preparation, the resistivity measurements and the static magnetic measurements using identical specimens have been reported by Oda et al.$^{24)}$ and Sakagami et al.$^{26)}$.

For the TMS measurements, the powder specimens were used and for the CEMS measurements the disk shaped specimens having the same Fe concentrations were used.

^{57}Fe Mössbauer measurements were performed using a combination of the transducer operated by a constant acceleration mode and a multichannel analyzer as described in the previous sections. The powder specimens were measured by TMS at various temperature. The disk shaped specimens were measured by CEMS at room temperature, utilizing the newly developed electron counter. The details of ^{57}Fe Mössbauer measurements should be referred to the former sections.

3.5.3 Experimental results and discussion

Figure 3.5-2 shows the ^{57}Fe Mössbauer spectra at room temperature obtained from $YBa_2Cu_{2.88}Fe_{0.12}O_{7-y}$ superconductor. Upper figure shows a CEMS spectrum and a TMS spectrum is shown in lower figure. These spectra are well analyzed by the superposition of three different kinds of the quadrupole-split doublets which are denoted as D-1, D-2 and D-3 as shown in Fig. 3.5-2. Isomer shift values of D-1 and D-2 are nearly 0 mm/s and of D-3 is 0.27 mm/s relative to bcc Fe at room temperature and do not show any appreciable difference between CEMS and TMS spectra. The magnitude of the quadrupole splitting are determined as 2.0 mm/s for D-1, 1.2 mm/s for D-2 and 0.5 mm/s for D-3 components, respectively, and these values do not also show any appreciable difference between CEMS and TMS spectra. It implies that the chemical states of Fe atoms at the surface are identical to the states in the bulk.

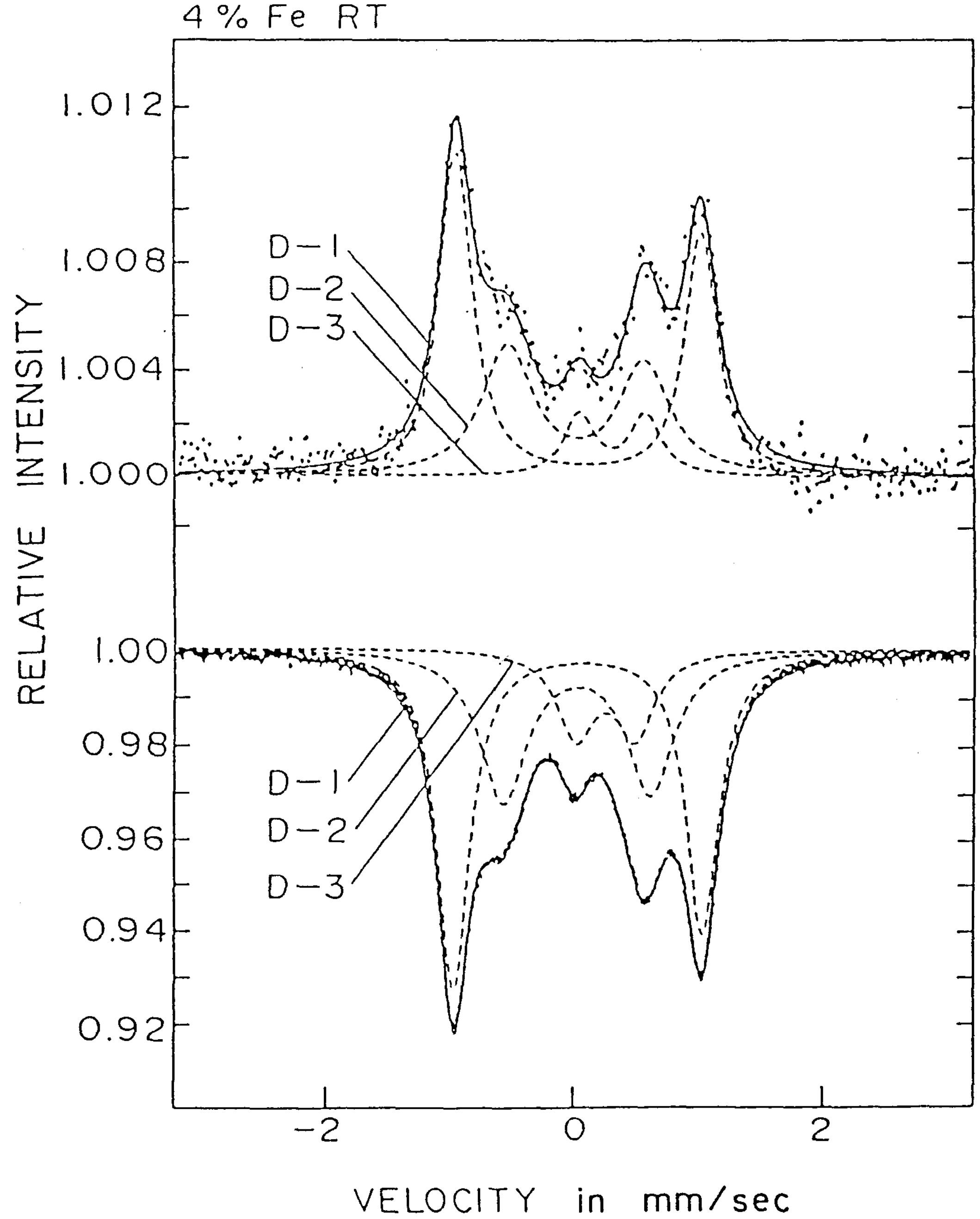

Fig. 3.5-2. ^{57}Fe CEMS spectrum (upper figure) and ^{57}Fe TMS spectrum (lower figure) obtained from x = 0.04 specimen at room temperature. Three different kinds of quadrupole-split doublets are shown by the broken lines and denoted by D-1, D-2 and D-3. Velocity scale is relative to α-Fe at room temperature.

Figure 3.5-3 and 3.5-4 show the CEMS and TMS spectra obtained from the specimens of x = 0.06 and x = 0.10, respectively. Isomer shift values and the magnitude of the quadrupole splitting determined from the CEMS spectra are again identical to the TMS spectra suggesting the identical chemical states of the Fe atoms at the surface to the bulk. However, the intensity ratio in D-1 component obtained from CEMS spectra differs from that of TMS spectra. The D-1 component has been interpreted as the spectrum component corresponding to the Fe atoms at Cu1 chain sites[8,21]. The intensity ratio in the quadrupole-split doublet of D-1 component, I_2/I_1, in which I_2 is the intensity at faster velocity side and I_1 is the intensity at the slower velocity side in the spectrum, is shown as solid circles in Fig. 3.5-5 as a function of the Fe concentration, x, together with the results from D-1 components in TMS spectra which are shown as open circles in the figure. The intensity ratio in the quadrupole-split doublet depends on the angle between the γ-ray propagation direction and the principal axis of the electric field gradient[27].

Figure 3.5-6 shows the results from X-ray diffraction pattern and clearly shows the preferred orientation of c-axis to the perpendicular direction to the surface for the disk shaped specimens, since the intensity of (005) is enhanced for the disk shaped specimens compared with that of the powder specimens. Since the X-ray diffraction pattern showed the preferred orientation of the c-axis of a perpendicular direction to the surface, the present CEMS measurements suggest that the principal axis of the electric field gradient is most probably parallel or perpendicular to the c-axis depending on the sign of the electric

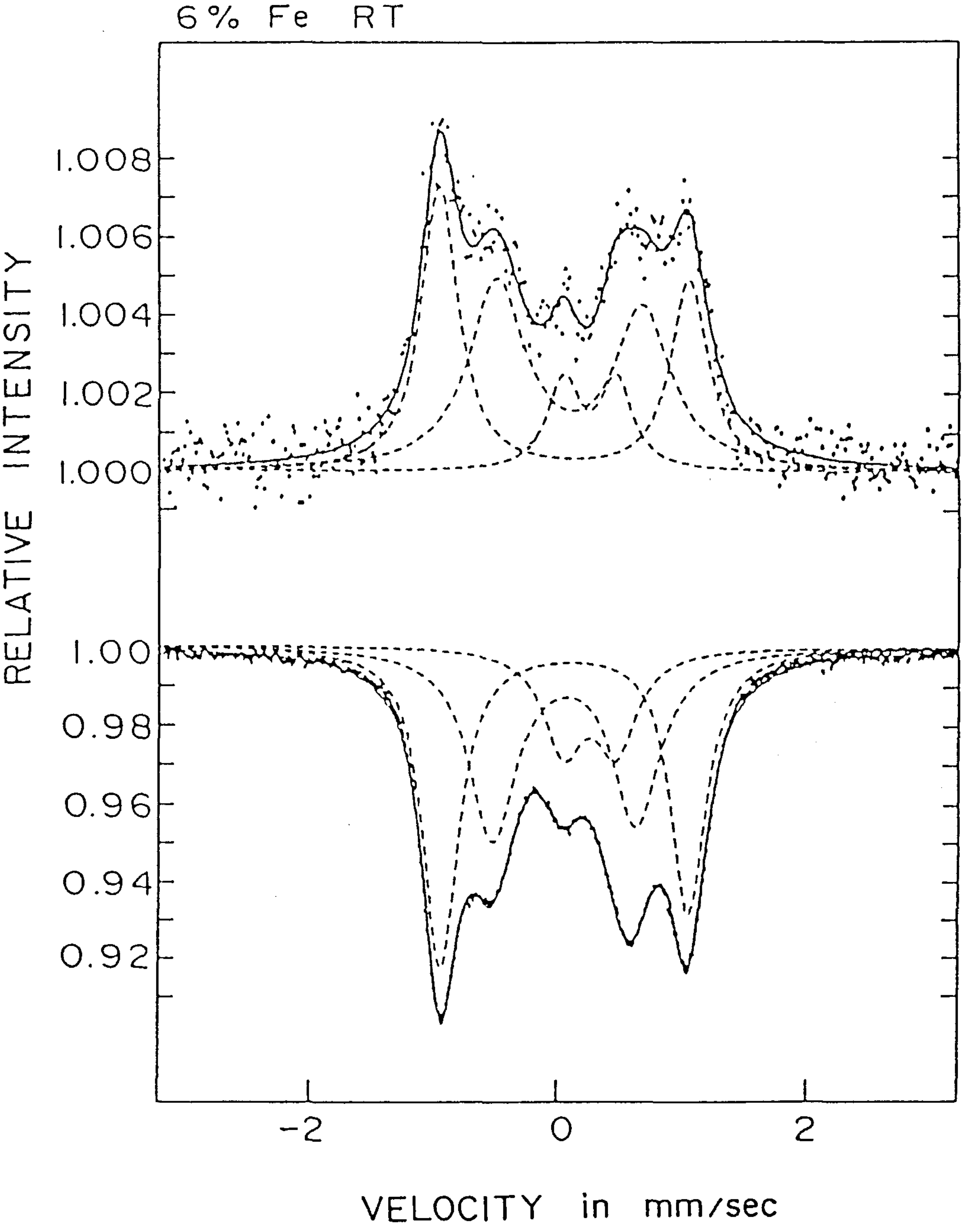

Fig. 3.5-3. ^{57}Fe CEMS spectrum (upper figure) and ^{57}Fe TMS spectrum (lower figure) obtained from x = 0.06 specimen at room temperature. Broken lines show the resolved partial components. Velocity scale is relative to α-Fe at room temperature.

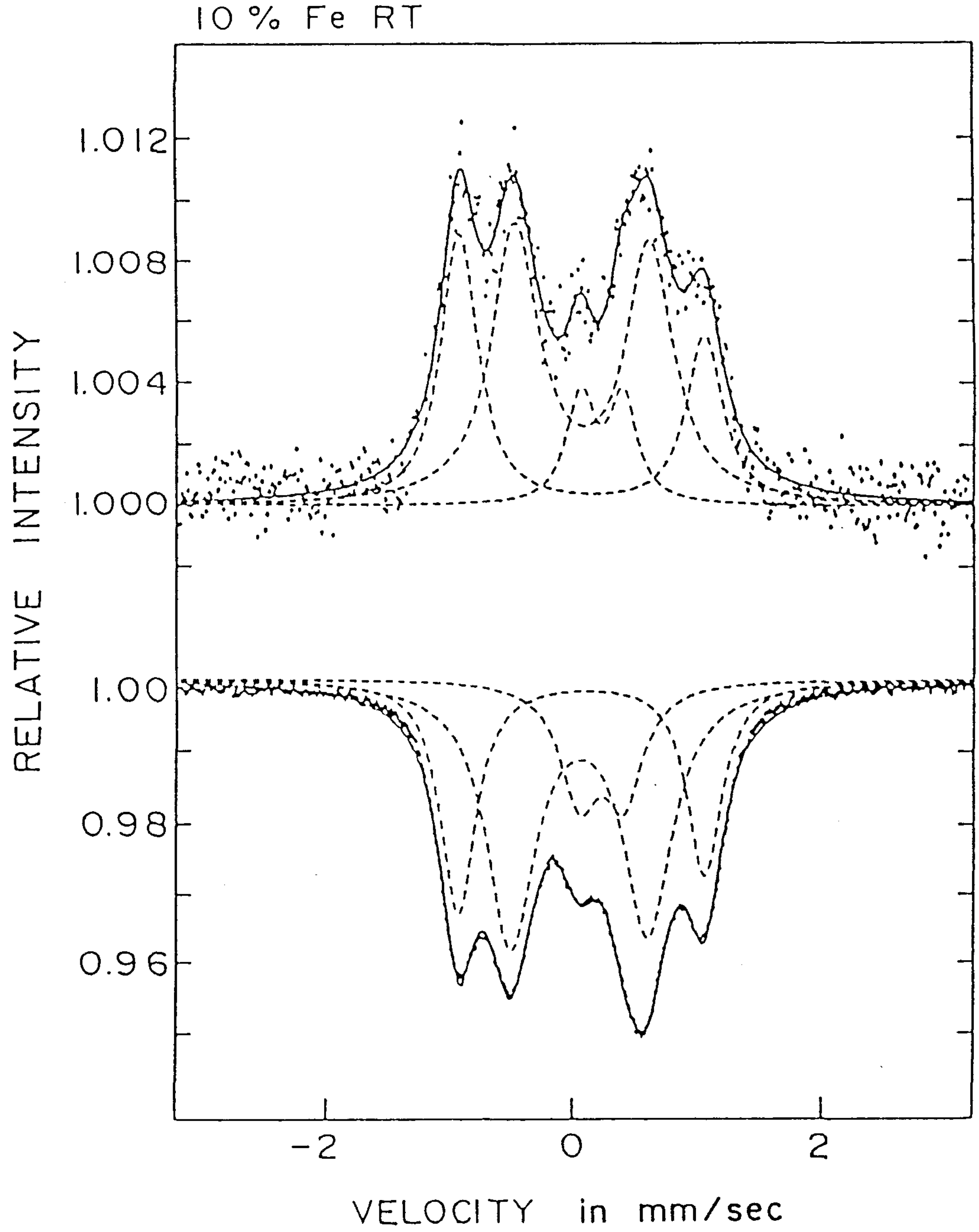

Fig. 3.5-4. ^{57}Fe CEMS spectrum (upper figure) and ^{57}Fe TMS spectrum (lower figure) obtained from x = 0.10 specimen at room temperature. Broken lines show the resolved partial components. Velocity scale is relative to α-Fe at room temperature.

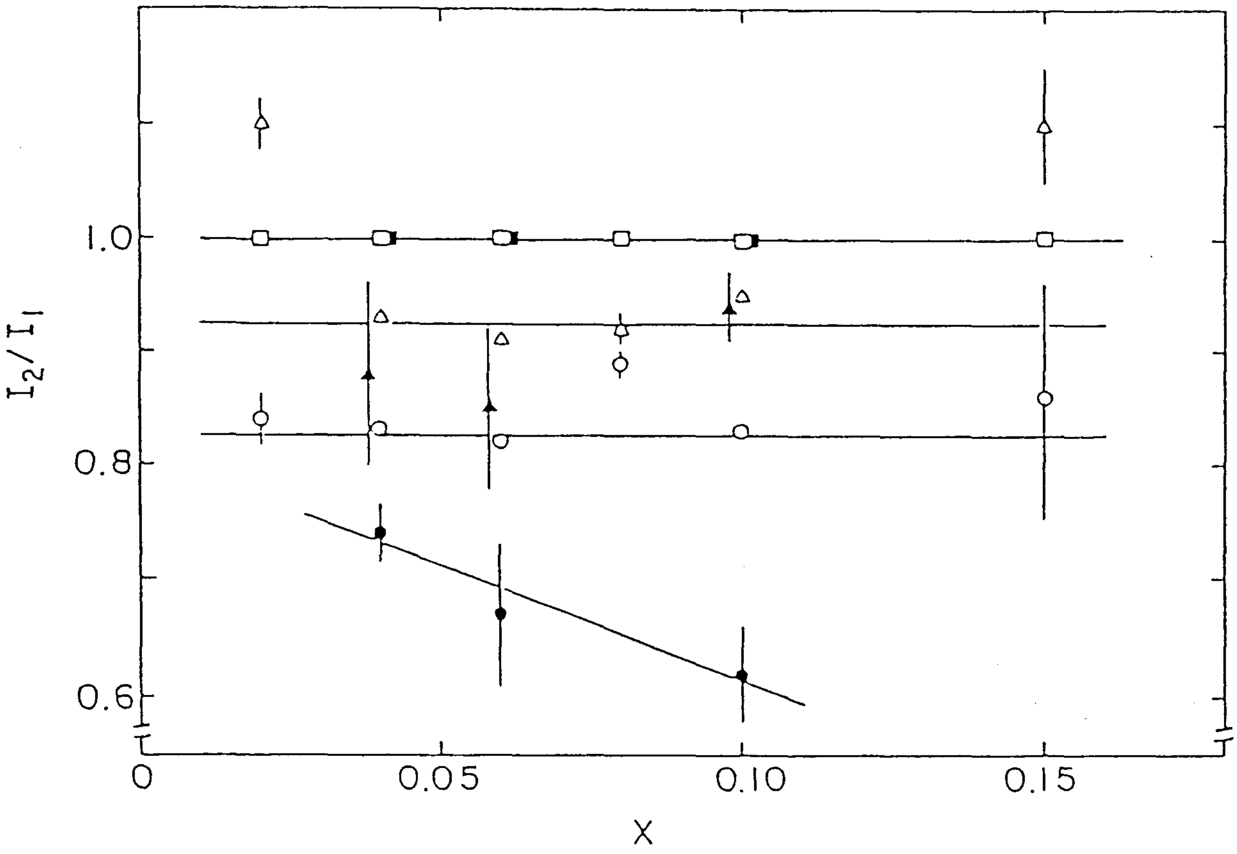

Fig. 3.5-5. Intensity ratio, I_2/I_1, where I_2 is the intensity at faster velocity side and I_1 is the intensity at slower velocity side in the spectrum.

○ : TMS for D-1
● : CEMS for D-1
△ : TMS for D-2
▲ : CEMS for D-2

Intensity ratio of D-3 component in CEMS and TMS spectra is assumed to be 1, namely $I_2/I_1 = 1$ as shown by □ and ■ , respectively.

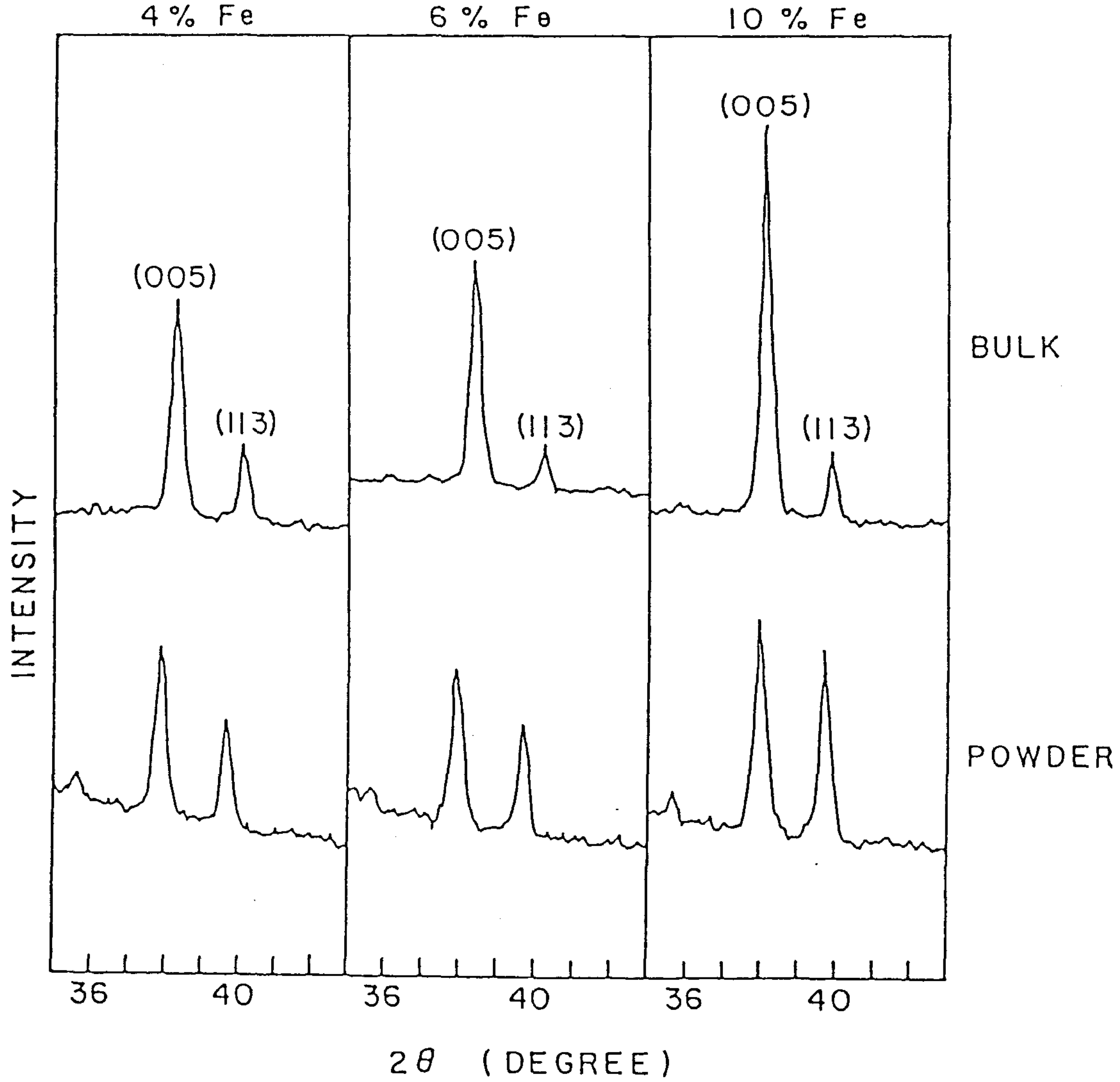

Fig. 3.5-6. X-ray diffraction pattern by Cu-K_α radiation obtained from Fe-doped 1-2-3 compounds. Upper patterns are for disk shaped specimens (bulk) and lower patterns are for powder specimens.

field gradient for D-1 component.

3.5.4 Conclusion

Conversion electron Mössbauer measurements have been performed using disk shaped Fe-doped 1-2-3 compounds and a newly developed electron detector in order to understand the difference in chemical states of Fe atoms at the surface and the bulk.

Mössbauer parameters determined from both of CEMS and TMS spectra for D-1, D-2 and D-3 components did not show any appreciable difference except for the intensity ratio in D-1 component. The intensity ratio of the D-1 component is affected by the existence of the preferred orientation of the c-axis to the surface of the disk shaped specimens and suggested that the principal axis of the electric field gradient is parallel or perpendicular to the c-axis for the D-1 component.

3.5.5 References

1. M.K.Wu, J.R.Ashburn, C.J.Torng, P.H.Hor, R.L.Meng, L.Gao, A.J.Haung, Y.Q.Wang and C.W.Chu, Phys. Rev. Lett., 58(1987)908.
2. S.Hikami, T.Hirai and S.Kagoshima, Jpn. J. Appl. Phys., 26(1987)L314.
3. R.J.Cava, B.Batlogg, R.B. van Dover, D.W.Murphy, S.Sunshine, T.Siegrist, T.P.Remeika, E.A.Rietman, S.Zahurak and G.P.Espinosa, Phys. Rev. Lett., 58(1987)1676.
4. S.Sato, I.Nakada, T.Kohara and Y.Oda, Jpn. J. Appl. Phys., 26(1987)L663.
5. Y.Oda, H.Fujita, H.Toyoda, T.Kaneko, T.Kohara, I.Nakada

and K.Asayama, Physica 148B(1987)339.

6. J.D.Jorgensen, M.A.Beno, D.G.Hinks, L.Soderholm, K.J.Volin, R.L.Hitterman, J.D.Grace, Ivan K.Schuller, C.U.Segre, K.Zhang and M.S.Kleefisch, Phys. Rev. B, 36(1987)3608.

7. J.M.Tranquada, D.E.Cox, W.Kunnmann, G.Shirane, H.Moudden, M.Suenaga, P.Zolliker, D.Vaknin, S.K.Sinha, M.S.Alvarez, A.J.Jacobson and D.C.Johnston, Phys. Rev. Lett., 60(1988)156.

8. V.Sedykh, S.Nasu and F.E.Fujita, Solid State Comm., 67(1988)1063.

9. E.Baggio-Saitovitch, I.Souza Azevedo, R.B.Scorzelli, H.Saitovitch, S.A.da Cunha, A.P.Guimaraes, P.R.Silva and A.Y.Takeuchi, Phys. Rev. B, 37(1988)7967.

10. J.M.Tarascon, P.Barboux, P.F.Miceli, L.H.Greene, G.W.Hull, M.Eibschutz and S.A.Sunshine, Phys. Rev. B, 37(1988)7458. ; M.Eibschutz, M.E.Lines, J.M.Tarascon and P.Barboux, Phys. Rev. B, 38(1988)2896.

11. Q.A.Pankhurst, A.H.Morrish, M.Raudsepp and X.Z.Zhou, J. Phys. C: Solid state Phys., 21(1988)L7.

12. E.R.Bauminger, M.Kowitt, I.Felner and I.Nowik, Solid State Comm., 65(1988)123.

13. T.Tamaki, T.Konai, A.Ito, Y.Maeno and T.Fujita, Solid State Comm., 65(1987)43.

14. M.Takano and Y.Takeda, Jpn. J. Appl. Phys., 26(1987)L1862.

15. C.W.Kimball, J.L.Matykiewicz, J.Giapintzakis, A.E.Dwight, M.B.Brodsky, M.Slaski, B.D.Dunlap and F.Y.Fradin, Physica B, 148(1987)309.

16. C.Blue, K.Elgaid, I.Zitkovsky, P.Boolchand, D.McDaniel,

W.C.H.Joiner, J.Oostens and W.Huff, Phys. Rev. B, 37(1988)5905.

17. L.Bottyan, B.Molnar, D.L.Nagy, I.S.Szucs, J.Toth, J.Dengler, G.Ritter and J.Schober, Phys. Rev. B, 38(1988)11378.

18. P.Boolchand, C.Blue, K.Elgaid, I.Zitkovsky, D.McDaniel, W.Huff, B.Goodman, G.Lemon, D.E.Farrell and B.S.Chandrasekhar, Phys. Rev. B, 38(1988)11313.

19. A.Simopoulos and D.Niarchos, Phys. Rev. B, 38(1988)8931.

20. R.A.Brand, Ch.Sauer, H.Lutgemeier, B.Rupp and W.Zinn, Physica C, 156(1988)539.

21. S.Nasu, H.Kitagawa, T.Kohara, Y.Oda, T.Shinjo, K.Asayama and F.E.Fujita, Trans. JIM, 29(1988)Supp.543.
; S.Nasu, H.Kitagawa, T.Kohara, Y.Oda, T.Shinjo, K.Asayama and F.E.Fujita, MRS Int'l. Mtg. on Adv. Mats., 6(1989)635.

22. S.Nasu, H.Kitagawa, Y.Oda, T.Kohara, T.Shinjo, K.Asayama and F.E.Fujita, Physica B, 148(1987)484.

23. Y.Maeno, T.Tomita, M.Kyogaku, S.Awaji, Y.Aoki, K.Hoshino, A.Minami and T.Fujita, Nature, 328(1987)512.

24. Y.Oda, H.Fujita, H.Toyoda, T.Kaneko, T.Kohara, I.Nakada and K.Asayama, Jpn. J. Appl. Phys., 26(1987)L1660.

25. Y.Maeno, M.Kato, Y.Aoki and T.Fujita, Jpn. J. Appl. Phys., 26(1987)L1982.

26. E.Sakagami, Y.Oda, Y.Yamada, T.Kohara and K.Asayama, J. Phys. Soc. Jpn., 56(1987)4255.

27. U.Gonser, "Mossbauer Spectroscopy", in Topics in Apllied Physics Vol. 5, Ed. by U.Gonser, Springer-Verlag, New York-Heidelberg-Berlin, (1975), p.26.

CHAPTER IV. SUMMARY

The newly designed electron counters have been developed and CEMS measurements have been applied to the several kinds of materials using these counters in order to demonstrate the benefits of CEMS to study the physical and chemical properties at the surface. The following results have been obtained from the experiments in this study.

1) Excellent signal to noise ratio of CEMS spectrum can be achieved by the development of the new electron counter designed for the CEMS measurement at room temperature. The CEMS measurement at 100 K is also possible by using the new counter designed for the low temperature CEMS measurement.

2) CEMS was applied to study the behavior of the ^{119}Sn implanted into Ni and Fe at room temperature.

In the case of the ^{119}Sn implantation into Ni, ^{119}Sn CEMS spectra of implanted ^{119}Sn atoms into Ni are interpreted by the two different kinds of contributions. One is the dissolved ^{119}Sn atoms into Ni which occupy the substitutional sites of Ni matrix. The other is the ^{119}Sn atoms in Ni_3Sn intermetallic compounds, which would be formed by the radiation enhanced diffusion of ^{119}Sn atoms. These two states of implanted ^{119}Sn atoms depend on the local Sn concentration. The acceleration energy and dose dependence of ^{119}Sn CEMS spectra is also well explained by the change of the local Sn concentration.

In the case of the ^{119}Sn implanted into Fe, the formation of the intermetallic compound of Fe and Sn was not observed. The implanted ^{119}Sn atoms are dissolved into Fe and occupy the substitutional site of α-Fe matrix at the region of the low local Sn concentration. At the region of the local Sn concentration over the maximum solid solubility of Sn in Fe, the oxides and cluster of Sn atoms are formed without containing Fe atoms. This phenomenon is quite different from the ^{119}Sn atoms implanted into Ni, which formed Ni_3Sn intermetallic compounds at the region of the high Sn concentration. The behavior of implanted Sn atoms may be influenced by the defect structure introduced by the implantation and the mobility of vacancies in Fe and Ni metals at room temperature.

3) CEMS was applied to the study of the work hardening around the surface of Hadfield steel. From CEMS measurements, α' martensite, carbides and segregations of carbon atoms were not detected in the CEMS spectra obtained from the specimens after working. The decarburization around surface was found by the CEMS measurements and the formation of ε martensite was observed in the transmission Mössbauer spectrum of the cold-rolled specimen measured at 20 K. From these results, it is concluded that the remarkable work hardening of Hadfield steel results from the formation of the thin ε martensites.

4) The interface between the Al_2O_3 deposited by the chemical vapor deposition technique and α-Fe substrate was investigated by ^{57}Fe CEMS. At the interface between Al_2O_3 layer and α-Fe substrate, Fe atoms do not mix to each other after deposition.

After annealing the deposited specimens, the two kinds of the ionic states of Fe^{2+} and Fe^{3+} were observed in CEMS spectra. However Fe^{2+} state was only observed after annealing at 1273 K. At 1273 K, α-Fe as the substrate transforms to γ-Fe so that this transformation would affect the formation of Fe^{2+} ionic state.

5) The surface layers of $Nd_2Fe_{14}B$ compounds were studied by ^{57}Fe CEMS. The CEMS spectra of as polished specimens are similar to the transmission Mössbauer spectrum of the powder specimen as the bulk. It suggests that the chemical state at the surface of the $Nd_2Fe_{14}B$ compound is not different from that in the inner bulk even after polishing the surface. The alignment of c-axis around the surface is also same to the original alignment at the press-forming process in spite of the polishing of the surface. After the heat-treatment of the specimens, only α-Fe component was observed in any CEMS spectra. The small coercive force around the surface of the Nd-Fe-B permanent magnet after the heat treatment is responsible to the decomposition of Nd and B atoms from the surface and the formation of α-Fe layers during the heat-treatment. CEMS measurements clearly showed that the surface of the heat-treated Nd-Fe-B permanent magnet is covered with α-Fe layers.

6) The ^{57}Fe CEMS measurements were performed for the disk shaped pellets of Y-Ba-Cu oxide superconductors doped by ^{57}Fe. Comparing the ^{57}Fe CEMS spectra with transmission Mössbauer spectra, it is suggested that the chemical state of Fe atoms around the surface are identical to that of the bulk. The

intensity ratio of the component corresponding to Fe atoms at the Cu1 chain sites indicates that the principal axis of the electric field gradient is most probably parallel or perpendicular to the c-axis, depending on the sign of the electric field gradient.

Above results demonstrate clearly that the CEMS is a quite powerful technique to study the physical and chemical properties at the surface of materials.

ACKNOWLEDGEMENTS

The author wishes to express hearty gratitude to Prof. F. E. Fujita and Prof. S. Kume for their continuous guidance and encouragement throughout this work and criticizing of the manuscripts of this thesis. He wishes especially to express hearty thanks to Dr. S. Nasu for his continuous collaboration, various suggestions and help throughout this work. He also give his thanks to Prof. R. Oshima and Dr. T. Ezawa in the same laboratory for their valuable discussions and helpful advice for the experiments. He is much indebted for a lot of persons to prepare the specimens of CEMS measurements and to perform the Mössbauer measurements. All ^{119}Sn ion-implantations were carried out at Electrotechnical Laboratory, Tsukuba, with the kind cooperation by Drs. I. Sakamoto, N. Hayashi and H. Tanoue. It is very kind of Drs. K. Nakaoka and Y. Shima, Technical Research Center, NKK, Kawasaki, to prepare the specimens of Hadfield steels. The deposition of Al_2O_3 on α-Fe was performed at Mitsubishi Electric Corporation, Amagasaki, with hearty cooperation by Mr. S. Hoshinouchi. The samples of Nd-Fe-B alloys were kindly prepared by Dr. S. Hirosawa, Sumitomo Special Metals, Mishimagun, Osaka. The specimens of ^{57}Fe doped Y-Ba-Cu oxide superconductor were kindly offered by Prof. T. Kohara, Himeji Institute of Technology. The Mössbauer measurements were carried out by the hearty cooperation of Messrs. H. Takano, H. Kitagawa and A. Fujisawa. He is sincerely thankful to these persons for their kindness. He also appreciates great helps of Messrs. M. Yoshida, T. Abe, H. Nakagawa, S. Imaoka, T. Kawano and other members in the same laboratory for the preparations of the manuscript.